



universität
wien

DISSERTATION / DOCTORAL THESIS

Titel der Dissertation /Title of the Doctoral Thesis

„Hub architecture and high-order connectivity features support global brain dynamics in the *C. elegans* neuronal network“

verfasst von / submitted by

Kerem Uzel

angestrebter akademischer Grad / in partial fulfilment of the requirements for the degree of

Doctor of Philosophy (PhD)

Wien, 2021 / Vienna 2021

Studienkennzahl lt. Studienblatt /
degree programme code as it appears on the student
record sheet:

UA 794 685 490

Dissertationsgebiet lt. Studienblatt /
field of study as it appears on the student record sheet:

Molekulare Biologie

Betreut von / Supervisor:

Univ.-Prof. Dr. Manuel Zimmer

TABLE OF CONTENTS

1. ACKNOWLEDGEMENTS	4
2. SUMMARY	5
2.1. Abstract	5
2.2. Zusammenfassung	6
3. INTRODUCTION	8
3.1. Anatomy and function of the <i>C. elegans</i> nervous system	8
3.2. Neuronal population dynamics.....	11
3.2.1. Neuronal population dynamics in <i>C. elegans</i>	12
3.3. Mapping the nervous system	13
3.3.1. Connectome reconstruction	13
3.3.2. The <i>C. elegans</i> connectome	14
3.3.3. Other efforts of connectomes.....	16
3.3.4. Comparative connectomics.....	16
3.4. Network measures in general and in the <i>C. elegans</i> connectome.....	17
3.4.1. Measures of functional segregation	18
3.4.2. Measures of functional integration	20
3.4.3. Measures of centrality.....	20
3.4.4. Measures of resilience	21
3.4.5. Small-world property.....	22
3.4.6. Connectivity motifs.....	23
3.4.7. Symmetry in the networks	25
3.5. Rich club neurons in brain networks and in the <i>C. elegans</i> connectome	25
3.6. Functional activity measures	27
3.6.1. Linear measures	27
3.6.2. Non-linear measures	28
3.7. Systematic interrogation of neurons	29
3.7.1. AIB neurons	29
3.7.2. AVA neurons	30
3.7.3. AVB neurons	30
3.7.4. AVE neurons.....	31
3.7.5. RIB neurons	31
3.7.6. RIM neurons	32
3.7.7. PVC neurons	32
4. RESULTS	33
4.1. Coordinated population dynamics in nervous system wide imaging experiments.....	33
4.2. Local connectivity patterns predict functional interactions	38
4.3. Neuronal identity and input similarities predict neuronal interactions.....	42

4.4.	Systematic search for structure-function relationships	46
4.5.	<i>In silico</i> perturbations suggest determinant network hubs	49
4.6.	Disrupting network hubs decreases global correlations	53
4.7.	Disrupting connectivity features decreases pairwise neuronal correlations.....	64
5.	DISCUSSION	68
5.1.	Probing the network will increase the number of observed brain states	68
5.2.	Signed and multi-layered connectome might reveal new structure-function relationships	70
5.3.	Improvement of structure-function predictions via input similarities and symmetries	72
5.4.	Relationship between genetic identity and connectivity	74
5.5.	Temporal dynamics of neuronal inhibition methods	75
5.6.	Role of neurotransmitter pathways in neuronal population dynamics	76
5.7.	Contribution of the dominant PC modes to structure-function relationships.....	77
5.8.	The role of rich club organization within the network	79
5.9.	Neuronal population dynamics as an emergent property.....	80
6.	MATERIALS AND METHODS	83
6.1.	Worm culture and strains.....	83
6.2.	Whole-Brain calcium imaging of <i>C. elegans</i> head and tail ganglia neurons	84
6.3.	Neural time series extraction	85
6.4.	Identification of head and tail ganglia neurons	86
6.5.	Leave-one-out procedure to test the robustness of correlation values	86
6.6.	Derivatives on neural time series data.....	87
6.7.	Effective dimensionality	87
6.8.	Shared dimensionality	87
6.9.	Calculating the residual activity of neurons.....	88
6.10.	Brain state transition quantification.....	88
6.11.	Identification of backward and forward clusters	88
6.12.	Population behavioural assays	88
6.13.	Posterior harsh touch assays	89
6.14.	Activity measures.....	89

6.14.1.	Correlation coefficient	89
6.14.2.	Cross correlation coefficient	89
6.14.3.	Mutual information	89
6.14.4.	Covariogram analysis.....	90
6.15.	Randomized networks	90
6.15.1.	Totally randomized networks	90
6.15.2.	Degree-preserved randomized networks.....	90
6.15.3.	Degree-, reciprocal connections and gap junction-chemical synapse likelihood preserved randomized networks	91
6.15.4.	Rich-club curve preserved randomized networks.....	91
6.15.5.	Partial randomization analysis	92
6.16.	Connectivity measures	92
6.16.1.	Input similarities	92
6.16.2.	Sum of inverse shortest path calculation.....	93
6.17.	<i>In silico</i> perturbation screen.....	93
6.17.1.	Generating perturbed networks.....	93
6.17.2.	Graph theoretical measures on perturbed networks.....	93
6.17.3.	Principal component analysis (PCA) on measures of perturbed networks.....	94
6.18.	Rich club analysis	94
6.19.	Connectivity motifs.....	95
6.19.1.	Dyad connectivity motifs	95
6.19.2.	Triplet connectivity motifs.....	95
6.20.	Classification of perturbed and control neuronal pairs.....	98
6.21.	Permutation test for global correlation and activity change in WT vs. HisCl datasets	98
6.22.	Custom shuffle test for comparing correlation values	99
7.	REFERENCES	100

1. Acknowledgements

I take this opportunity to gratefully acknowledge the assistance and contributions of the people who had faith in this work.

Foremost, to my supervisor Manuel Zimmer for all his guidance and support during my PhD.

To Prof. Mario de Bono and Prof. Thomas Hummel for evaluating my thesis.

To Richard Latham, Harris Kaplan, Tina Schrödel, Annika Nichols and Susanne Skora for everything they taught me in the lab.

To Luka Železnik, Oriana Salazar Thula, Ulises Rey Torné, Niklas Khoss, Mara Andrione, Julia Riedl, Charles Fieseler, Itamar Lev, Lukas Hille and all past and current members of the Zimmer lab for their help and companionship throughout this journey.

To Enrico Lanza for his unique contribution to my PhD during our collaboration.

To Duygu Demiröz, Levent Baş, Kaya Akyüz, İpek Ergal, Deniz Abdüsselamoğlu, Emine Dindar and Arda Kara for adding a touch of Turkishness to my expat life.

To IMPerfectos for never stop paddling.

To Arkasaha for the councils and revelry.

To Stannis Baratheon, the one true king, for leading us forward, only forward.

To Vienna the third, LG3317, Schweizer Garten and Arsenal, for being my home for many years.

To Alte Donau for beautiful Viennese summer days.

To my bicycles and sea kayak, Muddyfox, Ferit, Ferdi and Oru, for their services.

To Cunda & 25 islands for being a beacon of light in the midst of winter.

To Atman and the Gulf of Edremit for the most beautiful present in the world.

To my parents, Erkan and Çiğdem Uzel, for their unconditional love and support.

To my hero F. Gözde Çilingir for daring to get on that red canoe with me.

And last but not least, to all Kerems of the past seven years for their struggle and persistence. May your efforts light my way.

2. Summary

2.1. Abstract

Large scale activity recordings in various organisms, ranging from leeches to monkeys, revealed low dimensional neuronal population dynamics, i.e. individual neurons strongly coordinate their activity among each other to generate network wide correlated population states. Neuronal population dynamics are crucial for neuronal computations and the generation of behavior, however, the mechanisms generating such dynamics remain unknown. I propose that the anatomical connectome must provide the crucial architecture supporting coordinated network dynamics. But how does the anatomical wiring relate to the functional interactions between the neurons?

Using *C. elegans*, I addressed this question with a unique experimental paradigm combining three powerful tools: whole-brain imaging of identifiable neurons, genetic neuronal inhibition tools and knowledge of the connectome of the entire nervous system with synaptic resolution. First, I systematically analyzed local interactions and general features of the network to test whether they can predict neuronal correlations. Next, I performed systematic network perturbations by interrogation of neurons via transgenic neuronal inhibition tools. Finally, various computational methods were used to assess the impact of these perturbations on neuronal population dynamics and relate the outcome to the *C. elegans* connectome.

Systematically comparing graph features in the *C. elegans* connectome with correlations in nervous system wide neuronal dynamics, I found that local connectivity motifs and input similarities can predict functional relationships between neurons. Informed by graph theory, I inhibited selected sets of rich-club neurons (i.e. network hubs) leading to destruction of critical features in network architecture. Using whole-brain imaging in these animals I found that global correlation structure is largely reduced but individual neurons and smaller modules remain active, however in an uncoordinated way. Thus, when disconnecting network hubs, structure in neuronal population activity is specifically destroyed. Based on my data, I propose that both rich-club architecture in neuronal wiring and the dynamical properties of neurons are required for normal neuronal population dynamics. In my model, strong synaptic coupling between neurons across the connectome via network hubs and higher order connectivity features binds intrinsically active neurons to global population states providing a mechanistic model relevant for larger neural systems where neuronal population dynamics can be observed.

2.2. Zusammenfassung

Groß angelegte Aktivitätsaufzeichnungen in verschiedenen Organismen, vom Blutegel bis zum Affen, zeigten eine niedrigdimensionale neuronale Populationsdynamik, d. h. einzelne Neuronen koordinieren ihre Aktivität stark untereinander, um netzwerkweit korrelierte Populationszustände zu erzeugen. Die neuronale Populationsdynamik ist entscheidend für neuronale Berechnungen und die Entstehung von Verhalten, aber die Mechanismen, die diese Dynamik erzeugen, sind noch unbekannt. Wir gehen davon aus, dass das anatomische Konnektom die entscheidende Architektur für die koordinierte Netzwerkdynamik darstellt. Aber wie hängt die anatomische Verdrahtung mit den funktionellen Interaktionen zwischen den Neuronen zusammen?

Mit Hilfe von *C. elegans* bin ich dieser Frage mit einem einzigartigen experimentellen Paradigma nachgegangen, das drei leistungsstarke Werkzeuge kombiniert: Ganzhirn-Bildgebung identifizierbarer Neuronen, genetische neuronale Hemmungswerkzeuge und Kenntnis des Konnektoms des gesamten Nervensystems mit synaptischer Auflösung. Zunächst analysierte ich systematisch lokale Interaktionen und allgemeine Merkmale des Netzwerks, um zu prüfen, ob sie neuronale Korrelationen vorhersagen können. Als Nächstes führte ich systematische Netzwerkstörungen durch, indem ich Neuronen mit Hilfe von transgenen neuronalen Hemmungsinstrumenten befragte. Schließlich wurden verschiedene Berechnungsmethoden eingesetzt, um die Auswirkungen dieser Störungen auf die neuronale Populationsdynamik zu bewerten und die Ergebnisse mit dem Konnektom von *C. elegans* zu vergleichen.

Durch den systematischen Vergleich von Graphenmerkmalen im Konnektom von *C. elegans* mit Korrelationen in der neuronalen Dynamik des gesamten Nervensystems fand ich heraus, dass lokale Konnektivitätsmotive und Ähnlichkeiten im Input funktionelle Beziehungen zwischen Neuronen vorhersagen können. Auf der Grundlage der Graphentheorie hemmte ich ausgewählte Gruppen von Neuronen mit vielen Verbindungen (d. h. Netzwerkknotenpunkte), was zur Zerstörung kritischer Merkmale der Netzwerkarchitektur führte. Mit Hilfe der Ganzhirnbildgebung bei diesen Tieren konnte ich feststellen, dass die globale Korrelationsstruktur weitgehend reduziert ist, einzelne Neuronen und kleinere Module jedoch aktiv bleiben, wenn auch in unkoordinierter Weise. Wenn also die Knotenpunkte des Netzwerks abgeschaltet

werden, wird die Struktur der neuronalen Populationsaktivität gezielt zerstört. Auf der Grundlage unserer Daten schlage ich vor, dass sowohl die Rich-Club-Architektur in der neuronalen Verdrahtung als auch die dynamischen Eigenschaften der Neuronen für eine normale neuronale Populationsdynamik erforderlich sind. In meinem Modell bindet eine starke synaptische Kopplung zwischen Neuronen im gesamten Konnektom über Netzwerkknotenpunkte und Konnektivitätsmerkmale höherer Ordnung intrinsisch aktive Neuronen an globale Populationszustände und liefert damit ein mechanistisches Modell, das für größere neuronale Systeme relevant ist, in denen neuronale Populationsdynamik beobachtet werden kann.

3. Introduction

3.1. Anatomy and function of the *C. elegans* nervous system

The nervous system of *C. elegans* hermaphrodite consists of 302 neurons with 118 different neuronal classes (White et al., 1986). The nervous system is divided into two parts as the pharyngeal and somatic nervous system and almost totally separated from each other (White et al., 1986). The pharyngeal nervous system is responsible for the rhythmic contractions of the pharynx that allows the animal to eat. The somatic nervous system consists sensory, inter- and motorneurons, in total 279 neurons, which generates and maintains the brain dynamics and behaviour of the animal. Thus, all the analyses throughout this thesis solely focuses on the somatic nervous system and considering it as the whole nervous system of the animal in anatomical analysis of the wiring map (see Chapter 3.3.2). To this day, the anatomical map of the entire nervous system with synaptic resolution is only available for *C. elegans* which provides a powerful tool for neuroscience studies.

The *C. elegans* somatic nervous system is further organized in various ganglia. Head ganglion consists of majority of interneurons which are densely packed and anatomically grouped into anterior, dorsal, ventral, lateral and retrovesicular ganglion. Retrovesicular ganglion is followed by the ventral nerve cord where majority of motor neurons reside throughout the anterior-posterior axis of the animal. These motor neurons innervate the body wall muscles on both ventral and dorsal side of the animal to implement undulatory movement along the body. The ventral nerve cord transitions into tail ganglion at the very posterior end of the nervous system. Tail ganglion is also divided into three anatomical groups: pre-anal, dorso-rectal and lumbar ganglion. Neural processes originating from neurons both in head and tail ganglia form nerve bundles along the entire body of the animal which connects both regions (**Fig.3.1**) (White et al., 1986).

The body plan of *C. elegans* is bilaterally symmetric and two thirds of the neurons are present as bilaterally symmetric left and right (L-R) pairs of the same neuron class (Hobert et al., 2002). This symmetry includes similarity in morphology, function and connectivity of neurons. There are few exceptions of functional asymmetries between the L-R pairs, and they are restricted to sensory neurons (e.g. salt-sensing ASE neurons (Cochella and Hobert, 2012)).

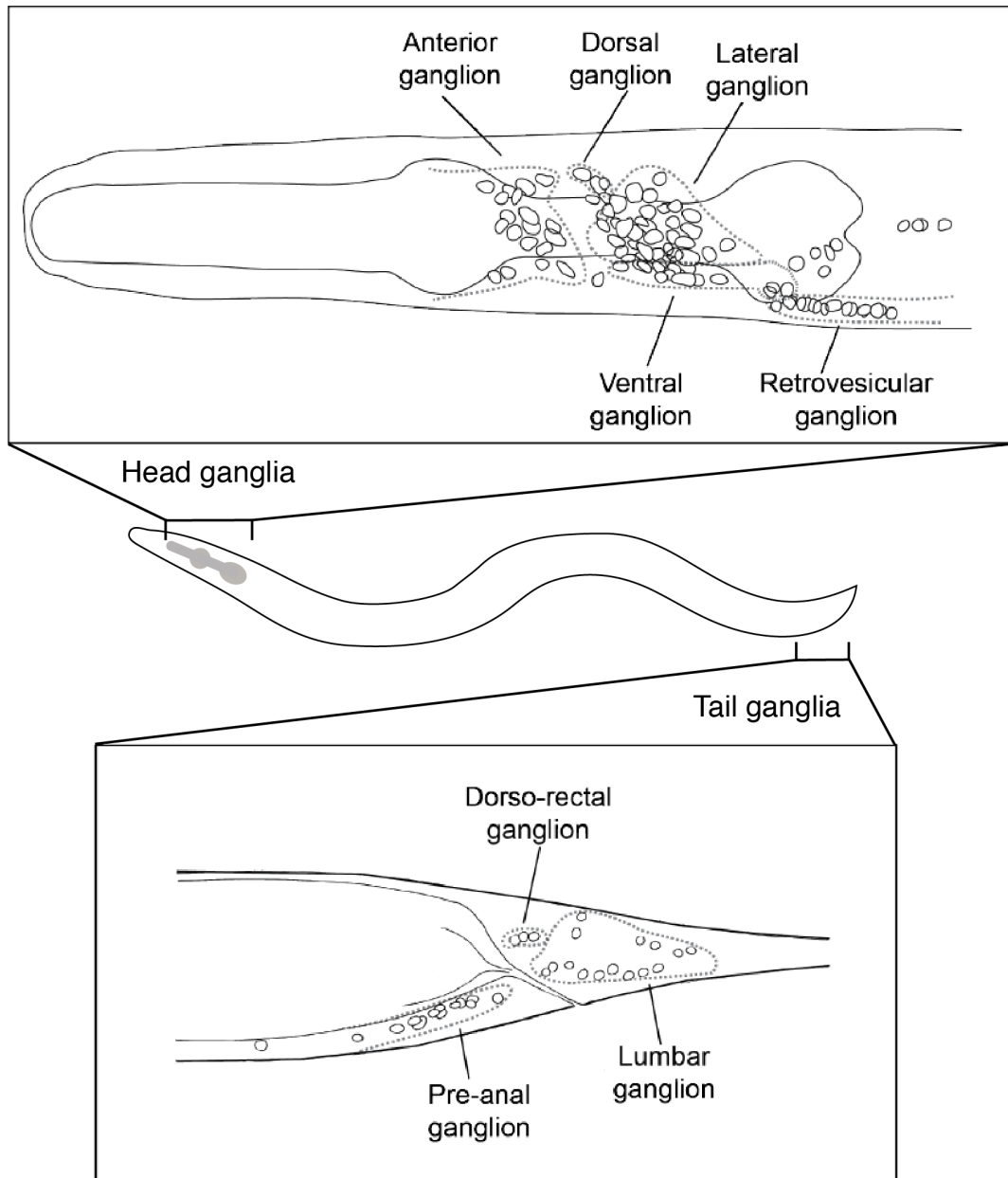


Figure 3.1. Head and tail ganglia of the *C. elegans* nervous system.

Schematic illustration of the nervous system in *C. elegans*. Ganglia illustrations are adapted and modified from White *et al.*, 1986.

All classic neurotransmitters are conserved and used in the nervous system of *C. elegans* such as glutamate, acetylcholine and γ -aminobutyric acid (GABA). Monoaminergic transmitters such as dopamine, serotonin, octopamine (invertebrate counterpart of epinephrine) and tyramine (invertebrate counterpart of norepinephrine) are also used (Chase and Koelle, 2007). A neurotransmitter atlas containing almost all neurons is previously mapped (Bentley *et al.*, 2016; Gendrel *et al.*, 2016; Pereira *et al.*, 2015; Serrano-Saiz *et al.*, 2013). *C. elegans* neurons also use around 250 neuropeptides (Li and Kim, 2008); these molecules can be co-released with neurotransmitters (Burnstock,

2004; Chalasani et al., 2010) or can initiate modifications in other cells extrasynaptically. Thus, neurons in the nervous system have another layer of communication on top of the already available synapses and connections (see Chapter 3.3.2).

Many neurons in the nervous system of *C. elegans* also form gap junctions (electrical synapses). They are formed by innexin proteins instead of connexin proteins in vertebrates. The innexin proteins do not contain specific sequence homologies with connexins but they function to form intercellular membrane channels similar in both structure and function compared to their counterparts in vertebrate tissues (Hall, 2017). Furthermore, number and organization of the innexin genes in *C. elegans* is similar to the connexin family in vertebrates. The *C. elegans* genome contains 25 innexin genes and at least one member of this family is expressed in almost every cell type in the animal; moreover, many cells express multiple different innexin genes (Altun et al., 2009). This complex expression pattern of innexins gives rise to formation of heterotypic and heteromeric gap junctions (Liu et al., 2013; Starich et al., 2014). In the nervous system of *C. elegans* the innexin expression pattern is very diverse: 20 out of 25 innexin genes were shown to be expressed in at least one neuron (Altun et al., 2009). There are few innexins that are expressed in a very confined set of neurons: INX-14 only in GABAergic motor neuron classes, INX-2 only in AVK, INX-1 only in AIB (Altun et al., 2009). On the other hand, many innexin genes are expressed in 15-30 neuron classes (Altun et al., 2009; Bhattacharya et al., 2019); moreover, few neuron classes express up to 12 innexin genes (Altun et al., 2009). Since many neurons are connected to each other with the aforementioned diversity of innexin gene expression as their repertoire, the heteromeric and heterotypic channels exist in the nervous system. Results of the mutant screens in innexin genes showed that single mutations of different innexin genes ended up with mild or almost no obvious phenotypes (Starich et al., 1996) suggesting that there are redundancies in the function of these genes. Although the exact amount of gap junctions is identified and quantified in the connectome of *C. elegans*, the exact mixture and identity of innexins within these junctions are not fully delineated.

Voltage-gated sodium channels are not present in the *C. elegans* genome (Bargmann, 1998); thus, it was thought for long that the *C. elegans* nervous system is made up of only graded neurons and lack classical action potentials. Recently, regenerative all-or-

none action potentials were discovered in AWA sensory neurons (Liu et al., 2018) which suggests that the *C. elegans* nervous system uses a hybrid system for encoding information. Additionally, two more enteric motor neurons that are implicated in defecation motor program were proposed to exhibit action potentials (Jiang et al., 2021) suggesting that AWA neurons are not the sole exceptions. However, the synaptic transmission mainly depends on voltage-dependent calcium and potassium currents, thus; the neurons exhibit graded potentials (Bargmann, 1998; Goodman et al., 1998; Lindsay et al., 2011; Narayan et al., 2011). Graded signaling is not as efficient as action potentials over long distances; but they allow parallel computations to occur in different compartments of a neuron. Additionally, bistable plateau potentials in some neurons exist (Mellem et al., 2008) which also depends on sodium and calcium currents. In these events, the release of synaptic vesicles occurs in a calcium-dependent manner. Thus, intracellular calcium concentrations increase with membrane depolarization. This provides an opportunity for using genetically encoded calcium indicators (GECI) as proxy for neuronal activity and make *C. elegans* a suitable model organism to track activity of neurons. The most common GECI variant, which is also used in this study, is GCaMP. It is a variant of circularly permuted variant of enhanced green fluorescent protein (cpEGFP). This indicator also contains a calcium-binding calmodulin and M13 sequence fragment of myosin light chain kinase (Akerboom et al., 2012; Chen et al., 2013; Nakai et al., 2001; Tian et al., 2009). Calcium binding results in conformational changes in the indicator that increases the brightness of the fluorophore which can be detected and measured (Nakai et al., 2001). Throughout this thesis, GCaMP is expressed in the worms using a pan-neuronal promoter with a nuclear localization tag to visualize the entire nervous system with single-cell resolution and recorded with high temporal resolution to reveal nervous system wide activity patterns (see Methods).

3.2. Neuronal population dynamics

Neural activity in groups of neurons was studied in various organisms including primates, zebra finches, leeches, and mice across different brain regions such as the olfactory bulb, the nerve cord ganglia or the motor cortex (Briggman et al., 2005; Churchland et al., 2012; Stopfer et al., 2003). Recently large-scale recordings of brain networks are also available with the advances in technology in large nervous systems (Ahrens et al., 2012; Bruno et al., 2017; Shine et al., 2019). These large-scale recordings

also revealed that the population activity is highly complex. All of these studies commonly reported that individual neurons do not display isolated activities, rather, they are involved in a network activity which is coordinated and patterned. Common features of these network states are (1) low dimensionality, i.e. information can be compressed to far less variables than the number of participating neurons; and (2) transient dynamics, i.e. network states continuously evolve in time (Briggman et al., 2005; Churchland et al., 2012; Stopfer et al., 2003). Low dimensional signals of population activity are shown to be available in neural circuits for sensory encoding (Bartho et al., 2009), decision-making (Briggman et al., 2005; Mante et al., 2013) or movement (Ahrens et al., 2012; Nguyen et al., 2016; Venkatachalam et al., 2016). Importantly, these studies found out that population activity might be complex and heterogenous in essence; but originally derived from a low dimensional system.

3.2.1. Neuronal population dynamics in *C. elegans*

In 2015, Kato *et al.* have delineated the general properties of the global population dynamics using whole-brain imaging in immobilized *C. elegans* (Kato et al., 2015). Since an important part of this thesis is based on the whole-brain imaging method in *C. elegans* (with the modification of extending it to contain both head and tail ganglia of the worm) and the activity patterns analyzed in this thesis are thoroughly characterized in this earlier work, I will briefly summarize these important findings in this section.

The behavioural repertoire of *C. elegans* consists forward and backward movement and ventral or dorsal turning behaviour; all of these individual events form an action sequence and thereby the coherent behaviour of the animal. However, the frequency of these events or the relative time spent in these events can be altered according to the external and internal factors. Kato *et al.* showed that majority of the neurons within the head ganglia of immobilized and unstimulated worms are active and they participate in coordinated global activity patterns. Furthermore, many of the participating neurons that show strong activity signals were shown to be correlated with the execution of motor commands in freely moving worms. These motor command related activity patterns of aforementioned neurons were also observed in immobilized worms where the worms are restricted by a chip and a chemical drug. Thus, in the absence of any movement, these neuronal activity patterns constituted a high-level representation of motor commands that is decoupled

from the motor output. Interestingly, it was also shown that these motor states are not only represented by a single neuron but rather a group of neurons, thus, the observed activity patterns are considered as distributed across the nervous system. Principal component analysis (PCA) was used to analyze and characterize the global brain dynamics. The first three PCs on average explained ~60% of the total variance and they received highest contributions from neurons that exhibit activity corresponding to the motor command sequence. PC1 captured the activity of neurons that are active either in forward and backward movement (with positive or negative signs, respectively). PC2 and PC3 have contributions from head motor neurons that are active during the turning events. Plotting the dominant PCs versus each other revealed a cyclical trajectory of the brain dynamics where the time-evolution of the global brain states are clearly visible. In this cyclical manifold, each distinct motor state was confined to a branch of this manifold; thus, the brain-state of the animal which follows the motor command sequence could be traced throughout the span of the whole-brain recordings.

Importantly, the neuronal activity correlations analyzed in this thesis can be robustly observed across different conditions like in well-fed adults without food (Kaplan et al., 2020; Kato et al., 2015), during larval development and in the presence of food (Nichols et al., 2017) and after short-term and long-term starvation (Skora et al., 2018). This suggests that the action sequence which is represented by the observed brain dynamics is robust to many conditions.

3.3. Mapping the nervous system

3.3.1. Connectome reconstruction

In order to map the entire nervous system including all connections from and to a neuron and its neighbouring neurons, dense mapping methods are needed. All synaptic inputs and outputs of a neuron can only be visualized with methods that have better resolution than the diffraction limit of light. Electron microscopy (EM) is the first method that allowed reliable synaptic identification (De Robertis, 1959) and still used as an essential method, especially in the characterization of densely packed ganglia (Lichtman and Denk, 2011). The pre- and post- synaptic partners can be identified via EM sections with ~100 nm thickness by presynaptic swellings containing vesicles and post-synaptic densities, respectively. Since many sections are needed for the reliable identification of

these synapses and since EM is a method that has very low throughput, serial-section EM (ssEM) methods were developed. Although the first applications of ssEM is dependent on manual sectioning, imaging, and tracing (White et al., 1976); automated methods were developed to provide high-throughput imaging as well as better Z-resolution (Briggman and Bock, 2012).

3.3.2. The *C. elegans* connectome

The first complete map of the entire nervous system (the connectome) was generated by ssEM using *C. elegans* (White et al., 1986). The selection of this organism was based on having a small nervous system with 302 neurons that exhibits stereotypic development. To generate this map, overlapping reconstructions of three different worms were used in the original study (White et al., 1986). Later, additional efforts were made to improve and revise the *C. elegans* connectome. These efforts include imaging additional EM sections from the original samples (Varshney et al., 2011) and re-annotations of the original EM micrographs (Cook et al., 2019; Jarrell et al., 2012). The newest effort by Cook *et al.* also provided additional connections with extrapolation and educated guesses (Cook et al., 2019); thus, the number of connections is significantly increased in this version of reconstruction. Same study also reconstructed the connectome of male worms which has substantially more neurons and connections compared to the hermaphrodite (Cook et al., 2019). Apart from the number of connections between two connectome reconstructions (Varshney et al., 2011 and Cook et al., 2019) which are not similar; the quantification of the weights of the connections are also different. Cook *et al.* estimated the weight of a connection by counting the number of EM sections traversed through the synaptic structure (Cook et al., 2019). On the other hand, Varshney *et al.* determined the synaptic value of the neurons by taking the values from White *et al.* which only counts the number of synapses between two neurons with one modification: they divide it between the left and right neurons proportionally to the values in electron micrographs (Varshney et al., 2011).

Importantly, the currently available *C. elegans* connectome does not include any information about the sign of the connections since it is not possible to determine the polarity of a synapse (inhibitory or excitatory) from electron micrographs of *C. elegans* (Varshney et al., 2011). There are few assumptions that could be made: in the *C. elegans*

nervous system GABAergic neurons were shown to make inhibitory synapses while cholinergic and glutamatergic neurons make excitatory synapses (Brownlee and Fairweather, 1999). Nevertheless, there are exceptions to these approximations such as inhibition of AIZ neurons via cholinergic AIY neurons (Li et al., 2014) and inhibition of AIB neurons through glutamatergic AWC neurons (Chalasani et al., 2007). There might be other examples of such exceptions across the network but since electrophysiology experiments are difficult to perform for every possible synaptic couple, the current knowledge is still not complete. Having said that, new techniques like optogenetic methods and calcium imaging, will increase the speed of acquiring knowledge about signs of all connections and eventually generate a signed connectome.

Throughout this thesis the reconstruction from Varshney *et al.* is used as the *C. elegans* connectome. This connectome consists of 279 neurons instead of 302 neurons because 20 neurons that belong to the pharyngeal nervous system and 3 neuron classes (CANL/R and VC06) which do not make synapses with other neurons are excluded (Varshney et al., 2011). In total this connectome consists of 6393 chemical synapses, 890 gap junctions (Varshney et al., 2011).

Although the overall pattern of connections between electrical and chemical synapses are similar, there are some notable differences. First, there are certain layers within sensory processing where gap junctions are more dominant (Hall, 2017). The interneuron class RMG is suggested to form a ‘hub-and-spoke’ pattern where multiple head sensors converge via gap junctions to it (Macosko et al., 2009). Furthermore, gap junctions connect bilateral left and right pairs of the same neuron classes. Other network properties of the connectome will be referred in more detail in the following sections (see Chapters 3.3.2 and 3.4). The *C. elegans* connectome is still the only complete map of the nervous system and provides a powerful tool and guide in neuroscience (see Chapter 3.3.4).

Recently another study increased the number of connectomes for *C. elegans* using many animals from different developmental stages (Witvliet et al., 2020). These stages include four L1, one L2, one L3 and two adult animals (Witvliet et al., 2020). In higher organisms the macroscale connectivity patterns are better conserved between individuals whereas microscale connectivity exhibits structural variability between individuals (Sporns et al.,

2005). In invertebrates such as *C. elegans*, the small nervous system is thought to be under higher pressure for precise and optimal wiring (Chklovskii et al., 2002); thus, the connectome itself is thought to be more stereotypic and have less inter-individual variability. However, one cannot exclude that there is variability between the connection strength of two neurons or even between synaptic partners of neurons from animal to animal. Throughout this thesis adult hermaphrodite worms are used for the experiments and consecutive analyses. Witvliet *et al.* reported that variable and stable connections each represent ~43 percent of the total connections in adult worms while ~14% of the connections are classified as developmentally dynamic (Witvliet et al., 2020). Furthermore, connections that are classified as stable constitute more synapses and form ~72% of all observed synapses (Witvliet et al., 2020).

3.3.3. Other efforts of connectomes

With the development of methods in EM in the recent years other efforts to assemble partial reconstructions of the nervous system is carried out for other invertebrates. These studies include *Pristionchus pacificus* (Hong et al., 2019) and *Ciona intestinalis* (Ryan et al., 2016) which consists of similar sized nervous systems in terms of cell number compared to *C. elegans*. Furthermore, for larger nervous systems of invertebrates such as the larval *Drosophila melanogaster* (Schneider-Mizell et al., 2016) and *Platynereis dumerilii* (Randel et al., 2015) brain-wide ssEM sections were acquired. Recently, a dense reconstruction of a portion of the fly brain was assembled (Scheffer et al., 2020). Because of the size and numerical complexity of brains of larger animals and vertebrates, full connectomes are still not feasible to map: synapse-resolution mapping is restricted to only sparse labeling (Bock et al., 2011; Motta et al., 2019), subregions of brains (Eichler et al., 2017; Helmstaedter et al., 2013; Takemura et al., 2017; Takemura et al., 2013) or partial reconstructions based on community efforts for completion (Hildebrand et al., 2017; Zheng et al., 2018). Reconstruction of a complete mouse connectome will be a major effort that needs the collaboration of many research groups and years of work (Abbott et al., 2020).

3.3.4. Comparative connectomics

With the availability of functional and structural connectomes from many species across many scales, the study of comparative connectomics emerged in the recent years.

Although many connectomes were mapped using different techniques, the data is still comparable in terms of networks using graph theoretical methods (van den Heuvel et al., 2016). Here, the goal is to compare the network organization of these nervous systems by quantifying the topological features with many network measures that is specialized to characterize different aspects of the network. The common conclusion from these studies and analyses is the presence of similar topological features across many scales in different organisms which suggest the importance of such features since they are conserved in many species and in many scales, ranging from worms (microscale) to fruit flies (mesoscale) and to macaques and humans (macroscale) (van den Heuvel et al., 2016). In the following sections these network measures will be generally defined for brain networks and then specifically for the *C. elegans* connectome where available.

3.4. Network measures in general and in the *C. elegans* connectome

Nervous systems can be represented as networks where neurons are nodes and connections between them are edges. Many network measures from graph theoretical approaches were adopted in neuroscience to characterize different aspects of global or local connectivities in the brain (Rubinov and Sporns, 2010). In this study many network measures that focus on integration, segregation or resilience of the network were used. **Fig.3.2** illustrates some basic concepts in these network measures which will be defined both for general brain networks and the *C. elegans* connectome in the following sections.

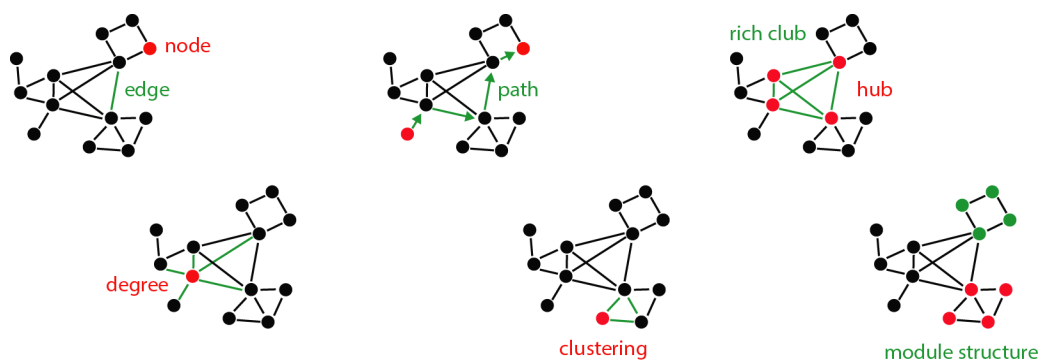


Figure 3.2. Illustration of basic concepts regarding network measures.

Figure illustrates left to right: depiction of **nodes** and **edges**, the metric of **degree**, a shortest **path** between two nodes, the metric of **clustering**, **rich club** organization and **hub** nodes, **modules** that are densely interconnected within the network. Illustrations are adapted and modified from van den Heuvel et al., 2016.

3.4.1. Measures of functional segregation

Functional segregation represents the ability of brain to perform specialized functions in subgroups of neurons which are highly interconnected to each other compared to the average of the whole network (Rubinov and Sporns, 2010). Different studies using various brain networks with different scales have reported that these specialized units (modules) are present in anatomical and functional maps and proposed to be responsible for different functions (Ferrarini et al., 2009; Honey et al., 2007; Sporns and Kötter, 2004).

3.4.1.1. Modules and modularity

One essential measure of segregation focuses on the search and quantification of the presence of modules within the network. This search could be done on anatomical or functional networks and will have different outcomes accordingly. The presence of modules in an anatomical network suggests that these networks are functionally segregated (Rubinov and Sporns, 2010). For instance, a local module is responsible for a specific behaviour such as visual region in cortex. On the other hand, the presence of modules in functional networks suggests there is organizational layers within the network and the segregation is available on neuronal processing level (Rubinov and Sporns, 2010).

Whether analyzed on anatomical or functional layers, these modules can be found in networks using complex algorithms. These algorithms reveal the modular structure of a network by finding the exact size and composition of these individual modules by an iterative approach that gradually divides the network into subgroups with the goal of having maximum possible intra-connections (within the modules) and minimal possible inter-connections (between modules) (Girvan and Newman, 2002). To which extent a network can be divided into defined non-overlapping modules is then quantified by the modularity score Q (Newman, 2004). This metric is quantified as the ratio of interconnections within the modules divided by the average connections within the network (Newman, 2004). Importantly, unlike the other network measures that is defined in this section, the calculated modular structure for a given network is an estimation of optimization algorithms instead of being exactly calculated. Various algorithms are generated to suit the complexity and size of the network as well as required

computational power (Rubinov and Sporns, 2010). In this study, modularity is calculated as the Q of the whole network using an algorithm that searches for non-overlapping modules and which is generalized for weighted and directed networks (Leicht and Newman, 2008).

In the *C. elegans* connectome, two previous studies did similar analyses and characterized the modules within the connectome. Pan *et al.* and Sohn *et al.* found 6 and 5 modules within the connectome, respectively (Pan *et al.*, 2010; Sohn *et al.*, 2011). The members of communities in two different studies are generally similar with the exception that one module in (Sohn *et al.*, 2011) is further divided into two distinct modules in (Pan *et al.*, 2010). Since the overall module identifications are more interpretable in the study by Sohn *et al.*, the study which elaborated the composition and possible function of these modules, this list of modules is used throughout this thesis for the analysis of the *C. elegans* connectome. Although there are modules that predominantly consist of a single neuron type such as sensory- or motorneurons, all of the modules contain interneurons and many modules have a broad range of neuronal compositions in terms of neuron types (Sohn *et al.*, 2011). The characterized modules correspond to chemosensory and 1st layer interneurons, 2nd layer interneurons, mechanosensory neurons and command interneurons. Importantly, motor neurons from both backward and forward circuits are dispersed into two modules (Sohn *et al.*, 2011).

3.4.1.2. Clustering coefficient and transitivity

These measures of segregation are based on the available triangles within the network (see also Chapter 3.4.6). The fraction of triangles around an individual node is equivalent to the clustering coefficient of that specific node (Watts and Strogatz, 1998). In other words, this measure looks whether the neighbors of a node are also neighbors of each other. For instance, network hubs that are highly interconnected with each other (see Chapter 3.5) will have high clustering coefficient. The mean clustering coefficient of the network is used as a measure which represents the pervasiveness of clustered connectivity around nodes (Rubinov and Sporns, 2010). The mean clustering coefficient is normalized individually for each node and is sensitive to the influence of low degree neurons.

In the *C. elegans* connectome the mean clustering coefficient is $C=0.22$ and $C=0.21$ for chemical synapses and gap-junction network, respectively (Varshney et al., 2011). Importantly, both networks are strongly clustered relative to random networks.

Transitivity is a variation of clustering coefficient which is not defined on individual nodes and while being calculated for the whole network the normalization step is performed collectively (Newman, 2003). Thus, it is less sensitive to impacts of low degree nodes within the network.

3.4.2. Measures of functional integration

Functional integration represents the ability of brain to combine information from distinct subgroups (such as modules) (Rubinov and Sporns, 2010). Thus, measures of functional integration focus on paths within the network which is the common routes between the nodes or modules of a network. The characterization of these paths in the network reveals how fast or easily information can flow between nodes or modules: shorter paths suggest stronger potential of integration. Functional integration measures are often applied to anatomical networks because the functional networks already have information about the information flow, hence, the interpretability of these measures solely on the functional network without the guidance of underlying anatomical architecture is rather difficult (Rubinov and Sporns, 2010).

3.4.2.1. Characteristic path length

The main network measure of integration is called characteristic path length and it is calculated as the average shortest path length of the whole network (Watts and Strogatz, 1998). It is a commonly used indicator to assess the integration level of the network, the lower characteristic path length indicates a more integrated network where information can be transmitted from any neuron to another in the network within only few steps. The characteristic path length of the *C. elegans* network is 2.65 and is comparable to random networks (2.25) rendering the connectome a highly integrated network (Watts and Strogatz, 1998).

3.4.3. Measures of centrality

As described in the previous sections, networks are integrated, and the functional integration of the network is often carried out by network hubs which can be brain

regions or individual neurons. The importance of these hubs in terms of the information flow is analyzed by measures of centrality. Although motifs and other main network measures such as degree can be used to detect these central regions within the network, there are other measures specifically focus on characterizing the influence of a node to the network (Rubinov and Sporns, 2010).

3.4.3.1. Betweenness centrality and eigenvector centrality

The shortest paths in the network (see Chapter 3.4.2.1) are crucial for measures of centrality: to control the flow of information these paths must cross through the central nodes within the network (Freeman, 1978). Betweenness centrality is a measure that captures this feature. It is defined as the fraction of all shortest paths in the network that crosses a node. For instance, network hubs that bridge modules have high betweenness centrality. Eigenvector centrality on the other hand, first ranks all the nodes that have high connections, but with the difference that a high scored node is also connected to nodes which also have high scores (Rubinov and Sporns, 2010). For instance, by definition rich club neurons have both high betweenness and eigenvector centrality values (see Chapter 3.5).

3.4.4. Measures of resilience

Network measures of resilience focuses on vulnerability of a network to perturbations. The extent of functional deterioration after a perturbation relies on which brain regions or connections are affected. For instance, enduring degenerative change in Alzheimer's disease or deterioration of brain functions due to a stroke is dependent on the location of the perturbation and connectivity of that region (Rubinov and Sporns, 2010). Degree distribution itself is proposed to indicate resilience of the network (see Chapter 3.4.4.1) (Barabasi and Albert, 1999). For example, a network with power-law degree distribution is considered resilient to random perturbations but vulnerable to targeted high-degree node perturbations.

3.4.4.1. Degree

Degree is a basic but an important measure in the network and degree of a node (neuron) is equal to the number of links connected to that node. In other words, it quantifies the number of synaptic partners or neighbours within the network. Thus, individual values

of degrees will represent the importance of the neuron in that network: highest degree neurons within the network constitute the network hubs. Importantly, the degrees of all neurons make up the degree distribution of the network which is an important indicator of resilience of a network. Since it represents the resilience of networks, the degree distribution is often preserved as an important factor of the network when control experiments are performed with randomization of the connections within a network. If the degree distribution is uniform, it indicates a network where the neurons are distributed homogeneously, whereas a skewed degree distribution suggests there are important hubs in the network and also peripheral neurons with only few connections. These peripheries could be at the sensory level or at the output motor layer. This kind of degree distributions are also a prerequisite for the formation of rich-club organization (Colizza et al., 2006) (see Chapter 3.5).

The connectome of *C. elegans* has a skewed degree distribution where many interneurons (especially command interneurons) have high degrees which is accompanied by low degree neurons distributed within many layers of the network (as sensory-, inter- and motoneurons).

3.4.4.2. Assortativity coefficient

An important measure of resilience is assortativity coefficient which is defined as the correlation coefficient between the degrees of all nodes on opposite ends of a link (Newman, 2002). In this context a positive assortativity coefficient indicates a resilient organization of interconnected network hubs (such as a core of the network) whereas a negative assortativity coefficient suggests a distributed hubs that are not highly interconnected and hence vulnerable to perturbation (Rubinov and Sporns, 2010).

3.4.5. Small-world property

Anatomical architecture of the nervous systems must meet opposing demands at the same time: functional integration and segregation (Tononi et al., 1994). Consequently, networks must include specialized subgroups with various functions (segregation, see Measures of Functional Segregation) which are at the same time linked with inter-modular connections (integration, see Measures of Functional Integration) to form coherent behaviour or to carry out complex computations. The ability to meet both of

these opposing demands in the organization of networks is termed as the small-world property and found in many anatomical and functional networks (Bassett and Bullmore, 2006). In general definition, small-world networks are significantly more clustered than random networks while keeping the characteristic path length of the network low: equal or less than random networks (Watts and Strogatz, 1998). Network Small-world-ness, a recent measure focuses on this aspect of the networks, takes into account both of these properties and calculated as a single metric (Humphries and Gurney, 2008).

With a characteristic path length of 2.65 (compared to 2.25 of random networks) and a clustering coefficient of 0.28 (compared to 0.05 of random networks), the *C. elegans* connectome is characterized to exhibit small-world property (Watts and Strogatz, 1998)

3.4.6. Connectivity motifs

Motifs are specific configurations of how different nodes in a network (e.g. neurons in the nervous system) are connected to each other. They can be seen as the building blocks that form the complex connectomes. Motifs are well studied in both biological networks with different scales (Perin et al., 2011; Song et al., 2005; Varshney et al., 2011), as well as in artificial networks (Milo et al., 2002). Motifs are classified according to the number of nodes they consist of and further separated according to the number and pattern of the connections within these nodes (e.g. a triplet motif with 2 connections is available in **Fig.3.3 A** as ID#1). Since the increased number of combinations within the motifs increases drastically with the number of nodes and also with variations such as different connection types and cell types, the analyses of motifs are usually restricted to small motifs (n=2,3,4) (Gal et al., 2017; Haeusler et al., 2009; Perin et al., 2011; Rieubland et al., 2014; Song et al., 2005; Varshney et al., 2011). There are two main definitions of motifs as “structural motifs” and “functional motifs” (Sporns and Kötter, 2004). Although both definitions are based on the anatomical structure of the network, in other words they look for the anatomical substrates of the network, one of them is called structural, because it only considers how a certain group of nodes are exactly connected.

The other is called functional because it also considers the activation of a subgroup of interconnections within a motif (**Fig.3.3 B**).

Thus, the functional motifs are contained within the structural motifs. In other words, only a portion of the anatomical circuit can be used by the network at a given time, hence, many possible subsets of connectivity patterns can exist embedded within the anatomical motif. Throughout this thesis, structural motif approach is implemented; thus, connectivity motifs were searched for the exact connectivity pattern within neurons (see Methods). Counting the same circuit repeatedly which might result in highly inflated motif statistics is avoided with this approach.

In a network, the number of nodes (neurons) and edges (connections) affects the number of observed motifs. However, even these two parameters are held constant, different connection patterns will lead to different repertoires of motifs in terms of diversity (how

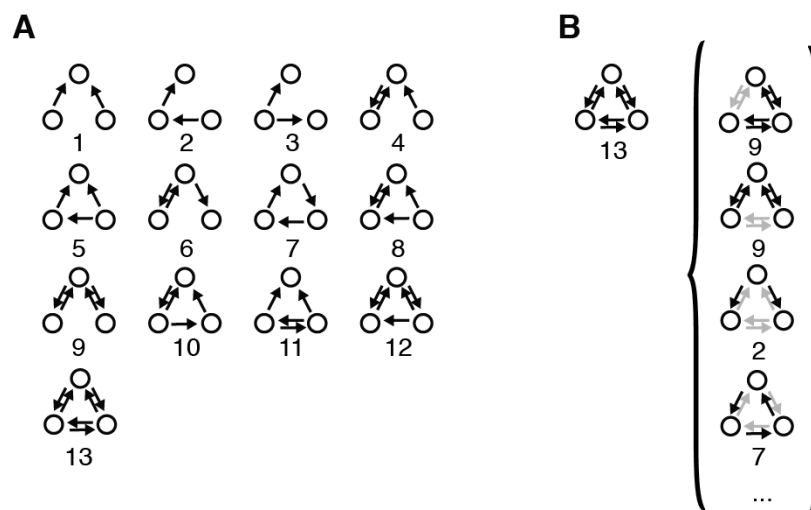


Figure 3.3. Definition of structural and functional motifs.

(A) For the motif size $n = 3$, there are 13 structural motif classes. Numbers refer to motif ID. Structural motifs reflect the exact connection pattern between nodes.

(B) A single instance of a structural motif contains many functional motifs. A structural motif (ID#13) can contain two instances of functional motif ID#9, one motif ID#2 and one motif ID#7. Many other distinct instances of functional motifs are also present but not shown.

many types of motif classes are present) and number (how frequent a certain motif class is observed) (Sporns and Kötter, 2004). It is hypothesized that a large functional repertoire is essential for dynamic and flexible processing, on the other hand, a small structural repertoire is needed for efficient encoding (Sporns and Kötter, 2004). When compared to random networks, biological systems were shown to exhibit higher functional motif repertoire by maximizing the number and diversity of motifs while

maintaining relatively low structural motif number and diversity (Sporns and Kötter, 2004).

In the *C. elegans* connectome certain dyad and triplet motif classes are over-represented (Cook et al., 2019; Qian et al., 2011; Reigl et al., 2004; Varshney et al., 2011) suggesting the network architecture is highly non-random and the over-represented motifs might have a role in the function of neurons.

3.4.7. Symmetry in the networks

Synchronies in networks is a well-studied concept in many complex systems including neuronal networks. Cluster synchronization is a sub-element of this concept where partial synchronization emerges as confined in clusters instead of expanding to the whole network. It has been shown that intrinsic network symmetries are crucial in the generation and maintenance of these synchronizations (Pecora et al., 2014).

In the *C. elegans* connectome it is previously shown that symmetries exist in connectivity patterns of different neuron types. For instance, majority of sensory and interneurons contain bilaterally symmetric L-R neurons, and their connectivity patterns are also symmetric (Varshney et al., 2011). Moreover, the body motor neurons that reside along the anterior-posterior axis of the ventral cord of the animal exist in repeating groups and head motor neurons exhibit four and six-fold symmetry (Varshney et al., 2011). Furthermore, pseudo-symmetries are characterized in the *C. elegans* connectome (Morone and Makse, 2019) that are crucial for the two main locomotory circuits of the animal which are responsible for backward and forward motion. The symmetric structures found throughout the connectome could have important functional relevance for generating synchronous and coordinated activity patterns.

3.5. Rich club neurons in brain networks and in the *C. elegans* connectome

Rich-club organization is an important feature of networks described first for internet (Zhou and Mondragon, 2004), for various complex networks (Colizza et al., 2006), for the human connectome (van den Heuvel and Sporns, 2011) as well as the *C. elegans* connectome (Towlson et al., 2013). The prerequisite is having a heavy-tailed distribution of degrees within the network that suggests the existence of highly connected regions

which is in fact the case for human brain (Hagmann et al., 2008) or small nervous systems (Varshney et al., 2011). In order to be defined as a rich-club, the nodes with the highest number of links (hubs) must interconnect amongst themselves instead of low-degree nodes to form subgraphs (clubs) (Colizza et al., 2006). It is defined by calculating the rich club coefficient of the network and generating a curve with the gradual removal of nodes by an increasing degree threshold. This curve is then compared to randomized versions of the same network to identify the presence of a rich-club and if available followed by the characterization of the members of this club (see Methods).

Rich club neurons were found in many brain networks in across many scales including worms (Towlson et al., 2013), fruit flies (Shih et al., 2015), mice (Rubinov et al., 2015), cats (de Reus and van den Heuvel, 2013), macaques (Goulas et al., 2014; Harriger et al., 2012) and humans (Goulas et al., 2014; van den Heuvel and Sporns, 2011). Rich club neurons play a key role at the information flow and communication within the network by being embedded in the network topology (de Reus and van den Heuvel, 2014). These neurons are considered as the connective core of the network (Shanahan, 2012) that binds different segregated circuits and thus crucial for the integration of the network (see Chapter 3.4.2). This topological integration -bridging distributed domains together via rich club neurons and their high interconnection rate amongst each other- has a high wiring cost for the networks (van den Heuvel et al., 2016). For instance, in *Drosophila* rich club regions are located across all modules of the nervous system with remote placement in terms of exact location of the regions (Shih et al., 2015) that significantly increases the wiring cost of the network. Similarly, mouse connectome also exhibits a modular structure that are connected to each other by rich club neurons via costly long-distance connections (Rubinov et al., 2015).

Rich club neurons within the *C. elegans* connectome are also distributed along the two main ganglia of the nervous system (Towlson et al., 2013) and provide the long connections across the body axis of the animal which increases the total wiring cost of the whole network. However, the observation of similar structures in many networks across many scales that have evolved independently suggests a functional role for this organization. Furthermore, in *C. elegans*, rich club neurons are the first neurons to be generated within the nervous system (Towlson et al., 2013), corroborating the functional role and importance of this architecture in the development of nervous systems.

In parallel, hubs within the network have been shown to play important roles in shaping neural dynamics. A subset of high-degree neurons is shown to be responsible for network synchronization in hippocampus (Bonifazi et al., 2009) and entorhinal cortex (Mòdol et al., 2017) and for the transfer of information in local cortical networks (Nigam et al., 2016). These studies support the idea that rich club neurons play a key role in networks which compensates their high wiring cost through long-distance synaptic connections at network integration.

The rich club neurons in the *C. elegans* chemical synapse network were previously characterized and consist of 14 neurons: AVAL/R, AVBL/R, AVDL/R, AVEL/R, PVCL/R, DVA, AIBR, RIBL and RIAR (Towlson et al., 2013). These neurons have high degrees, participation coefficients and betweenness centrality ranks in the network (Towlson et al., 2013) (see Chapter 3.4). These neurons are distributed to two different ganglia of the animal, thus have a significantly high average connection distance (Towlson et al., 2013). 48% of the total wiring cost of the whole network belongs to the connections to rich club neurons while these neurons constitute only 4% of the neurons (Towlson et al., 2013). Consequently, they were proposed to play a central role in the integration of the whole network.

3.6. Functional activity measures

Throughout this thesis calcium signals are used as a proxy for neuronal activity (see Chapter 3.1) and functional interactions between neurons are examined using various methods. These methods include linear methods such as correlation, its variant cross-correlation and covariance. Additionally, since nonlinearities in neuronal interactions such as oscillations, state transitions, attractor dynamics and conditional dependencies exist (Bassett and Sporns, 2017; Curto and Morrison, 2019); nonlinear methods are also included in the analyses.

3.6.1. Linear measures

In statistics, covariance is a measure which quantifies the joint variability of two random variables (Rice, 2006). It measures whether the variables tend to show similar trends. For instance, if greater values in a variable corresponds to greater values of the other variable, covariance is positive. The sign of covariance shows the tendency of the linear

relationship between them (Rice, 2006). The absolute value of covariance is not straightforward to interpret. Correlation coefficient on the other hand, is the ratio between the covariance of two variables and the product of their standard deviations. Hence, it can be regarded as the normalized version of covariance which will generate a value between -1 and 1. Thus, the absolute value of correlation coefficient reflects the strength of the linear relationship. Cross-correlation is quantification of the correlation coefficient between the variables by introducing a systematic time lag which produces a series of coefficients. Maximum values of these coefficients (or minimum in case of anti-correlations) will then be searched to reflect the best linear relationship between two variables and the corresponding time lag will represent their temporal relation. All three these measures can only represent a linear correlation and ignores other types of relationships within the datasets.

3.6.2. Non-linear measures

In information theory, if the knowledge about the state of a variable reduces the uncertainty about the state of another variable, the first variable is regarded as containing information about the second variable (Cover and Thomas, 2006). Mutual information (MI) is the measure that quantifies this statistical dependence between two variables (Cover and Thomas, 2006; Shannon, 1948). It is also widely used in neuroscience to study neural activity and their relations to one another (Ince et al., 2017). It is based on the quantification of uncertainty (entropy) to quantify the reduction in uncertainty on the second variable which provides information. The unit of MI is bits which is a measure of entropy. Importantly, MI can detect non-linear interactions but the resulting values of MI do not describe a model for the underlying relationship between variables (Timme and Lapish, 2018).

Another non-linear measure used in this study is based on covariograms which is a variant of cross-correlation analysis. This method is based on peri-event time histograms followed by a shuffle-correction procedure (Brody, 1999; Kaplan et al., 2020). Covariograms report the frequency of a target neuron's peak at different time delays relative to a reference neuron's peak; hence, it depends on the discretization of the data and is therefore insensitive to the shape of calcium signals (Brody, 1999; Kaplan et al., 2020). Importantly, covariogram-analysis represents a directed (asymmetric) measure of functional interactions.

3.7. Systematic interrogation of neurons

An important part of this study is to test and validate the structure-function relationships found in wild-type animals with the perturbation of the brain via systematic inhibition of neurons. The main method of neuronal inhibition throughout this thesis is the delivery of transgenic histamine gated chloride (HisCl) channels which leads to rapid inhibition of neural activity. These channels were characterized in *Drosophila* (Gisselmann et al., 2002) and validated to be working in *C. elegans* by various studies including our lab (Kato et al., 2015; Pokala et al., 2014). It is based on the expression of transgenic channels that leads to rapid inhibition of the targeted neuron upon histamine uptake by the animals. Histamine is not synthesized or used as an endogenous neurotransmitter by *C. elegans*, the effect of HisCl channels is restricted to only to neurons that transgenically express these channels without any collateral effects to other neurons (Kato et al., 2015; Pokala et al., 2014). The main advantage of the approach is its simplicity while still providing the temporal control of the inhibition which bypasses the possible developmental defects. Unlike other perturbations such as optogenetics, HisCl method does not provide an acute inhibition. Thus, the exact dynamics of the transition from unperturbed to perturbed brain states cannot be observed. Instead, the targeted neurons are inhibited beforehand in an incubation phase (see Methods) and the experiments are carried out with animals that already exhibit perturbed brain dynamics. In the following sections I briefly summarized the known function of the targeted neuron classes in this study and the known effects of their perturbation (ablation, inhibition and activation) in previous studies.

3.7.1. AIB neurons

AIB interneurons have recurrent connections with command interneurons AVA and AVE in the backward movement circuit (White et al., 1986) and functional studies reported that it is important for motor state transitions (Gray et al., 2005). In whole-brain imaging experiments AIB neurons exhibit activity during backward motion (Kato et al., 2015), and laser ablation of AIB resulted in lower frequency of reversals (Gray et al., 2005). Furthermore, optogenetic activation of AIB was reported to trigger reversals (Kocabas et al., 2012; Wang et al., 2020) and optogenetic inhibition resulted in lower reversal frequencies (Kocabas et al., 2012). These results corroborate that AIB is an important interneuron for the backward movement circuit. On the other hand,

optogenetic inhibition of AIB led to abolished omega turns (Wang et al., 2020) indicating that these neurons are also important for reversal to turn transition.

3.7.2. AVA neurons

AVA neurons are the highest degree neurons in the *C. elegans* connectome (Varshney et al., 2011) and the command interneurons responsible for the initiation of backward movement. When AVA neurons are optogenetically activated the animals exhibit backward movement (Schmitt et al., 2012); on the other hand, when AVA neurons are inhibited or ablated the backward movement rates of the animals drastically decrease (Chalfie et al., 1985; Gordus et al., 2015; Liu et al., 2017; Pokala et al., 2014). Acute inhibition of AVA causes long pauses of animals which are then followed by turn events which suggests that AVA neurons are essential for the execution of backward movement (Kato et al., 2015; Pokala et al., 2014). Whole-brain imaging experiments in AVA-inhibited animals showed that cyclical global brain dynamics are retained, suggesting that AVA is important for the initiation of the backward movement as a behaviour but not essential for the generation of brain state responsible for backward movement (Kato et al., 2015). This finding is in parallel with AVA neurons forming a bottleneck between the head ganglia and body motor neurons in the backward movement circuit (White et al., 1986). Furthermore, the A-class ventral cord motor neurons that are the main output of AVA neurons were silenced; however, other interneurons that are participating at the coordinated activity within backward movement brain state, AVE, RIM and AIB, retained their activity patterns (Kato et al., 2015). This result suggests that the long pauses observed in AVA silenced freely-moving animals were going through the backward-movement phase similar to wild-type animals only with the lack of ability of executing them because of AVA inhibition.

3.7.3. AVB neurons

AVB neurons, the command interneurons in the forward movement circuit, are the second highest degree neurons in the *C. elegans* connectome (White et al., 1986) which are thought to control forward motion (Chalfie et al., 1985). As the equivalent of AVA neurons in the forward circuit, these neurons output heavily to B-class motor neurons (White et al., 1986) and form a bottleneck between head ganglia and body motor neurons. Ablation of AVB neurons were shown to increase reversal frequency of the animals

(Rakowski et al., 2013). Furthermore, ablation of AVB neurons reduced forward motion but failed to completely abolish it (Rakowski et al., 2013) suggesting that they are essential for forward motion, but execution of forward movement does not solely depend on their activity. Additionally, optogenetic manipulation of AVB (together with AIY) resulted in promotion of high speed and suppression of reversals at high oxygen concentrations (Laurent et al., 2015). In whole-brain imaging experiments AVB neurons were shown to be strongly active in forward movement brain states (Kato et al., 2015).

3.7.4. AVE neurons

AVE interneurons are one of the command interneurons implicated in backward movement circuit (Chalfie et al., 1985; White et al., 1986). AVE neurons were previously shown to exhibit strong activity in backward motion (Kawano et al., 2011) and backward movement brain states in whole-brain imaging experiments (Kato et al., 2015). Optogenetic activation of AVE resulted in the initiation of backward movements and ablation of AVE resulted in greatly reduced reversal rates (Li et al., 2020). Inhibition of AVE neurons were reported to result in ectopic pausing (Katz et al., 2018) suggesting that they have a function in locomotion quiescence. Unlike AVA command interneurons within the backward circuit, AVE neurons were shown to be dispensable for gentle touch responses in ablation experiments (Li et al., 2011).

3.7.5. RIB neurons

RIB interneurons are located within the forward movement circuit (White et al., 1986) and were shown to be active in forward movement state (Gray et al., 2005; Kato et al., 2015; Li et al., 2014). Optogenetic inhibition of RIB neurons during forward movement resulted in a pause state (Wang et al., 2020); in parallel to these results, RIB neurons were reported to code for the forward speed of the animal (Kato et al., 2015). Consequently, RIB neurons are important for modulation of forward motion (e.g. speed) rather than the execution of forward movement. On the other hand, optogenetic activation of RIB neurons during backward motion resulted in transitions to an omega turn or forward movement (Wang et al., 2020). Furthermore, optogenetic activation of RIB neurons during forward motion initiated omega turns (Wang et al., 2020); thus, these neurons were also reported to be a part of turning module as the modulator of transition between reversal and turning and not only function in the forward movement circuit.

3.7.6. RIM neurons

RIM neurons are motor/interneurons that are part of the backward movement circuit. RIM neurons are one of the few neuron classes that uses tyramine as a neurotransmitter and they were previously shown to prolong backward movement duration via inhibiting AVB, command interneurons responsible for forward movement (Alkema et al., 2005). Moreover, RIM neurons were shown to suppress head oscillations via silencing head muscles (Pirri et al., 2009). Both effects were shown to be executed through tyramine-gated chloride channel LGC-55 (Alkema et al., 2005; Pirri et al., 2009). In behaviour experiments using freely-moving worms, optogenetic activation of RIM neurons initiated backward movement (Gordus et al., 2015); however, inhibition and ablation of these neurons were also reported to increase reversal rate of the animals (Gray et al., 2005; Li et al., 2011). Importantly, RIM neurons were shown to be crucial at generation of variable behavioural responses to external stimuli (Gordus et al., 2015). In whole-brain imaging experiments, RIM neurons were reported to be active during backward movement brain state and strength of their activity was shown to be correlated with reversal speed (Kato et al., 2015).

3.7.7. PVC neurons

PVC neurons are command interneurons for the forward movement circuit (Chalfie et al., 1985) and are one of the highest degree neurons within the *C. elegans* connectome (White et al., 1986). PVC neurons were reported to mediate gentle touch response (Chalfie et al., 1985). Laser ablation of PVC led to abolishment of forward movement upon posterior harsh touch (Li et al., 2011); however, these animals can still perform forward movement to different stimuli such as anus touch responses although with a lower rate (Li et al., 2011). Thus, PVC neurons are only required for the execution of forward movement within specific touch responses and not in general, unlike AVB neurons. PVC neurons were shown to exhibit calcium activity only as a response upon posterior touch stimuli (Li et al., 2011). Optogenetic activation of PVC neurons triggered forward motion and resulted in acceleration of animals during forward movement (Husson et al., 2012).

4. Results

4.1. Coordinated population dynamics in nervous system wide imaging experiments

Recent studies have shown that using *C. elegans* it is possible to perform large-scale calcium imaging with single-cell resolution (Nguyen et al., 2016; Schrödel et al., 2013; Venkatachalam et al., 2016). Calcium imaging experiments revealed coordinated neuronal population dynamics across the nervous system of the worms (Kaplan et al., 2020; Kato et al., 2015; Nichols et al., 2017). A large fraction (~40%) of all neurons participate in these dynamics which correspond to the animals' major motor commands: forward movement, backward movement and turning (see Chapter 3.2.1). Importantly, these dynamics occur in unstimulated and immobilized conditions (Kaplan et al., 2020; Kato et al., 2015; Schrödel et al., 2013). Thus, they do not depend on movement or acute sensory stimulation which suggests that they are driven intrinsically. Consequently, this experimental approach is ideal to study which structural features of the connectome can best predict and support globally correlated brain dynamics. First, to generate a functional connectome which will then be used to delineate structure-function relationships, I extended the previous work of whole-brain imaging experiments in immobilized worms that covered only head ganglia (Kato et al., 2015; Nichols et al., 2017; Schrödel et al., 2013; Skora et al., 2018) with a new chip device which enables the simultaneous imaging of the head and tail ganglia and a subset of neurons located on the ventral cord of the animal. This experimental setup enables the recording of almost all sensory- and interneurons of the animal and many motorneurons (**Fig. 4.1 A**).

Using this approach, I generated six wild-type (WT) datasets from different well-fed adult worms, capturing the GCaMP signals of ~150 neurons per recording (**Fig. 4.1 B**). Then, in order to compare their activity with their connectivity patterns, I identified the vast majority of active neurons (n=50-71) by taking into account their anatomical positions, relation to surrounding neurons as well as their characteristic activity patterns based on previous work (Kato et al., 2015; Nichols et al., 2017; Skora et al., 2018) (see Methods). Furthermore, I identified all active neurons in the tail ganglia, which have not been identified previously, and confirmed all of the previous identities from earlier works using the new NeuroPAL method (Yemini et al., 2021) (**Fig. 4.1 C**). In total, the extension of the whole-brain imaging method to the tail ganglia and posterior part of the

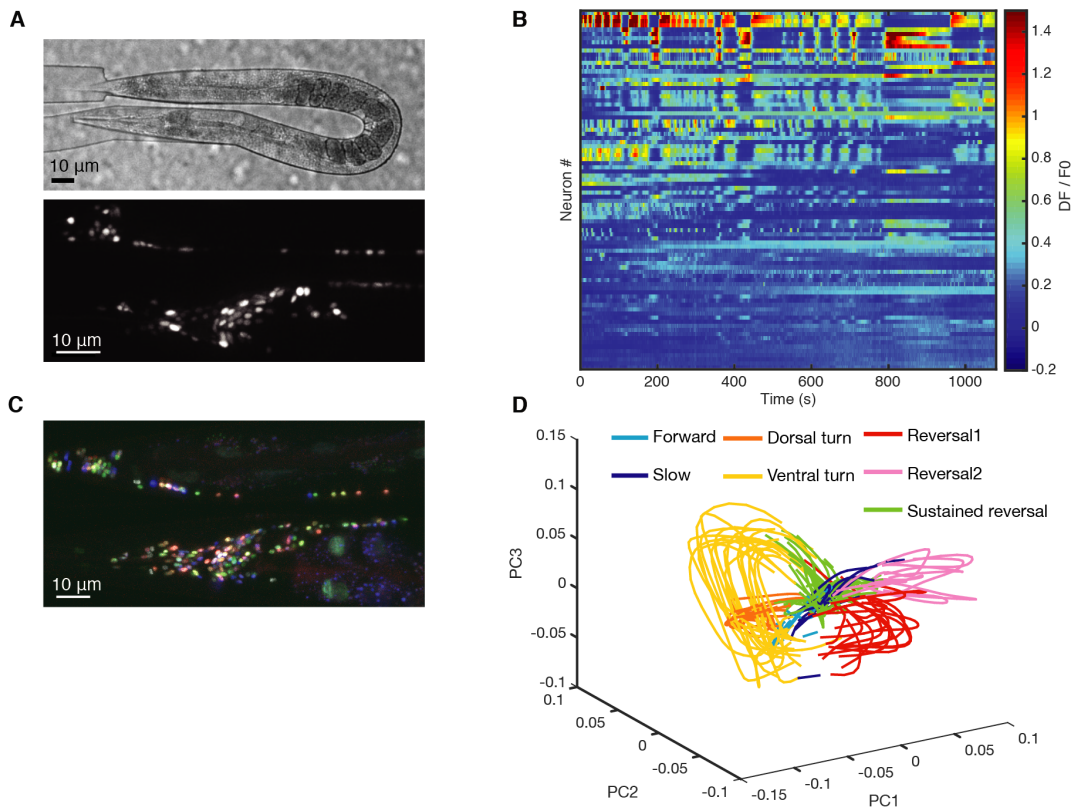


Figure 4.1 Experimental setup for whole-brain head and tail imaging.

(A) Top: Phase-contrast image of an immobilized worm inside the microfluidic device. Bottom: Maximum intensity projection of a representative sample recorded under constant conditions.

(B) A representative 18-min-long whole-brain imaging recording from WT worms, shown as heat map of fluorescence (DF/F0) time series of all detected neurons (154 segmented neurons, one neuron per row, sorted by neuronal activity levels).

(C) Maximum intensity projection of a representative NeuroPAL line (Yemini et al., 2021) sample used for the confirmation of neuronal cell class identities.

(D) Phase plots of first 3 integrated principal components (PCs) of the recording shown in panel B colored by seven-state brain cycle (Kato et al., 2015). Colors indicated by color key.

ventral cord allowed an increase in number of recorded neurons by 33 ± 3.8 and in number of identified neurons by 16 ± 4.6 . These WT datasets also recapitulated the brain dynamics across the neuronal population that was reported and characterized previously using principal components (PC) analysis (Kato et al., 2015): A 3-D visualization of the first 3 PCs on the time derivatives of neuronal activity traces (see Methods) revealed a cyclical manifold where the time evolution of brain states can be observed, and the branches of this manifold represent different command states of the animal (**Fig.4.1. D**). The majority of newly identified neurons within the tail ganglia and the posterior part of the ventral cord mainly contributed to the PC1 which have contributions from neurons implicated in forward and backward movement. To further investigate how population

activity is structured within WT datasets, I calculated the shared dimensionality (Gurnani and Silver, 2021; Owen and Perry, 2009; Stringer et al., 2019) (see Methods) and effective dimensionality (Abbott et al., 2011) (see Methods) and found that the data exhibits a lower bound of 3-5 dimensions (effective dimensionality: 3.34 ± 0.43 , shared dimensionality: 8.17 ± 1.33 , **Fig.4.2**).

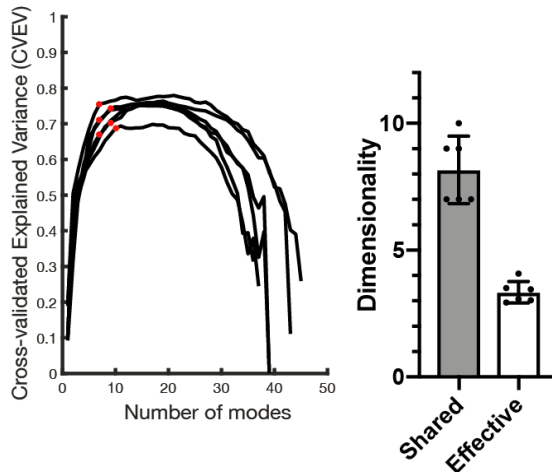


Figure 4.2 Dimensionality analysis of WT datasets.

Left: Relationship between cross validated explained variance (CVEV) and number of population modes. Black curves indicate individual recordings, red circles indicate the changepoint in the curve's slope, corresponding to shared dimensionality for the populations.

Right: Dimensionality of WT datasets calculated as shared and effective. Bars and error bars indicate mean and standard deviation across 6 datasets.

Next, I generated a functional interaction map of the nervous system by calculating the average ($n=2-6$) pairwise correlations between the activity time-series of 66 identified active neurons across all WT datasets (**Fig.4.3 A**). Hereafter I use the term 'functional interaction' to refer to such pairwise measures which potentially capture dynamical relationships between pairs of neurons and which may result from both direct synaptic signaling or indirect coupling via the network. I used agglomerative clustering to reveal correlated structures within the dataset that contribute to the previously characterized global population dynamics (Kato et al., 2015) (see Chapter 3.2.1): reversal neurons were clustered together to form a highly correlated structure and they are strongly anti-correlated with the forward neurons. Plus, head motor neurons that are responsible for dorsal and ventral turns clustered independently. Finally, sensory neurons which exhibit either spontaneous fluctuations or low activity in general and other neurons that does not show a distinct activity pattern of activity were grouped together which generate low or almost no correlation values with the previously indicated clusters (**Fig.4.3 A**). Importantly there are sub-structures observed in high correlation corners in **Fig.4.3 A** which supports the effective and shared dimensionality values calculated earlier in **Fig.4.2**. The histogram of the correlation values in the average correlation matrix shows

the distribution of correlation values within the datasets and shows that the datasets consist of highly correlated and anti-correlated pairs (**Fig 4.3. B**).

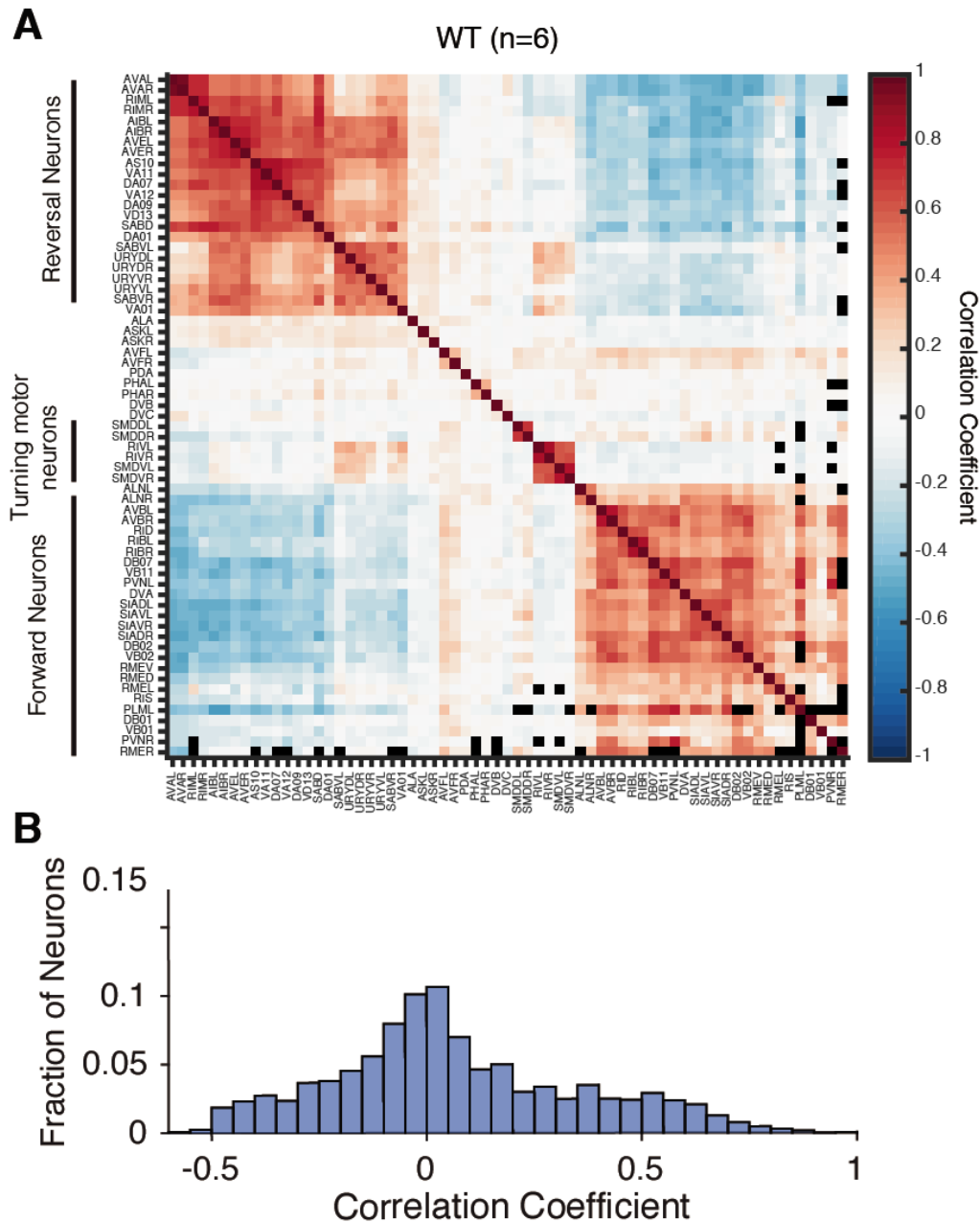


Figure 4.3 Functional interaction map of WT datasets.

(A) Pearson correlation matrix of identified neurons averaged across datasets (n=6 independent recordings of different worms). Correlation coefficients indicated by color key. Neurons are grouped according to hierarchical clustering. Black cells indicate pairs that were never observed simultaneously.

(B) Frequency distribution of average pairwise correlations for WT datasets.

Importantly, pairwise correlations were consistent between individual WT datasets (**Fig.4.4 A**) and have low variation in general when re-analyzed with a leave-one-out procedure (**Fig.4.4 B**). Pairwise correlations were also similar when compared to previous studies that include only head ganglia recordings (**Fig.4.5**). These studies

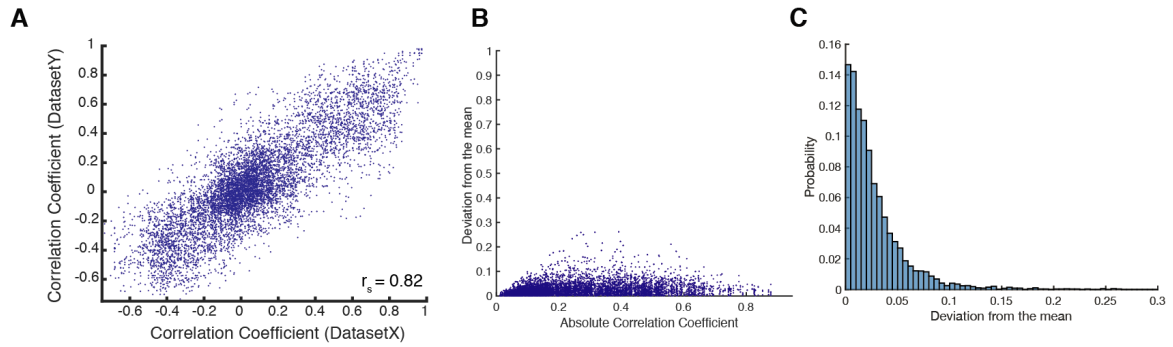


Figure 4.4 Correlation coefficients are robust among different recordings.

(A) Scatter dot plot of correlation values of same neuronal pairs across 6 WT datasets ($n=7930$ pairs). r_s , Spearman's rank correlation coefficient.

(B) Scatter dot plot of correlation values of neuronal pairs across 6 WT datasets and their deviation from the mean after a leave-one-out procedure.

(C) Frequency histogram of the deviation from the mean for each correlation value after a leave-one-out procedure.

include a different developmental stage (L4), a different genetic background (*npr-1* animals) that partly mimic wild isolates of *C. elegans* (De Bono and Bargmann, 1998; McGrath et al., 2009) and animals that were mildly or severely starved (Skora et al., 2018) (**Fig.4.5**). Taken together, these results show that the global correlations under study are robust to different conditions, in parallel with the robustness of the actions they encode (Kato et al., 2015; Nichols et al., 2017; Skora et al., 2018).

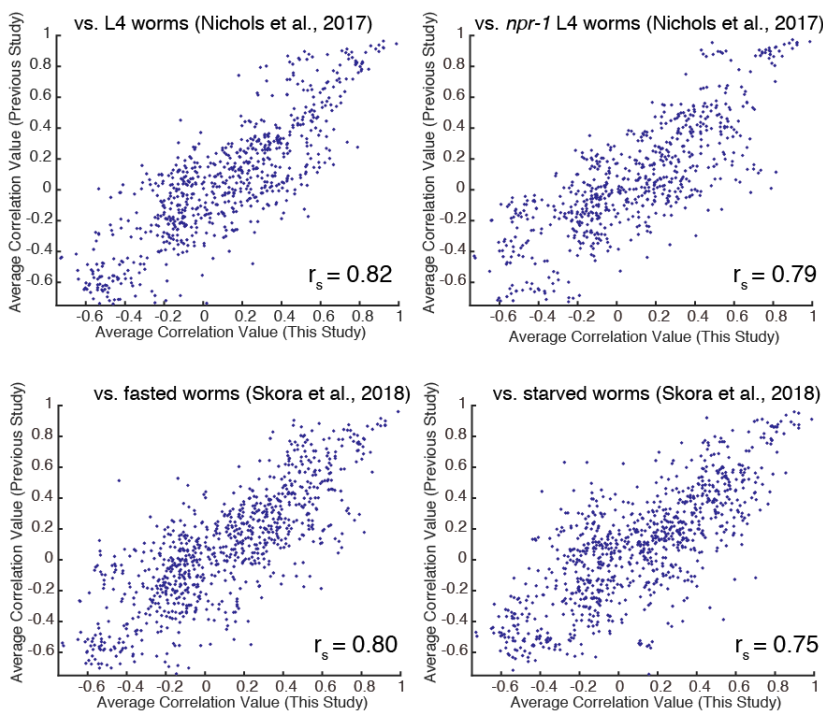


Figure 4.5 Pairwise correlation coefficients are comparable with previous studies.

Scatter dot plot of average correlation values of same neuronal pairs in this study vs. different conditions from indicated previous studies {Nichols,2017; Skora,2018}. r_s , Spearman's rank correlation coefficient.

4.2. Local connectivity patterns predict functional interactions

My first observation between the connectivity of neurons and their activity patterns was a correlation between the degree of a neuron (see Chapter 3.4.4) and its overall activity level (Fig.4.6). This result suggests that neuronal activity levels are influenced by network interactions.

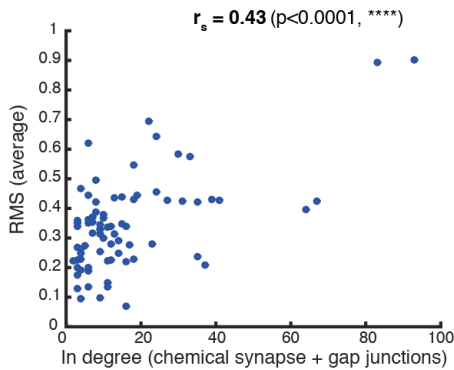


Figure 4.6 Neurons with high in-degrees exhibit stronger neuronal activity levels.

Correlation analysis between in-degrees of neurons (sum of total number of chemical synapses and gap junctions) and neuronal activity levels (RMS). r_s , Spearman's rank correlation coefficient. Permutation test p value estimates the probability that r_s value was obtained by chance in shuffled neuron label trials.

Thus, I further examined the exact connection patterns between neurons to characterize their possible influence on the pairwise correlations. I first classified neuronal pairs by the connection patterns between only two neurons (see Methods) and tested whether this classification enriches functional interactions. The comparison of different connection patterns between neuronal pairs as well as the non-connected pairs revealed that connected neurons are significantly more correlated (Fig.4.7 A).

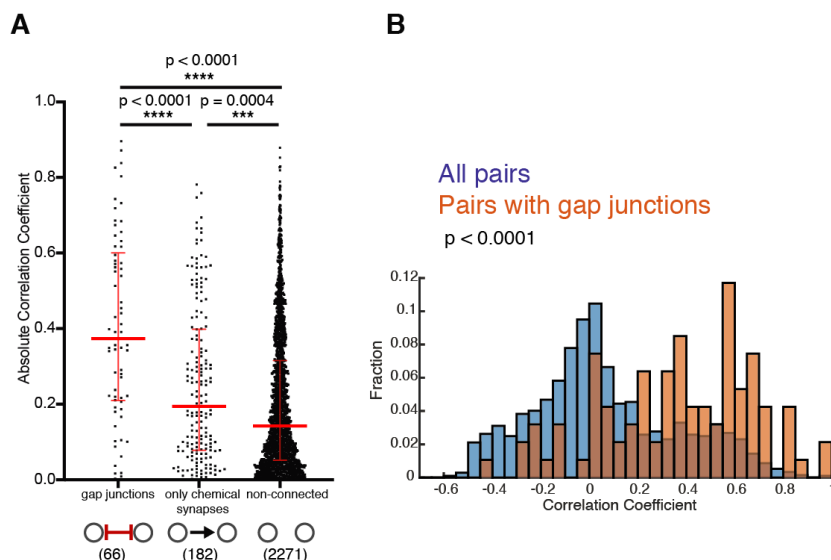


Figure 4.7 Neurons that form gap junctions are highly correlated.

(A) Pairwise correlation grouped by dyad connection pattern. Dots show correlations of individual neuronal pairs, red bars indicate median with interquartile range. Asterisks indicate significance levels after a custom shuffle test. First column: pairs with only gap junctions. Second column: pairs with only unidirectional chemical synapses. Third column: non-connected pairs.

(B) Frequency distribution of correlation values for pairs with gap junctions versus all neuron pairs. Permutation p value estimate the probability that absolute distance between the mean of two distributions was obtained by chance.

Furthermore, I found out that pairs connected exclusively via gap junctions significantly enriched high correlations compared to those connected by only chemical synapses (**Fig.4.7 A**). However, examining distributions revealed many counterexamples: non-connected neurons with high correlations and connected neurons with low correlations (**Fig.4.7 A**). Importantly, I found that neuronal pairs with gap junctions exhibit almost exclusively positive correlations (**Fig.4.7 B**). Next, I tested whether connection strength (number of synapses and gap junctions) can predict the strength of pairwise correlations. Surprisingly I found only a very weak relationship with functional interaction; however, it was statistically significant when compared to random networks (see Methods) (**Fig.4.8**). Moreover, when I repeated the same analysis on a binarized connectome where the weights of the connections were taken out, I obtained a similar weak relationship with functional interaction (Spearman's $r_s = 0.18$ in both cases) suggesting that including all known information about synaptic strength does not improve when compared to a binarized connectome and resulted in a weak relationship with functional interaction.

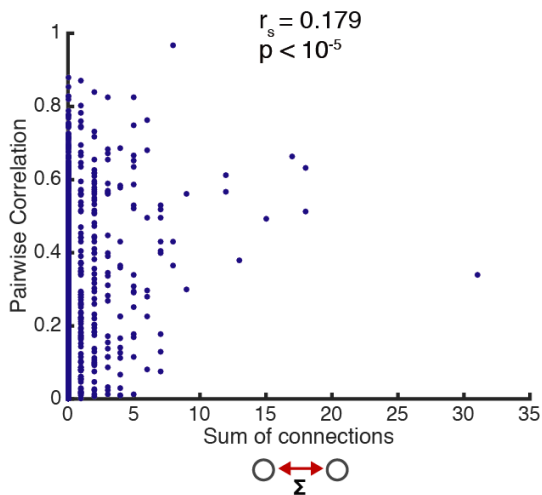


Figure 4.8 Sum of connections is a weak predictor of correlations.

Correlation analysis between pairwise correlations and sum of chemical synapses and gap junctions. r_s , Spearman's rank correlation coefficient. Permutation test p value estimates probability that r_s value was obtained by chance from degree preserved randomized networks.

Since a fraction of neurons that does not have a direct connection exhibit high pairwise correlations (**Fig.4.7 A**) and connectivity between pairs of neurons (whether with or without synaptic weights) provide weak predictive power (**Fig.4.8**), I hypothesized that higher order connectivity features might play a key role at supporting neuronal interactions. To examine their influence, I extended the connectivity analysis to triplet motifs. Neuronal pairs can be connected with gap junctions and chemical synapses via 259 configurations with a third motif member out of 98 possible triplet motif classes (see Methods). 247 of these configurations are observed in the *C. elegans* connectome whereas in my WT datasets I recorded the activity of all three members at least once for 195 of them. These motifs cover 16% of all motifs within the connectome. I shortlisted

25 triplet motifs that significantly enriched pairwise correlations compared to matched controls: pairs that shared the same connectivity but were not part of the triplet motif (Fig.4.9 A; see Methods). I henceforth refer to these motifs as ‘significant motifs’ (Fig.4.9 A). A typical feature I found across these significant motifs was the presence of a common input to the pair (22/25 motifs, $p=0.002$ expected chance level, Fig.4.9 A, red shade). Pooling all motifs that contain a common input significantly enriched pairwise correlations (Fig.4.9 B), suggesting that this common feature was more relevant than any specific motif configuration. Therefore, I further shortlisted 10 motifs that significantly enrich pairwise correlations compared to the pooled set of all common-input-motifs (Fig.4.9 A, black box).

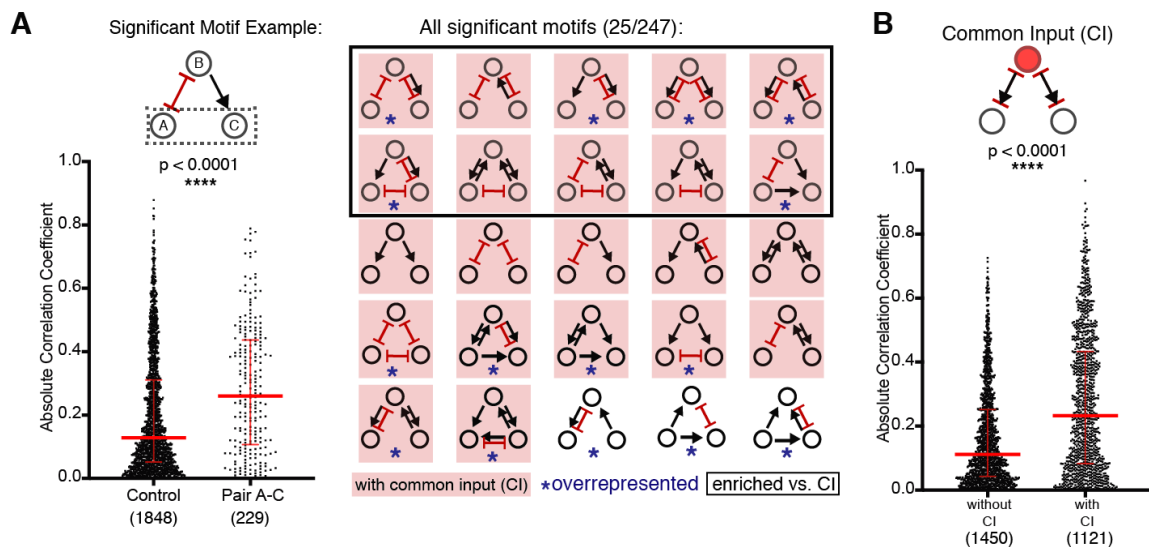


Figure 4.9 A shortlist of triplet motifs and common input predict neuronal interactions.

(A) Left, top: example significant triplet motif. Black arrow indicates chemical synapse (directed), red line indicates gap junctions (undirected). Left, bottom: pairwise correlations in all pairs A-C with above motif vs matched control. Dots show correlations of individual neuronal pairs, red bars indicate median with interquartile range. Significance was tested with Mann-Whitney test. Right: list of all significant triplet motifs. Red shades indicate motifs where B is a common input to A-C. Black box indicates the motifs that predict significantly higher correlations than the combined set of all common input motifs. Blue asterisks indicate motifs that are over-represented in the connectome compared to random networks.

(B) Top: schematic showing a source of common input within the triplet motifs. Bottom: Pairwise correlations within triplet motifs grouped by motifs with ($n=103$) and without ($n=156$) common input (CI). Dots show correlations of individual neuronal pairs, red bars indicate median with interquartile range. Asterisks indicate significance level after a custom shuffle test.

Next, I checked the occurrences of the triplet motifs in the *C. elegans* connectome compared to random networks (Fig.4.10 A) and I found that many significant motifs were also over-represented in the connectome (13/25, $p=0.052$, Fig.4.9 A, blue asterisks, see Methods). Moreover, I analyzed the general set of over-represented and under-

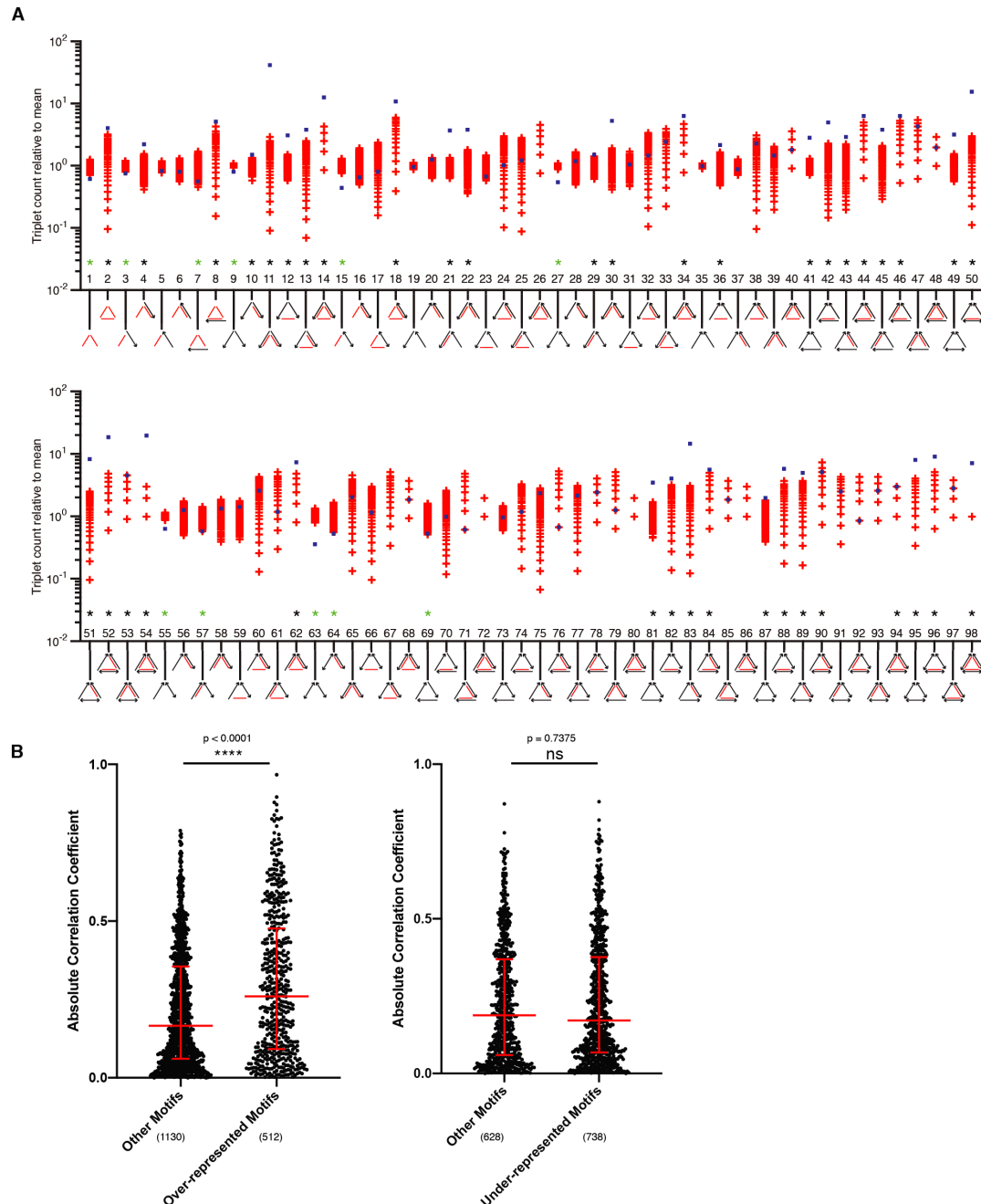


Figure 4.10 Over-represented triplet connectivity motifs have a functional role in the network.

(A) The ratio of the triplet connectivity motifs compared to the mean of a random network ensemble ($n=10^5$). Blue squares indicate the occurrence of motifs in the *C. elegans* connectome and red crosses indicate occurrences in randomized networks. Black and green asterisks indicate over-represented and under-represented motifs after single-step min p procedure for multiple hypothesis correction, respectively. * $p < 0.05$.

(B) Pairwise correlation grouped by motif membership. Dots show correlations of individual neuronal pairs, red bars indicate median with interquartile range. Asterisks indicate significance levels after a custom shuffle test. ****, $p < 0.0001$; * $p < 0.05$, ns, not significant. Numbers in parentheses indicate number of individual neuron pairs in scatter plots.

represented set of motifs within the connectome to find out that over-represented motifs have significantly higher correlation values (**Fig.4.10 B**) which further suggests a

potential functional role in the network.

Taken together, these analyses suggest a shortlist of triplet motifs and common input, as important structural elements that support pairwise correlations between neurons by recruiting them to global activity patterns that are observed in whole-brain imaging datasets. Importantly, both could account for functional interactions between unconnected pairs.

4.3. Neuronal identity and input similarities predict neuronal interactions

The nervous system of *C. elegans* is bilaterally symmetric and majority of the neuron classes are present as symmetric left and right (L-R) pairs (Hobert et al., 2002) (**Fig.4.11 A**). I found that within my datasets these L-R pairs are highly correlated (**Fig.4.11 B**) and exhibit solely positive correlations (**Fig.4.11 C**). Critically, L-R pairs constitute less than 1% of all connected neuronal pairs in my datasets ($n=20$ vs. $n=2050$), suggesting that neuronal cell class identity alone cannot explain all strong correlations. Therefore, I set out to characterize the connectivity features that are hallmarks of L-R pairs to investigate whether such features might predict strong functional interactions in general. L-R pairs are more likely to form a gap junction (43% compared to the rest of the network 1%, $p < 10^{-5}$ expected chance level) and as shown in the previous section, gap junctions were among the best direct connectivity features in predicting functional interaction (**Fig.4.7**).

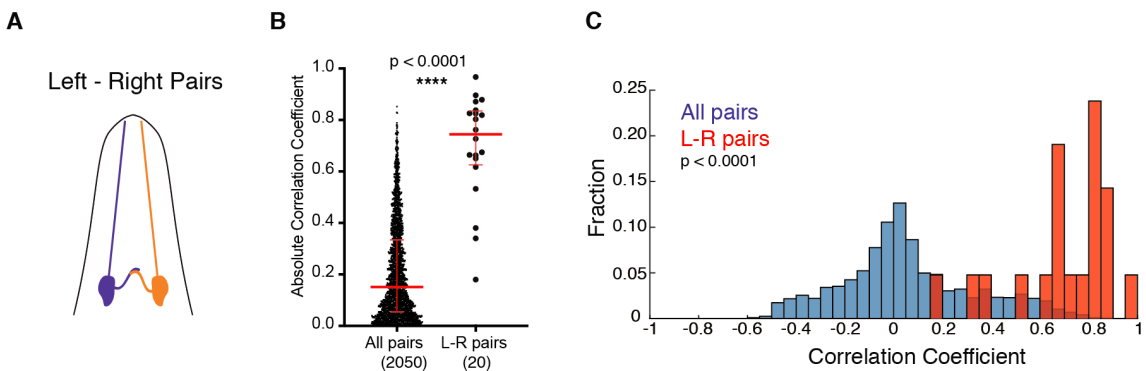


Figure 4.11 Pairs of the same class ID are amongst the most correlated neurons.

(A) Schematic showing left-right pair of the same neuron class.

(B) Pairwise correlations grouped by left-right pairs versus all remaining pairs in the network. Dots show correlations of individual neuronal pairs, red bars indicate median with interquartile range. Significance was tested with a custom shuffle test.

(C) Frequency distribution of correlation values for left-right pairs versus remaining pairs. Permutation p value estimate the probability that absolute distance between the mean of two distributions was obtained by chance. For all tests in this Figure: ****, $p < 0.0001$; ***, $p < 0.001$; ** $p < 0.01$. Numbers in parentheses indicate number of individual neuron pairs in scatter plots.

Besides by position and morphology, cell class identities were previously defined by sharing synaptic partners (Hobert et al., 2002; White et al., 1986), which can be quantified with primary (1°) input similarity, a measure which captures the fraction of shared inputs between neuronal pairs by calculating the similarity between the sets of presynaptic neurons (**Fig.4.12 A**). I found out that 1° input similarity is high among L-R pairs; however, all remaining pairs exhibited a skewed distribution (**Fig.4.12 B**) indicating that a subset of all pairwise neuronal combinations also shares similar input connectivities. Enrichment of input similarities in L-R pairs and the presence of a common input in the significant motifs both point to the influence of shared inputs as an important source of pairwise correlations. Consistent with this view, I found that 1° input similarity across all pairs was a better predictor of functional interaction in comparison to direct connectivity (**Fig.4.12 C** versus **Fig.4.8**). Next, I extended the input similarity analysis to the secondary (2°) input layer, which measures how similar the two larger network neighborhoods are upstream of each neuronal pair (**Fig.4.12 D**). Large fractions of both L-R pairs as well as all neuronal pairs exhibited high 2° input similarities (**Fig.4.12 E**). Importantly, a common 2° input does not necessarily require the presence of a 1° common input (**Fig.4.12 D**). Strikingly, I found out that 2° input similarity forms the best predictor of functional interaction in this study (**Fig.4.12 F**).

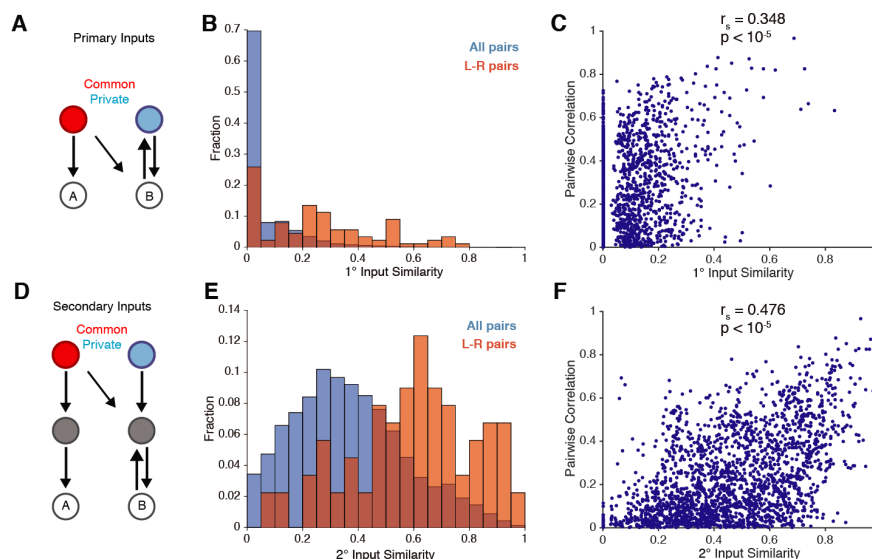


Figure 4.12 . Higher order connectivity measures and input similarities predict neuronal interactions.

(A,D) Diagrams depicting higher order connectivity features used for structure function predictions.

(B,E) Frequency histograms of connectivity exhibited by left-right and all pairs.

(C,F) Correlation analysis between pairwise correlations and indicated connectivity feature. r_s , Spearman's rank correlation coefficient. Permutation test p values indicate probability that r_s is found in degree preserved randomized networks.

(A-C) 1° input similarity (cosine distance between 1° input vectors). (D-F) 2° input similarity (cosine distance between 2° input vectors).

In order to find out whether input similarity measures selectively enrich neuron pairs with similar activity patterns, I repeated the analyses by restricting it to only one neuron and all its combinations within the datasets (e.g. AVAL vs all neurons). I found out that the predictability of 1° and 2° input similarities do not form high and low PC weight clusters (i.e the contribution of a neuron to the global population dynamics) but found distributed across a wide range (**Fig.4.13**).

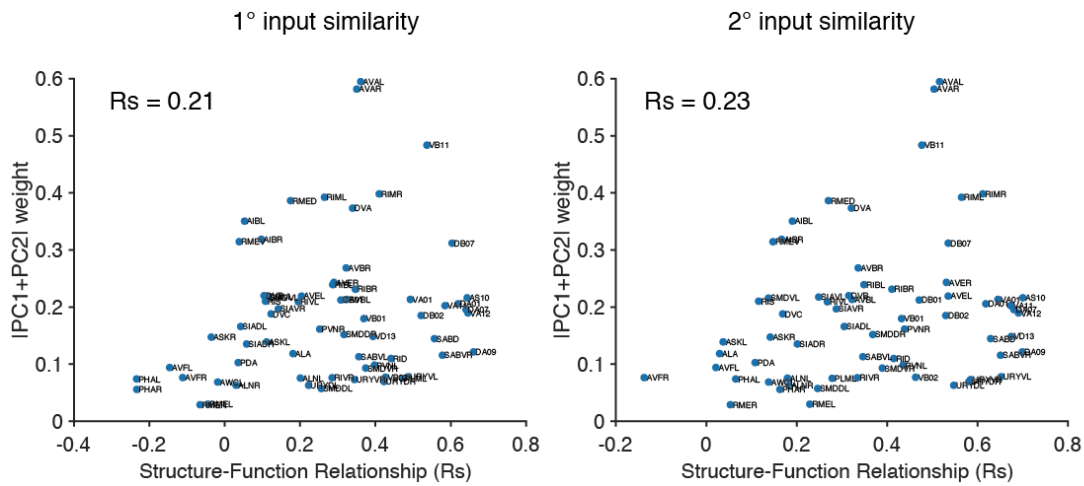


Figure 4.13 Structure-function relationships are comparable across different subsets of neurons.

Scatter dot plot of structure-function relationships calculated when using a single neuron and only it's corresponding pairs (e.g. AVAL means only AVAL and 65 more neurons -all it's combinations within **Fig.4.3.A**- are used to calculate that Rs value) versus that neurons summed absolute PC1 and PC2 weight. Neuron names are indicated by text. r_s , Spearman's rank correlation coefficient. Left: 1° input similarity is used as the anatomical measure. Right: 2° input similarity is used as the anatomical measure.

Moreover, this predictability was also at comparable levels when only the residual activity of neurons was used which lack the dominant first few PC modes (**Fig.4.14**) indicating that these results do not depend on the activity pattern which is captured by the first PC but valid for all the activity patterns captured in my recordings.

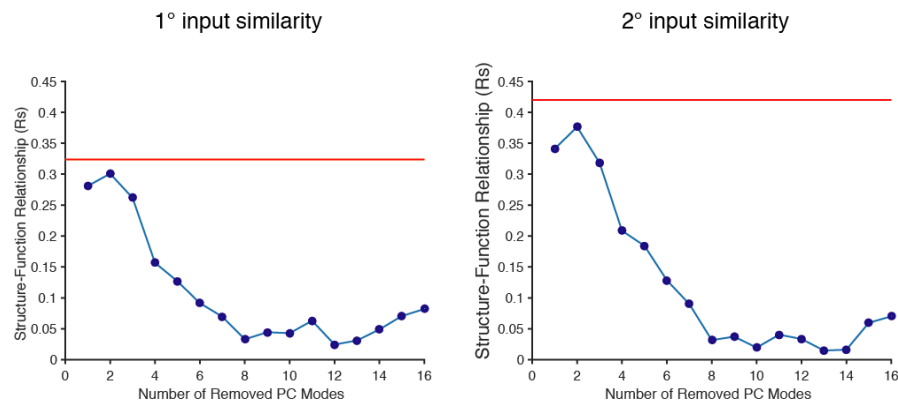


Figure 4.14 Prediction of input similarities does not depend on the first PC mode.

Structure-function relationship calculated from residual activity of neurons versus number of removed PC modes for residual activity calculation. Red lines indicate the Rs values in Fig.3C,F. Left: 1° input similarity is used as the anatomical measure. Right: 2° input similarity is used as the anatomical measure.

Finally, I set out to investigate input similarities across the connectome. When the connection matrix is transformed into pairwise 1° and 2° input similarity matrices it produced increasingly dense representations of connectivity (**Figs.4.15**). I also found a similar effect in random networks (**Fig. 4.16 C,D**). However, in the *C. elegans* connectome, both 1° and 2° input similarities are under-represented among sensory neurons (**Fig.4.16 A,B**) and over-represented not only among L-R pairs (**Fig.4.12 B,E**) but also among interneurons and most strongly among motoneurons (**Fig. 4.16 A,B**). All of these results suggest that both 1° and 2° input similarities might promote neuronal functions specific to neuronal cell types and might be evolved under selective pressure.

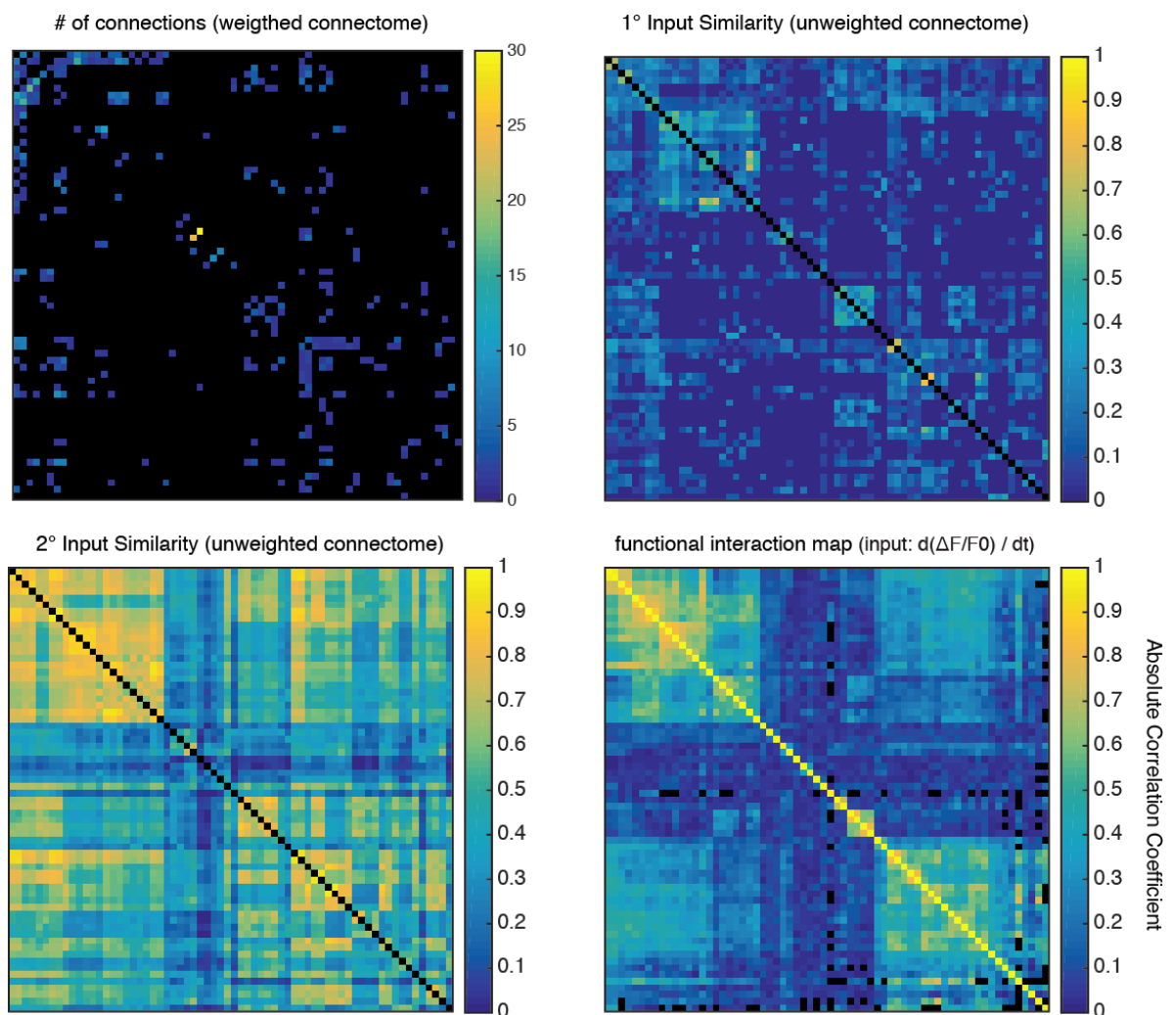


Figure 4.15 Input similarity matrices produced dense representations of connectivity.

Connectivity and correlation matrices. Top, left: Direct connectivity. Top, right: 1° input similarity. Bottom, left: 2° input similarity. Bottom, right: Absolute average correlation matrix. All Matrices have the same neuron order, and neurons are sorted like in **Fig.4.3 A**. Values indicated by color key.

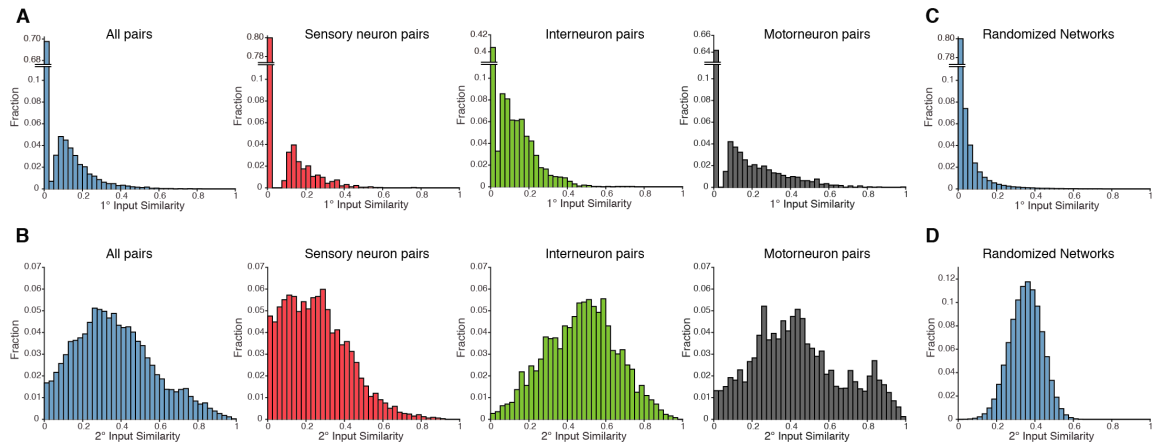


Figure 4.16 Exploration of input similarities across the connectome and random-networks.

(A-B) Frequency histograms for 1° and 2° input similarities (cosine distance) in the *C. elegans* connectome. First column: all pairs in the network, $n = 38781$. Second column: pairs between sensory neurons, $n = 3655$. Third column: pairs between interneurons, $n = 2556$. Fourth column: pairs between motorneurons, $n = 7021$.

(C-D) Frequency histograms for 1° and 2° input similarities of all pairs in randomized networks.

4.4. Systematic search for structure-function relationships

In the previous section, I found connectivity measures - generalized from L-R pairs- that can predict pairwise correlations in the connectome. Next, I extended this approach and systematically searched for structure-function relationships across a parameter space with the use of other measures both for pairwise activity relationships and for connectivity features. Apart from the correlation which was the main method of measuring functional interactions between neurons throughout this study, I also examined i) covariance to include information from signal amplitudes; ii) peak cross correlation to account for possible time lags between neurons, iii) mutual information to test the contribution of nonlinear interactions and iv) covariogram analysis to have an asymmetric measure of functional interactions which discretizes the data and is therefore insensitive to the shape of calcium signals (Brody, 1999; Kaplan et al., 2020). To capture interactions on fast and longer timescales I used either time-derivatives or original neuronal activity traces as inputs to these measures, respectively. Importantly, time-derivatives were previously shown to be more informative on decoding behavioural metrics (Kato et al., 2015). I examined features of connectivities that ranged from direct connectivity measures to higher-order connectivity patterns (sum of inverse shortest paths, 1° and 2° input similarities) with the combination of using weighted and unweighted matrices as inputs to these transformations (**Fig.4.17**). Recently, the *C. elegans* connectome was suggested to contain a significant portion of variable

connections (Witvliet et al., 2020). In order to account for this, I included additional control networks with partially randomized connections (see Methods).

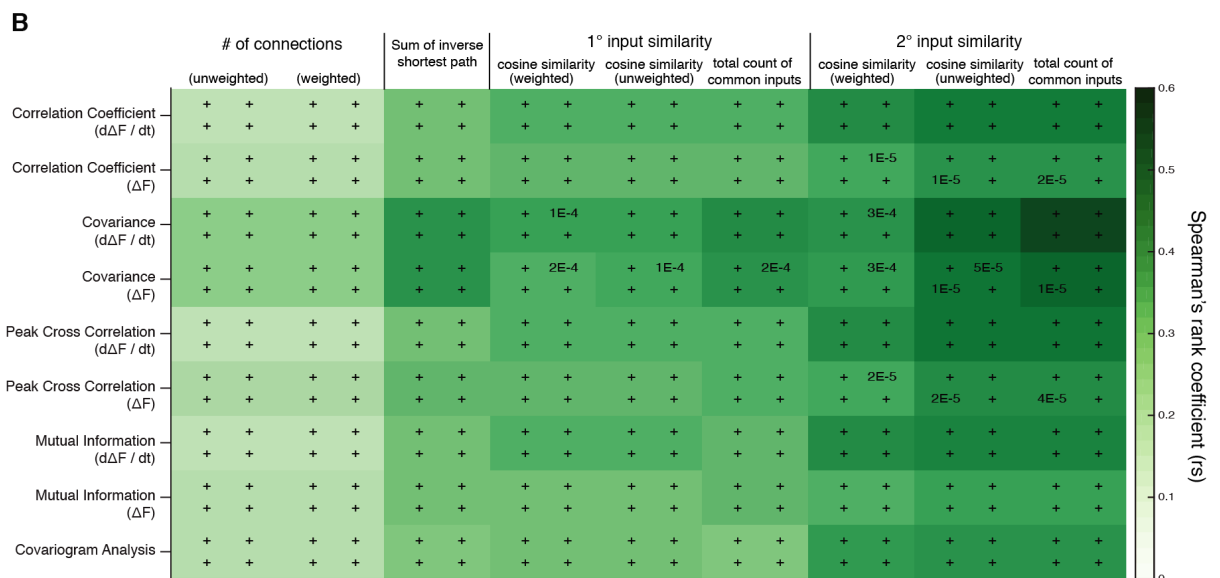
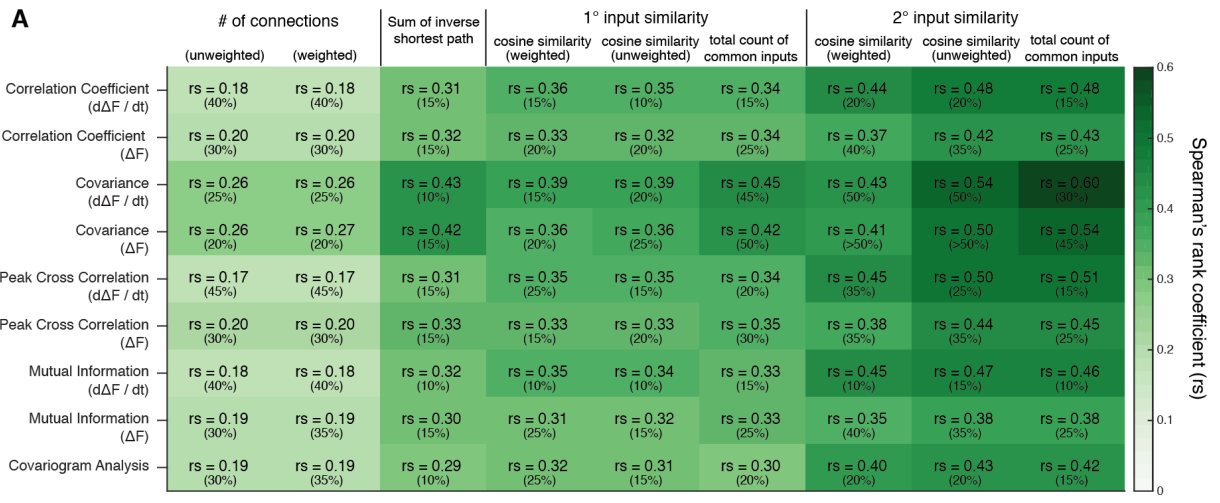


Figure 4.17 Systematic survey of structure-function relationships.

(A) Columns: connectivity metrics. Normalized and absolute means cosine distance and vector dot product of vector inputs, respectively. Rows: functional interaction metrics (ΔF, change in fluorescence; dΔF / dt; time derivative of change in fluorescence). r_s indicates Spearman's rank correlation coefficients also indicated by color key. Permutation test p values (Bonferroni adjusted) indicating probability that $\geq r_s$ value was found in degree preserved randomized networks. Raw p values for various random networks are shown in Fig.S4. Percentages indicate the maximum range of variability in the connectome that is tolerated to obtain a result not significantly different (see Methods).

(B) Columns: connectivity metrics. Rows functional interaction metrics (ΔF, change in fluorescence; dΔF / dt; time derivative of change in fluorescence). 4 entries in each cell show raw p values for permutation test indicating probability that $\geq r_s$ value in **panel A** of the corresponding cell was found in 4 different randomized networks. Top, left: totally randomized networks. Top, right: degree preserved randomized networks (also used in **panel A**). Bottom, left: degree, reciprocal connections and gap junction likelihood preserved randomized networks. Bottom, right: rich-club curve preserved networks. +, p < 10⁻⁵.

All of the structure-function analyses generated highly significant results which cannot be recapitulated in various versions of random-networks that preserve certain features of the connectome (**Fig.4.17**). Degree distribution is a key feature of the connectome that accounts for the resilience of the network, reciprocal connectivity ratio and gap junction likelihood of the connectome must be accounted while combining the gap junction and chemical synapse networks to test the effect of higher-order connectivity features in the combined network and preservation of rich-club organization ensures the high interconnectivity of the network hubs; thus, these different random networks which have various features serve as stringent controls (see Methods). Importantly, the results were highly robust to randomization carrying $\geq 10\%$, most of them even $\geq 20\%$ shuffled synapses (**Fig.4.17**). These two observations support the notion that the *C. elegans* connectome is a highly non-random network (Varshney et al., 2011), and show that my results are robust to annotation errors and possible inter-individual differences (Witvliet et al., 2020).

Across all measurements I did not find a pair of measures that particularly stands out in making the best structure-function prediction, but most informative and key to this study were the general trends I discovered: I found that neuron activity traces and their time-derivatives generated similar results, suggesting the predictive power of the connectome applies to both longer-term interactions and fast fluctuations. Non-linear methods yielded similar results to linear methods and importantly, covariogram analysis, the only approach that contain a directional interaction map, did not outperform. Furthermore, covariance generally outperformed correlation, suggesting that signal magnitudes are also important. On the structural side, using weighted or unweighted connectivity matrices generated similar results. Moreover, normalized input similarities (cosine similarity) yielded similar results compared to the total count of common inputs. These results were surprising and point out the importance of network topology and its sufficiency at making structure-function predictions. Quantities such as connection strength and gross amount of common input surprisingly do not add information to these predictions. Finally, higher-order connectivity measures generally outperformed lower-order or direct connectivity measures, indicating that indirect coupling via the network has a strong contribution to functional interactions.

4.5. *In silico* perturbations suggest determinant network hubs

In the previous sections I delineated structure-function relationships using the WT datasets and in the next sections I sought to experimentally test these by using genetic neuronal inhibition tools. First, I performed a systematic *in silico* perturbation screen in order to narrow down the best targets for this approach. I systematically removed 1 to 4 neuron classes from the network and then calculated the effects of these perturbations (see Methods for details). Importantly, these perturbations do not affect direct connectivity between the remaining pairs of neurons and therefore selectively target only higher order connectivity features. I observed that the removal of single or up to 4 classes of neurons, in the vast majority of instances, did not reveal any substantial effect on path-lengths, 1°- or 2° input similarity (Fig.4.18) which indicates robustness of network structure. However, upon removal of network hubs, the effects on network structure strikingly increased, particularly with the combinatorial removal of 4 hub classes (Fig.4.18).

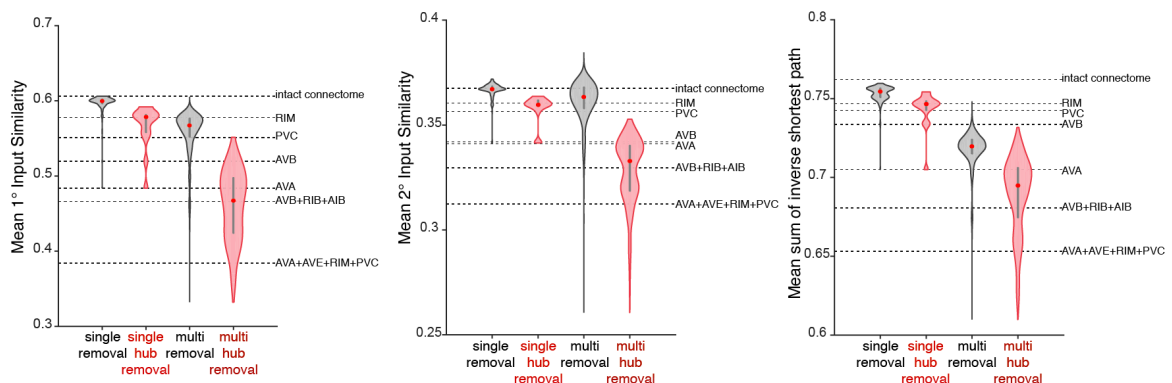


Figure 4.18 *In silico* perturbations reveal that network hubs are critical for the network.

Effect of *in silico* perturbations on mean 1° input similarity, 2° input similarity and sum of inverse shortest path. Violin plots indicate distributions of effects from all single neuron class removals ($n=187$); all hub class removals ($n=14$); random quadruple removals of any neuron classes ($n=6 \times 10^6$); and removals of all quadruple combination of hub classes ($n=1001$). Red dots indicate median, vertical grey lines within the violin plots indicate interquartile ranges. Vertical dashed lines show values for intact connectome and individual perturbations as indicated.

In these analyses hub neurons were identified by rich-club membership (Towlson et al., 2013) which is calculated from the combined network of chemical and gap junction connections (Fig.4.19).

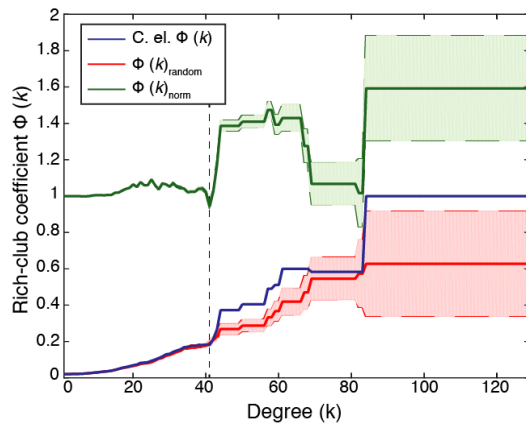


Figure 4.19 Rich club organization of the connectome using the combined network.

The blue line indicates the rich-club coefficient (RCC) of the *C. elegans* network (gap junctions + chemical synapses). Red line and shade indicate the mean RCC and standard deviation (SD) for 10^3 random graphs, respectively. The green line and shade indicate normalized RCC and SD, respectively. The vertical dashed line indicates the change point in the normalized RCC. Neurons above the threshold: AVAL/R, AVBL/R, PVCL/R, AVDL/R, DVA, AVEL/R, AIBL/R, RIAL/R, RIBL, HSNR, RIH, RIMR, AVJL, AVKL.

Next, I extended the perturbation screen to a larger set of connectivity measures (Rubinov and Sporns, 2010) (see Chapter 3.4) (**Fig.4.20**) and the effects of these perturbations were analyzed by PCA. PCA revealed that a large amount of variance of the effect on connectivity measures (67%) could be explained by the first PC, followed by only 10% and 7% contributed from PC2-3 (**Fig.4.20**).

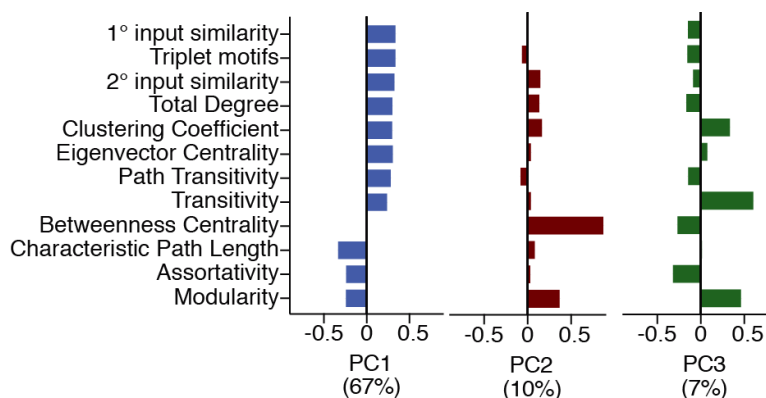


Figure 4.20 Many network features are interdependent.

PC weights of z-scored differences of 12 graph theoretical measures in perturbed networks vs. intact connectome. The variance explained by the PCs are indicated in the x axes.

Interestingly, PC1 exhibited a flat spectrum of eigenvalues (**Fig.4.20**) which suggests that connectivity features are all affected by neuronal perturbations to a similar extent and in a correlated fashion. In other words, it is not possible to selectively disrupt specific features such as path-lengths or input similarities in the network while leaving other features intact. Nevertheless, strong perturbations on network measures were largely due to the removal of multiple hub neurons (**Fig.4.21**) corroborating their key-role. Therefore, I investigated the contribution of hub neurons to the higher order connectivity motifs that were found to make strong structure-function predictions. Hub neurons constitute only 9% of the neurons within the connectome, but they form 56% and 55% of the gap junctions and chemical synapses, respectively. Importantly, I found that hub neurons were over-represented in significant triplet motifs (**Fig.4.22**). Furthermore, hub neurons were enriched sources of common 1°- or 2° input, and, as was previously shown (Towlson et al., 2013), contribute to short path lengths (**Fig.4.23**).

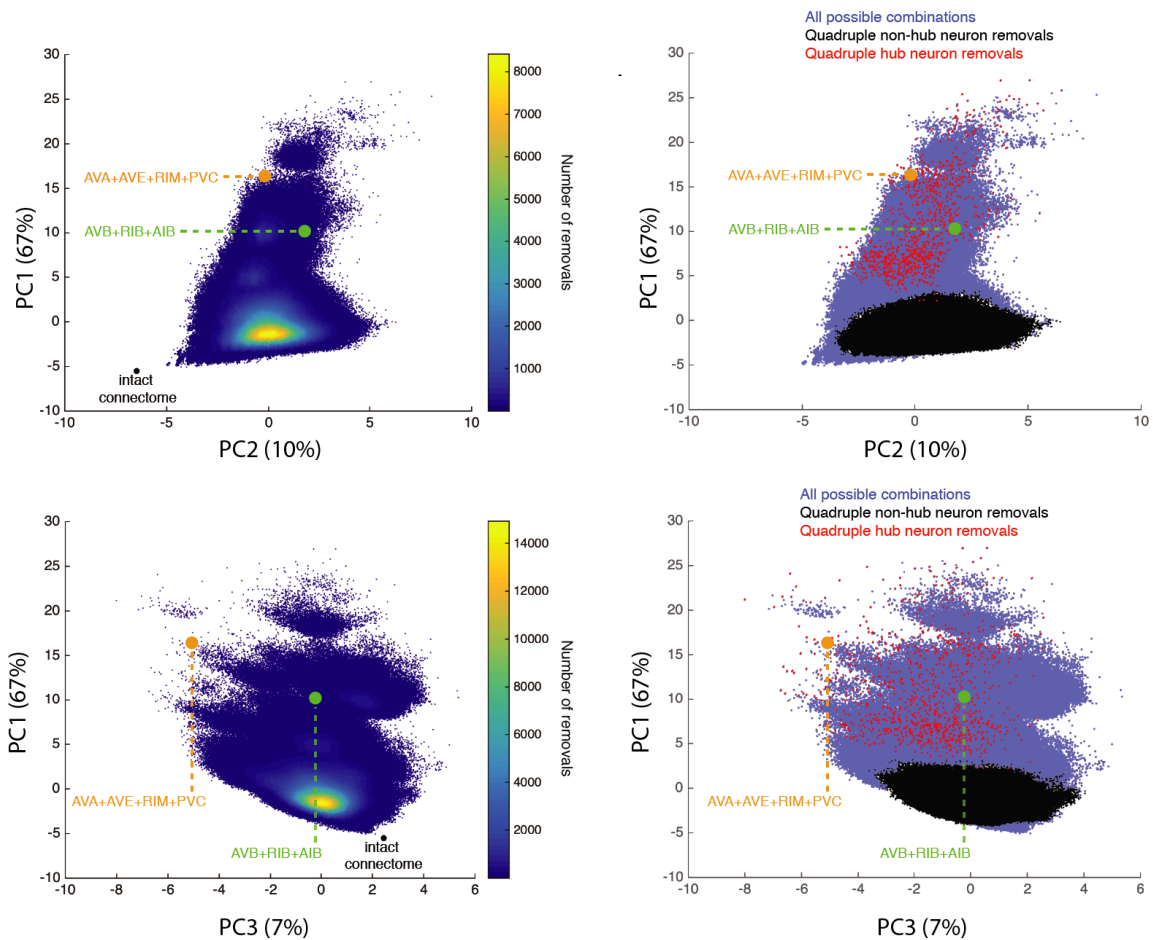
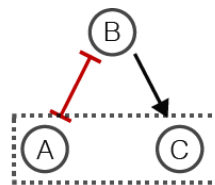


Figure 4.19 *In silico* perturbations suggest important network hubs that are critical for many network features.

Left: heat scatter plot of all *in silico* perturbations containing single, double, triple and quadruple neuron class removals in PC1 vs PC2 space (top) and in PC1 vs PC3 space (bottom). Black dots indicate the value of intact connectome. **Right:** Red dots indicate quadruple neuron class removals of rich-club neurons. Black dots indicate quadruple neuron class removals of non-rich club neurons. Green dot indicates AVB+RIB+AIB perturbation. Magenta dot indicates AVA+AVE+RIM+PVC perturbation.



Rich Club Ratio of B

Significant Motifs:	53% (p=0.058)
Insignificant Motifs:	31% (p=0.687)
All Motifs:	33%

Figure 4.20 Rich-club neurons are enriched in significant triplet motifs.

Top: An example triplet motif. Black arrow indicates chemical synapse (directed), red line indicates gap junctions (undirected).

Bottom: Quantification of the rich club ratio (RCR) for neuron B (third neuron) of corresponding motif groups. Permutation test p value estimates probability that RCR was obtained by chance in motif ID shuffled 10^5 trials.

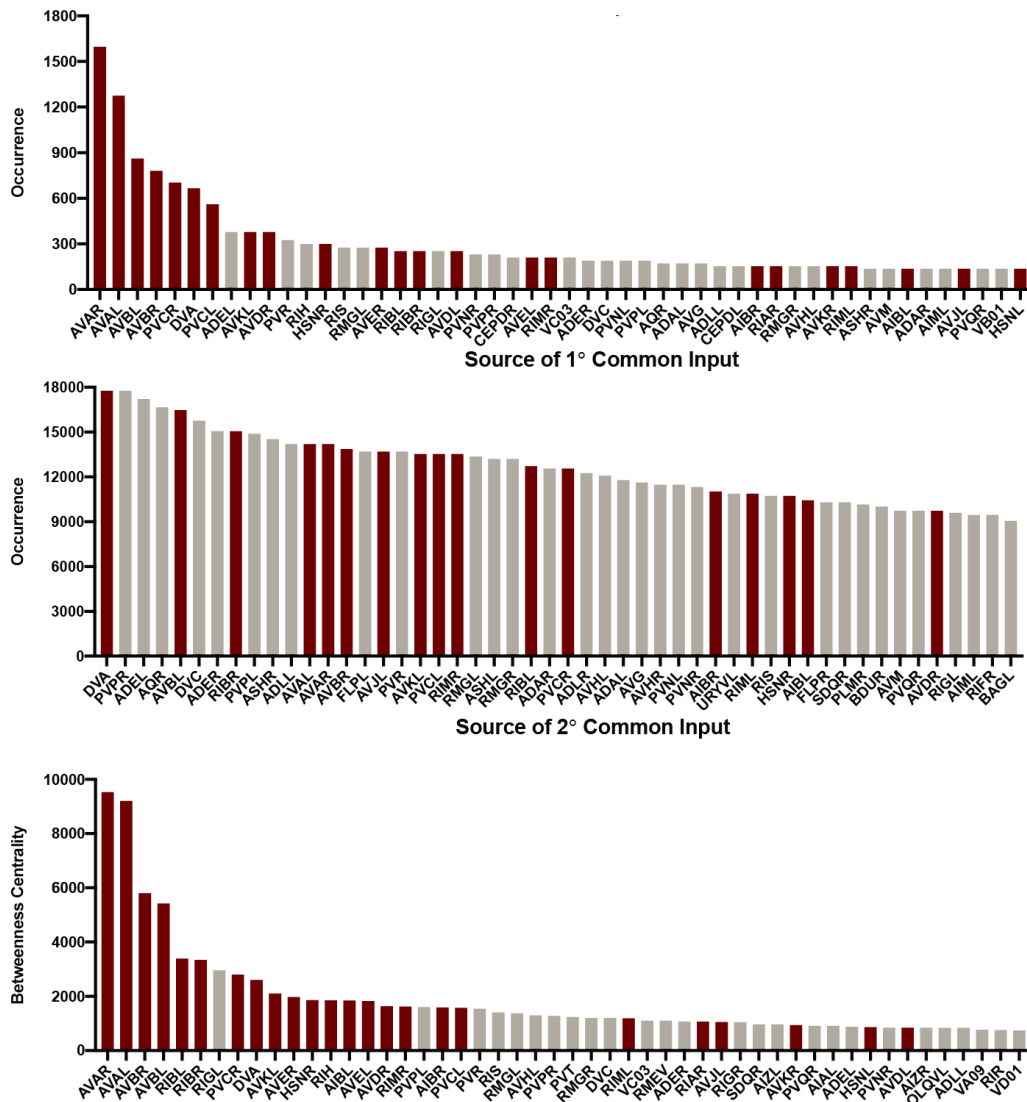


Figure 4.21 Network hubs are the top contributors of input similarities.

Top: Top 50 neurons' occurrences as the source neurons for 1° (top) and 2° (middle) input. Rich club neurons are indicated by red bars. **Bottom:** Betweenness centrality values for the top 50 neurons in the network. Rich club neurons are indicated by red bars.

It was previously shown that hub neurons interconnect the modular and segregated communities of the network (Pan et al., 2010; Sohn et al., 2011; Towson et al., 2013). To this end, I tested whether module membership (see Chapter 3.4.1) could make structure-function predictions and found out that pairwise correlations did not differ within versus across modules (Fig.4.24). This result is in parallel with the notion that correlated brain dynamics in my experimental conditions incorporate primary sensory interneurons, command interneurons and motor neurons (Kato et al., 2015) which should span all the modules found in refs. (Pan et al., 2010; Sohn et al., 2011). In conclusion, these analyses show that network hubs are crucial for the abundance of triplet motifs, higher order connectivity features as well as for the overall topology of the *C. elegans* connectome.

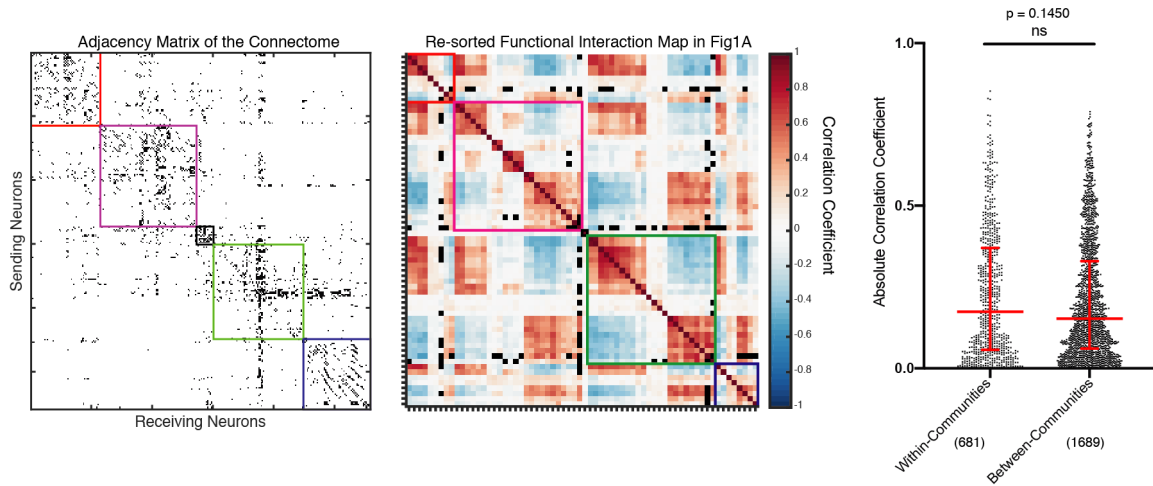


Figure 4.22 Community structure cannot predict correlations in the network.

Left: Unweighted connectivity matrix of the *C. elegans* connectome sorted by identified communities.

Middle: Pearson correlation matrix of identified neurons averaged across datasets re-sorted by identified communities in (Sohn et al., 2011) annotated by different colors ($n=6$ independent recordings of different worms). Correlation coefficients indicated by color key. Black boxes indicate pairs that are never observed simultaneously.

Right: Pairwise correlation grouped as within-communities and between-communities. L-R pairs are excluded from the analysis. Dots show correlations of individual neuronal pairs, red bars indicate median with interquartile range. Comparison was made with a custom shuffle test (Methods). ns, not significant. Numbers in parentheses indicate number of individual neuron pairs in scatter plots.

4.6. Disrupting network hubs decreases global correlations

The results from the previous sections showed that individual connectivity features included in my analyses are largely interdependent and thus cannot be manipulated in a selective manner. On the other hand, the same results led to a prediction: I showed previously that hub architecture of the neuronal network supports many of connectivity features that make significant structure-function predictions. Therefore, the hub architecture is likely to be required for globally synchronized neuronal dynamics. To test this prediction, I sought to inhibit multiple hub neurons experimentally using histamine gated chloride (HisCl) channels suitable for selective and transient inhibition (Pokala et al., 2014) (see Chapter 3.7).

After surveying available genetic driver combinations, I decided on two non-overlapping sets of hub neurons to target that have different organizational features. First combination contains AVA-AVE-RIM-PVC neurons. Here, three neurons are active during backward movement motor commands (AVA, AVE, RIM) and one neuron is the command interneuron of the forward movement circuit (PVC) (Chalfie et al., 1985; Gordus et al., 2015; Gray et al., 2005; Kato et al., 2015; Li et al., 2014) (see Chapter 3.7). Second

combination encompasses AVB-RIB-AIB neurons involved in forward movement motor command (AVB), forward movement and forward-to-turn transition (RIB) and backward movement and backward-to-turn transition (AIB) (Chalfie et al., 1985; Gordus et al., 2015; Gray et al., 2005; Kato et al., 2015; Li et al., 2014) (see Chapter 3.7). These two combinations all contain network hubs and mainly target one of the two main modules within the network: backward and forward movement circuit, respectively. Importantly, *in silico* removal of both combinations exhibited drastic decrease of higher-order similarity measures and short path-lengths in the network in my systematic perturbation screen (Fig.4.18). Furthermore, these two combinations generated high values when projected onto PC1 which pools the effect on many measures (Fig.4.21) providing a severe perturbation on various network measures.

First, I observed that upon histamine application targeted neurons in both lines were inhibited effectively (Fig.4.25). Moreover, animals showed expected selective effects in behavioural experiment assays: AVA-AVE-RIM-PVC inhibition led to a complete abolishment of backward movement in worms while speed of AVB-RIB-AIB inhibited worms drastically decreased (Fig.4.26).

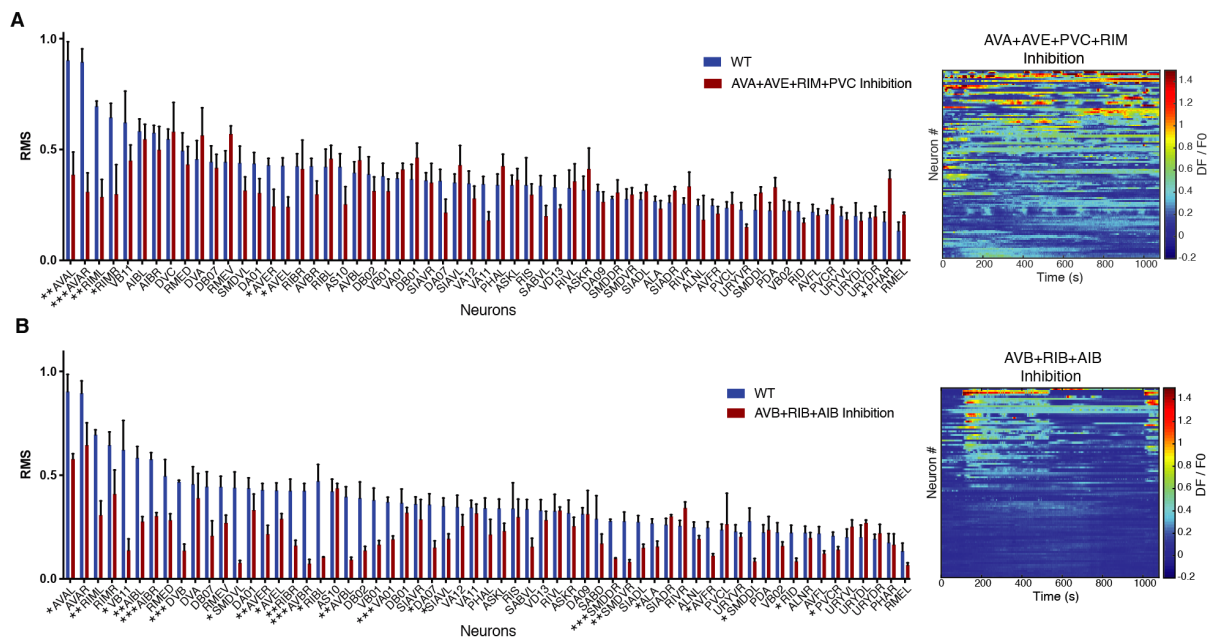


Figure 4.23 Neuronal activity levels of the multiple hub inhibition lines.

(A-B) **Left:** Neuronal activity levels (RMS) of identified neurons in WT vs. inhibition datasets. Neurons are sorted by WT values in descending order. Error bars indicate SEM. Comparisons were made by t-test. * $p < 0.05$, ** $p < 0.01$, *** $p < 0.001$. **Right:** Representative examples of 18-min-long whole-brain imaging recordings from indicated inhibition lines, shown as heat maps of fluorescence (DF/F₀) time series of all detected neurons (one neuron per row, sorted by neuronal activity levels).

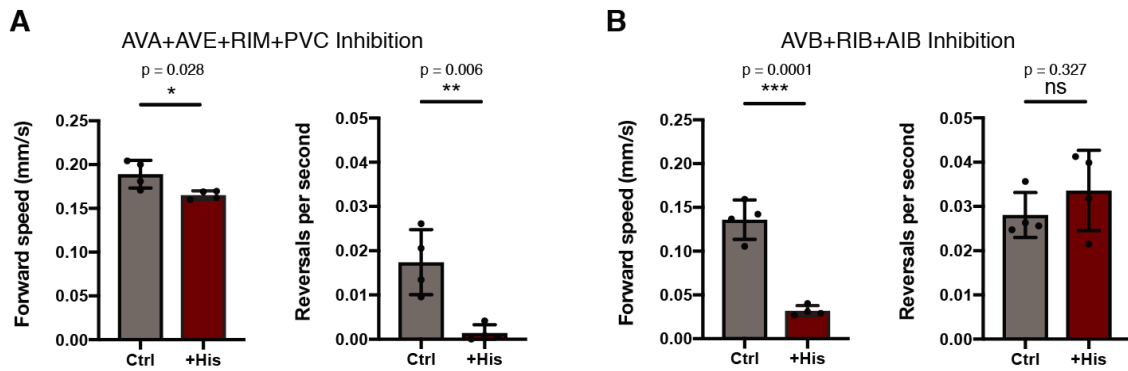


Figure 4.24 Behavioural analysis of the multiple hub inhibition lines.

(A-B) Quantification of population behavioural assays of the indicated inhibition line without (Ctrl) or with (+His) histamine treatment. Left: forward speed. Right: reversal events per second. Each data point represents a single assay, $n = 20-25$ worms per assay. Horizontal lines and error bars show mean and SD, respectively. Asterisks indicate significance levels after Mann-Whitney test.

These results were consistent with the targeting of backward or forward movement circuit and roles of the targeted neurons in these circuits. However, the results of the behaviour experiments might have two different origins. First, the command interneurons AVA and AVB which form a bottleneck between the head ganglia and the body motor neurons were inhibited in two different combinations; thus, the backward or the forward motor command could not be relayed to the motor neurons. In other words, the backward or forward motor command could be generated in the nervous system but because of the inability to relay it to the motor neurons it could not be executed (Chalfie et al., 1985; Kawano et al., 2011; Wen et al., 2012). On the other hand, the backward or forward movement circuit might have been severely perturbed via the disruption of network hubs; thus, the backward or forward network activity could not be properly established due to the inability of recruitment of neurons or the maintenance of coordination between them.

In order to reveal the origin of this effect, I performed whole-brain imaging experiments with these inhibition lines. In nervous system wide imaging experiments, I observed a drastic decrease in the global pairwise correlations in both multiple hub inhibition lines (**Fig.4.27 A,B**) confirming that the results of behavioural experiments were not only an execution defect but a reflection of a severe loss of coordination within the network dynamics. These results were in parallel with the results of the *in silico* perturbation screen where I observed a severe perturbation effect (reflected as high values on PC1) in both combinations (**Fig.4.21**). Next, I checked the global neuronal activity levels of the multi-hub inhibition lines to further understand the reason of the loss of global

hub combinations and performed the same experiments and analyses. In all single cell inhibition lines, I observed the expected selective effects in behavioural experiment assays (**Fig.4.28 A-G**). Moreover, all of the targeted neurons were inhibited effectively (**Fig.4.29** and **Fig.4.30**). The only neuron class that did not exhibit calcium transients in my unstimulated experimental setup was PVC which was consistent with the previous studies (Li et al., 2011). Therefore, I performed an additional type of behaviour assay with the PVC inhibition line and indirectly confirmed the inhibitory effect of HisCl in these neurons with the loss of posterior touch responses (**Fig.4.28 H**).

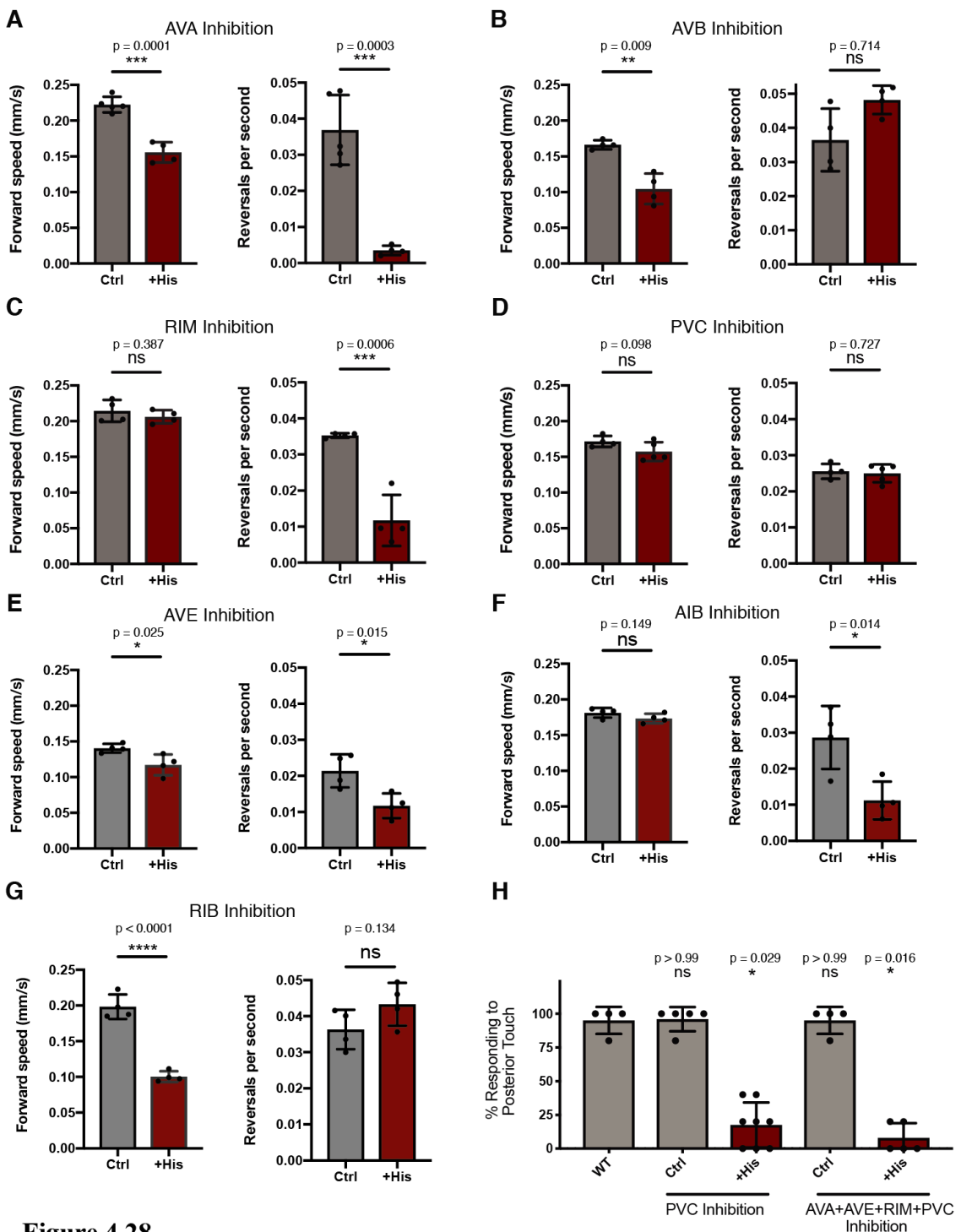


Figure 4.28

Figure 4.26 Behavioural analysis of the single hub inhibition lines.

(A-G) Quantification of population behavioural assays of the indicated inhibition line without (Ctrl) or with (+His) histamine treatment. Left: forward speed. Right: reversal events per second. Each data point represents a single assay, $n = 20\text{--}25$ worms per assay. Horizontal lines and error bars show mean and SD, respectively. Asterisks indicate significance levels after Mann-Whitney test.

(H) Response of WT worms and indicated inhibition lines without (Ctrl) and with (+His) histamine treatment in posterior harsh touch assays. Each data point represents a single assay, $n = 5$ worms per assay. Horizontal lines and error bars show mean and SD, respectively. Asterisks indicate significance levels after Kruskal-Wallis test with Dunn's multiple-comparisons test. For all tests in this Figure: ****, $p < 0.0001$; ***, $p < 0.001$; **, $p < 0.01$, ns, not significant.

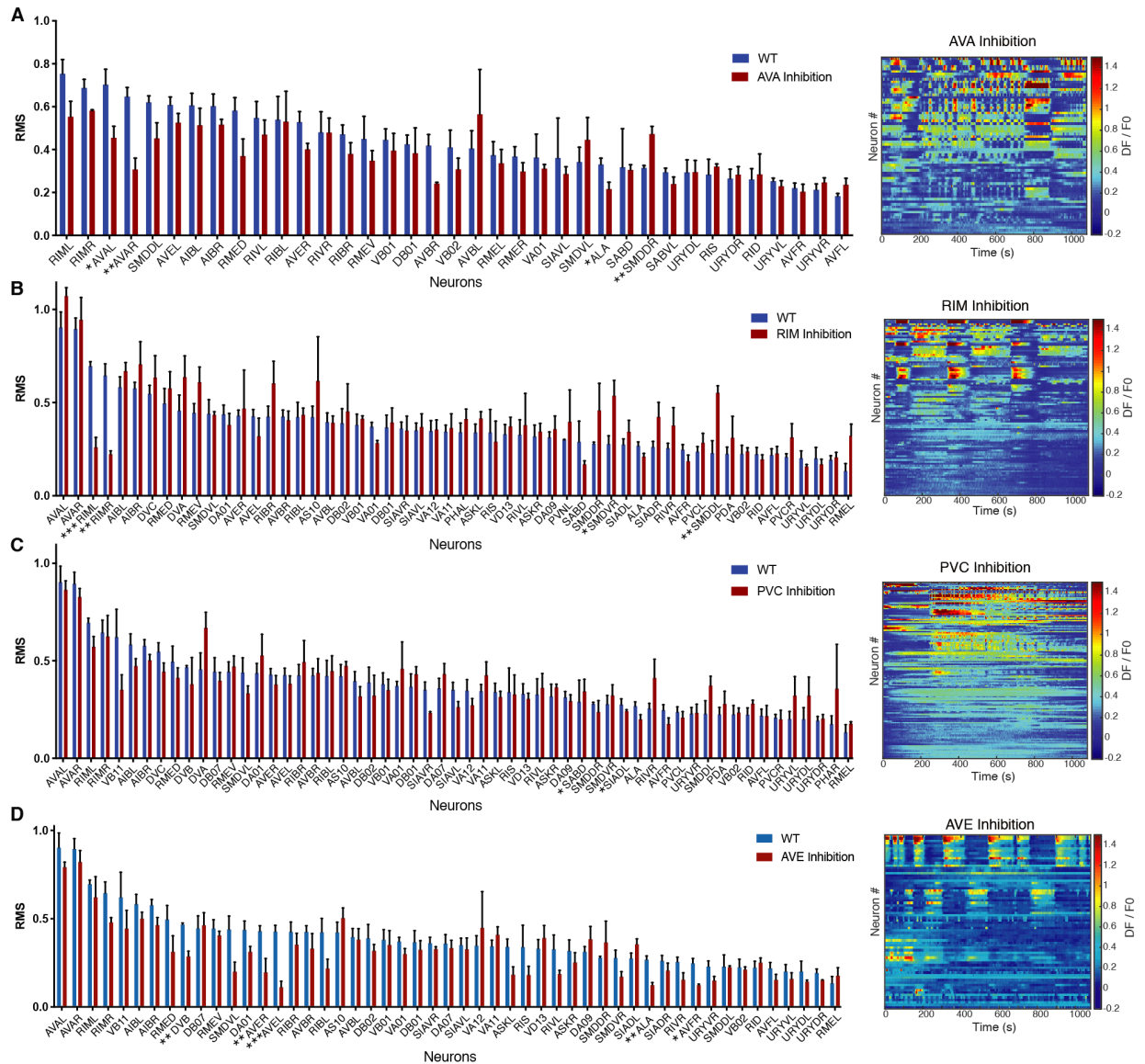


Figure 4.29 Neuronal activity levels of single hub inhibition lines within the AVA-AVE-RIM-PVC combination.

(A-D) Left: Neuronal activity levels (RMS) of identified neurons in WT vs. inhibition datasets. Neurons are sorted by WT values in descending order. Error bars indicate SEM. Comparisons were made by t-test. * $p < 0.05$, ** $p < 0.01$, *** $p < 0.001$. Right: Representative examples of 18-min-long whole-brain imaging recordings from indicated inhibition lines, shown as heat maps of fluorescence (DF/F₀) time series of all detected neurons (one neuron per row, sorted by neuronal activity levels).

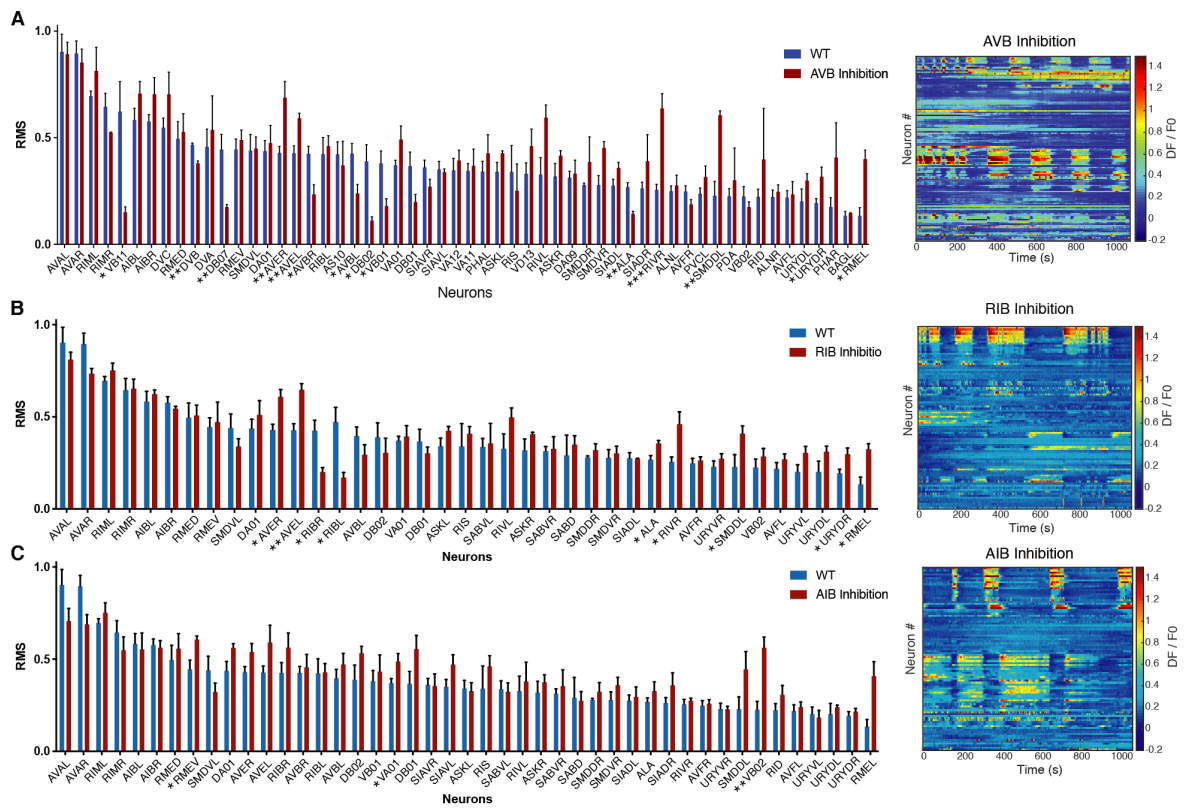


Figure 4.27 Neuronal activity levels of single hub inhibition lines within the AVB-RIB-AIB combination.

(A-C) Left: Neuronal activity levels (RMS) of identified neurons in WT vs. inhibition datasets. Neurons are sorted by WT values in descending order. Error bars indicate SEM. Comparisons were made by t-test. * $p < 0.05$, ** $p < 0.01$, *** $p < 0.001$. Right: Representative examples of 18-min-long whole-brain imaging recordings from indicated inhibition lines, shown as heat maps of fluorescence (DF/F_0) time series of all detected neurons (one neuron per row, sorted by neuronal activity levels).

In nervous system wide imaging experiments, single-hub-neuron targeted animals exhibited normal global pair-wise correlations, not significantly different from WT animals (Fig.4.31 A-D and Fig.4.32 A-C). Importantly, global neuronal activity levels were not significantly affected in all single hub neuron inhibition lines (Fig.4.31 E-H and Fig.4.32 D-F). These results demonstrated that brain dynamics can only be globally disrupted with multiple hub neuron perturbations, as opposed to single cell manipulations where I observed the effect of perturbation confined on the correlation matrices and localized to a single cluster (Fig.4.31 A-D and Fig.4.32 A-C, quantified in Fig.4.31 E-H, Fig.4.32 D-F and Fig.4.33), suggesting that hub architecture supports the synchronization of global network dynamics. Moreover, the retainment of uncoordinated activity fluctuations in both multi-hub targeted animals precludes the possibility that I targeted specific drivers or pace-makers of the network and suggests that the detrimental effect on pairwise correlations was rather due to the loss of indirect couplings via the network.

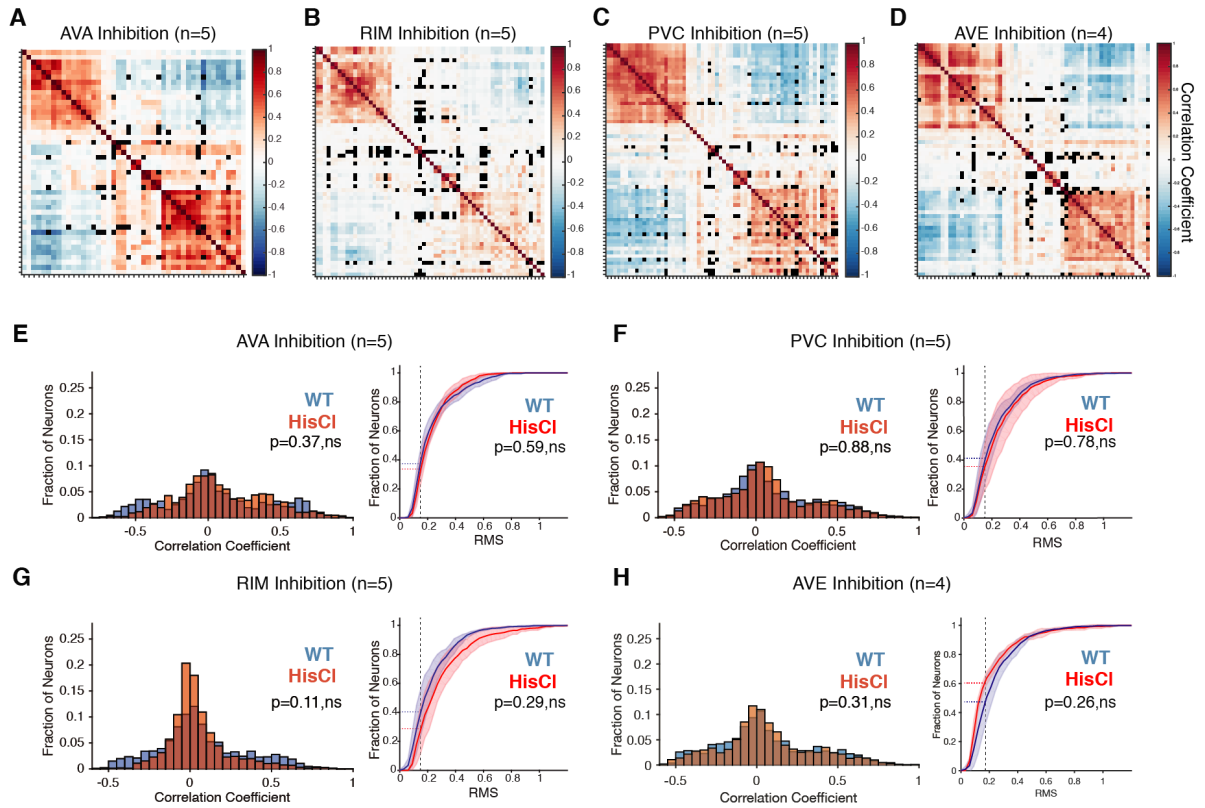


Figure 4.28 Global neuronal population dynamics are robust to single hub control perturbations within AVA-AVE-RIM-PVC combination.

(A-D) Average correlation matrices from single hub inhibition control lines, n=5 independent recordings for each line except AVE inhibition line (n=4). Correlation coefficients indicated by color key. Neurons are sorted like in Fig.4.3 A. See also Fig.4.3 A.

(E-H) Left panels: Frequency distribution of average pairwise correlations for WT and indicated inhibition lines. Permutation test p values estimate the probability that KS distance between two distributions was obtained by chance. Right panels: Cumulative frequency distributions of neuronal activity levels (RMS) for WT and indicated inhibition lines. Permutation p values estimate the probability that KS distance between two distributions was obtained by chance. n, numbers of independent recordings from different worms. Vertical dashed lines indicate the average RMS value of all inhibited neurons in this study providing a guideline for non-active neurons.

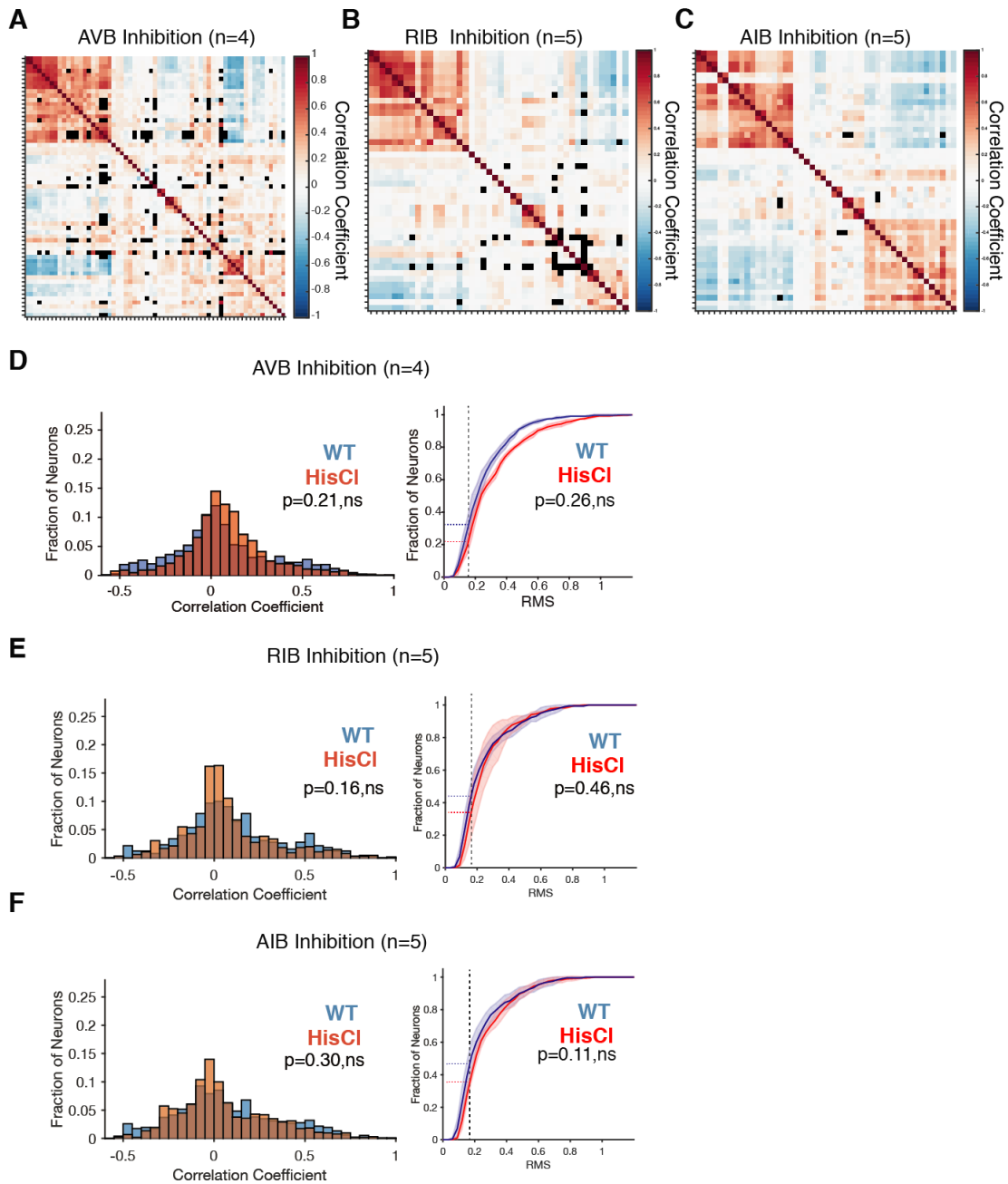


Figure 4.29 Global neuronal population dynamics are robust to single hub control perturbations within AVB-RIB-AIB combination.

(A-C) Average correlation matrices from single hub inhibition control lines, n=5 independent recordings for each line except AVB inhibition line(n=4). Correlation coefficients indicated by color key. Neurons are sorted like in Fig.4.3 A. See also Fig.4.3 A.

(D-F) Left panels: Frequency distribution of average pairwise correlations for WT and indicated inhibition lines. Permutation test p values estimate the probability that KS distance between two distributions was obtained by chance. Right panels: Cumulative frequency distributions of neuronal activity levels (RMS) for WT and indicated inhibition lines. Permutation p values estimate the probability that KS distance between two distributions was obtained by chance. n, numbers of independent recordings from different worms. Vertical dashed lines indicate the average RMS value of all inhibited neurons in this study providing a guideline for non-active neurons.

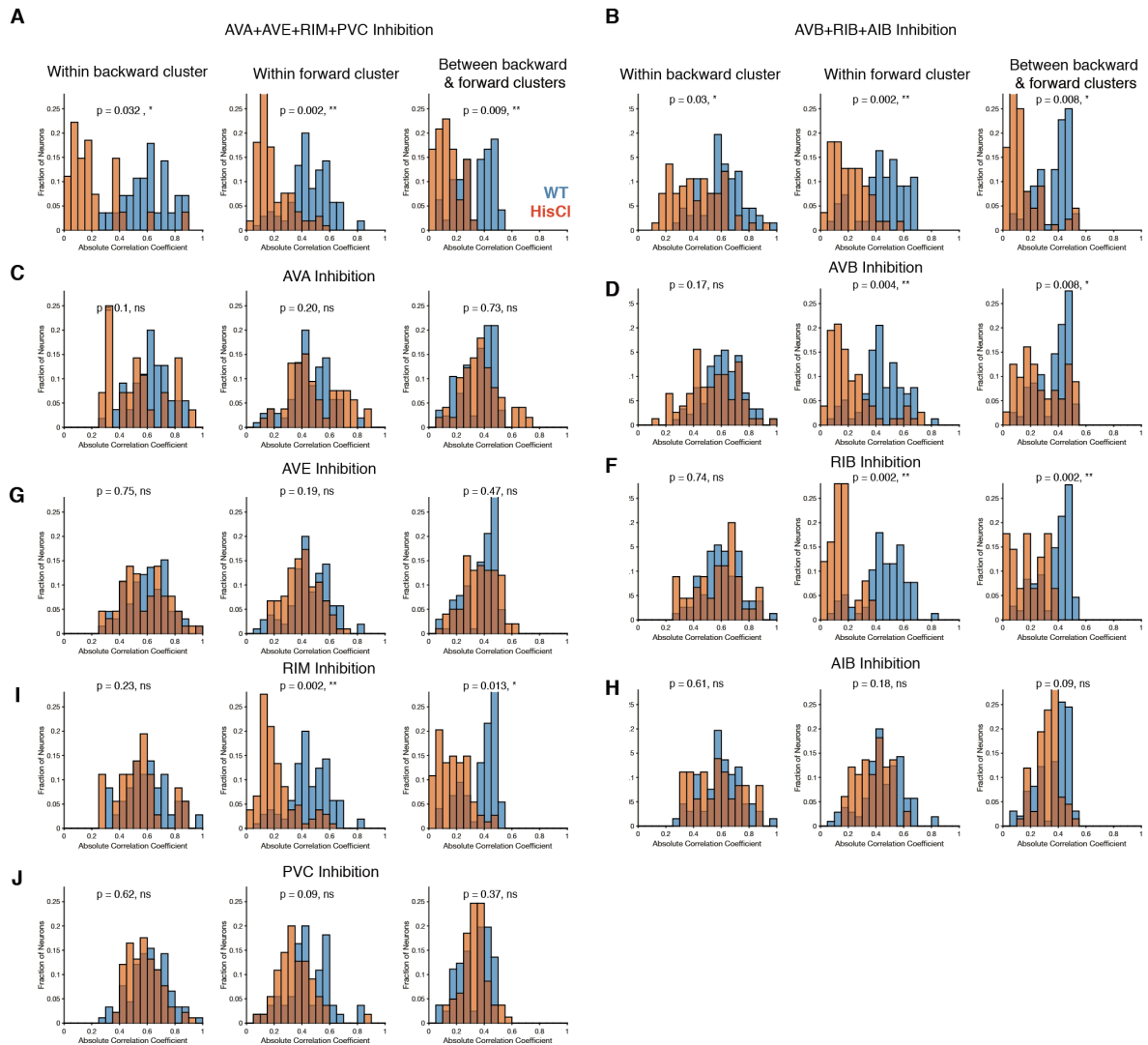


Figure 4.30 Differential effects of the inhibition lines on backward and forward clusters.

(A-J) Frequency distribution of average pairwise correlations for WT and indicated inhibition lines. **Left**, correlations within backward cluster; **middle**, correlations within forward cluster; **right**, correlations between the clusters (for cluster identification, see Methods). Permutation test p values estimate the probability that KS distance between two distributions was obtained by chance.

Finally, in single hub inhibition experiments, I observed an interesting specific effect in the RIM-only targeted animals where two other hub neurons AVA and AVE but not AIB neurons occasionally became de-coupled from network dynamics. In WT animals the reversal interneurons AIB, RIM, AVA and AVE are always active in synchrony and antagonistically to the forward interneurons (Kato et al., 2015) (see Chapter 3.7). However, in RIM-inhibited animals I observed that only AIB became active in nearly half of all switches from the forward state (**Fig.4.34 A-C**). This is consistent with a di-synaptic pathway from AIB to AVA/AVE via RIM neurons (Gordus et al., 2015) (**Fig.4.34 D**), and suggests that RIM establishes coupling between AIB and the other interneurons within the backward movement circuit. Another observation about single

cell inhibition experiments were about the comparison of secondary layer interneurons and command interneurons.

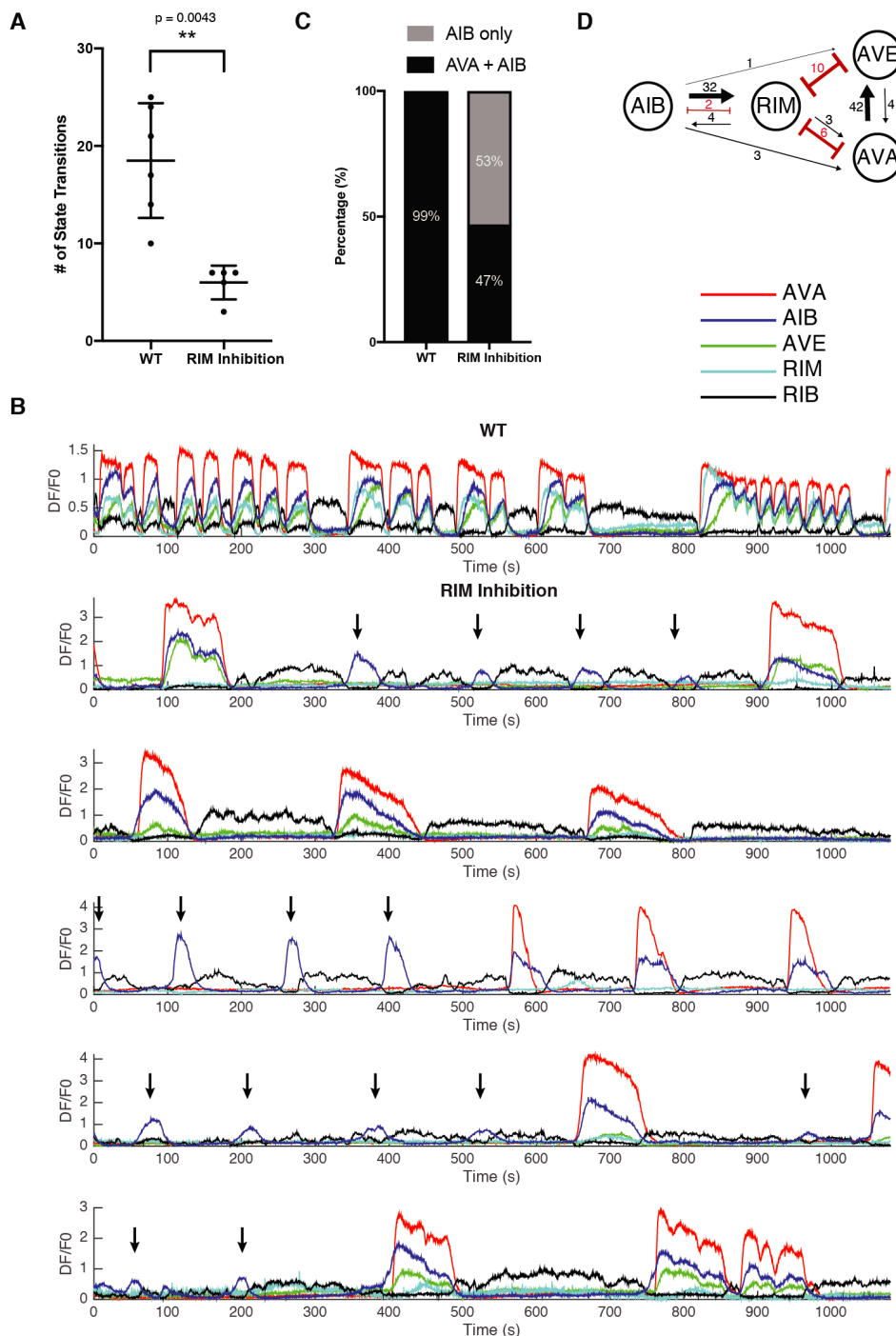


Figure 4.31 Effect of RIM inhibition on the backward-movement interneurons.

(A) Number of state transitions in whole-brain recordings of WT and RIM-inhibition line (n=6 and n=5, respectively). Dots show individual recordings, black lines indicate means and error bars indicate SD. Asterisks indicate significance level after Mann-Whitney test. ** $p < 0.01$.

(B) Traces of reversal neurons and RIB (representing the forward neurons). Neuron names are indicated in the legend. Top: a representative WT recording. Bottom: 5 different recordings from different worms of RIM-inhibition line. Black arrows indicate events where AIB is active but the rest of the reversals neurons are not active.

(legend continued on next page)

(C) Colored bar plot of different percentages of reversal states. Black indicates reversals where AVA and AIB neurons are both active. Grey indicates brain states where AVA and rest of the reversal neurons are not active but AIB is active.

(D) Neuronal circuit of AIB-RIM-AVA-AVE neuron classes. Black arrow indicates chemical synapse (directed), red line indicates gap junctions (undirected). The width of the lines indicates strength of the connection: the number of synapses / gap junctions are indicated next to the connection.

Interestingly, although both are non-significant globally, the effects of second-layer interneurons (RIM and RIB) were comparable (or even stronger in some cases) than the effects of high degree pre-motor interneurons (AVA, AVE, PVC, AVB) (**Fig.4. 31**) which have more synaptic partners and connections in the connectome, indicating that the removal of key connections has a more substantial effect on synchronizations than the removal many connections.

4.7. Disrupting connectivity features decreases pairwise neuronal correlations

If the contribution of hub neurons to connectivity features identified in the previous sections of study is indeed crucial for establishing globally synchronized brain dynamics, the effect of hub neuron perturbations on connectivity measures is expected to correlate with the effect on functional interactions. I first tested this prediction with respect to significant motifs. I classified the neuron pairs in the inhibition lines which are members of significant motifs into two groups: the ones where the third neuron in the triplet motif is targeted and the ones where the third neuron is unaffected (**Fig.4.35 A**). I observed that the members of intact significant motifs exhibit higher correlation values compared to the control pairs (neuron pairs that are not a member of any motif, see Methods) and strikingly, this enrichment was lost in the disrupted motifs (**Fig.4.35 B,D**). This result was observed in both inhibition lines where different sets of motifs are targeted (**Fig.4.35 B,D**) supporting that the effect does not depend on the targeted neurons but rather on the underlying triplet motifs. Critically, intact motifs within the inhibition lines exhibited significantly lower pairwise correlations compared to their WT counterparts (**Fig.4.35 C,E**). In summary, partial retainment of correlations within intact motifs of hub inhibition datasets where global population dynamics is absent or largely disrupted indicate that connectivity triplet motifs are -although partial- responsible for the pairwise correlations and their disruption cannot entirely account for the decline in global network synchronies upon hub-neuron inhibition. As expected, other higher order connectivity features -also delineated in the previous sections- must have a contribution.

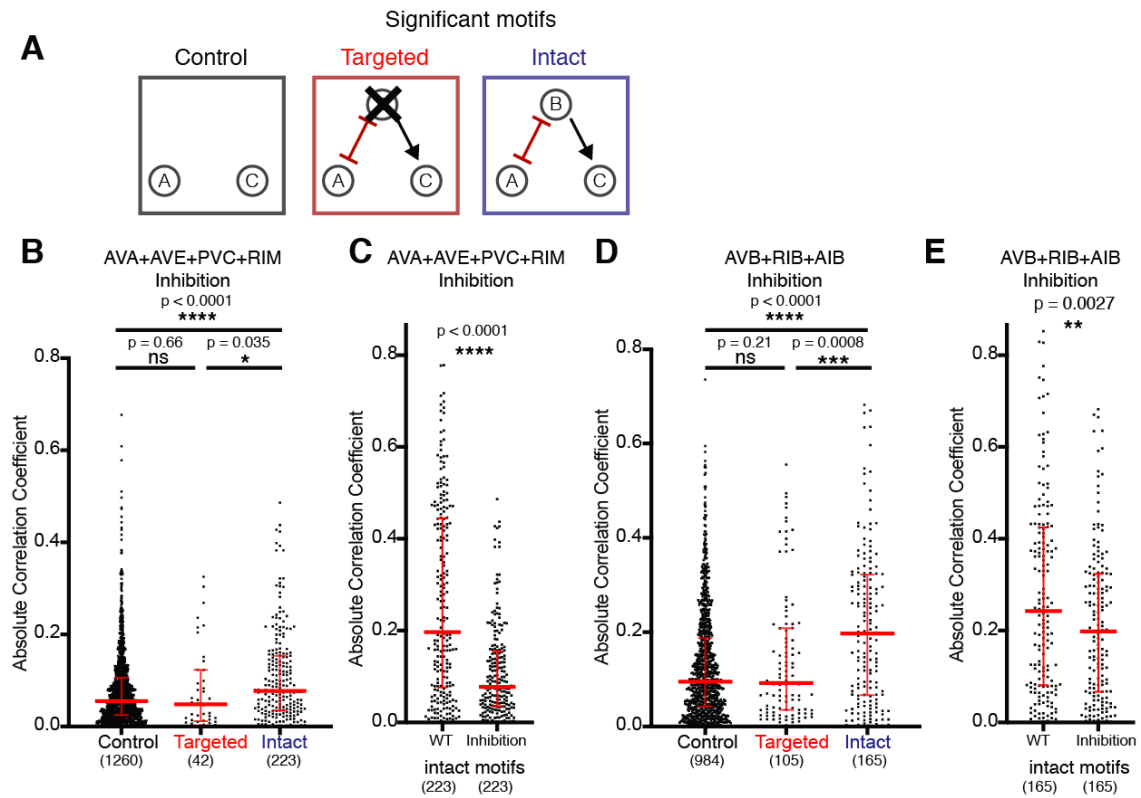


Figure 4.32 Significant triplet motifs partially explain the decrease in global correlation levels.

(A) Schematic illustrating comparisons made in panels below using a single example motif. Black box: control group with the neuron pairs that do not belong to any triplet motif; red box: neuron pairs that belong to significant motifs and the third neuron (depicted with B) targeted in inhibition line; or blue box: left intact.

(B,D) Pairwise correlations grouped by control, targeted motifs and intact motifs. Dots show correlations of individual neuronal pairs, red bars indicate median with interquartile range. Significance was tested with a custom shuffle test.

(C,E) Pairwise correlations of intact motifs in WT vs. inhibition lines. Dots show correlations of individual neuronal pairs, red bars indicate median with interquartile range. Significance was tested with a custom shuffle test. Numbers in parentheses indicate number of individual neuron pairs in scatter plots.

Therefore, I analyzed to what extent the reduction of path lengths and input similarities in the perturbation lines can explain the global decrease in functional interactions. First, I calculated how strong path lengths, 1° and 2° input similarities were changed in both perturbation lines compared to WT and classified neuron pairs into two groups: perturbed versus unaffected (**Fig.4.36 A-C**). I found that neuronal pairs perturbed in these measures exhibited decreased pairwise correlations, while unaffected pairs retained WT correlation values (**Fig.4.37**). Although 2° input similarity is a better predictor, the perturbation of both input similarity measures showed a similar effect on correlations. Importantly, a significant decrease is observed in both metrics indicating that the predictive power of 1° and 2° input similarities is retained in datasets with disrupted global patterned activity which further supports their role in structure-function relationships within the nervous system. In order to test whether these results were robust

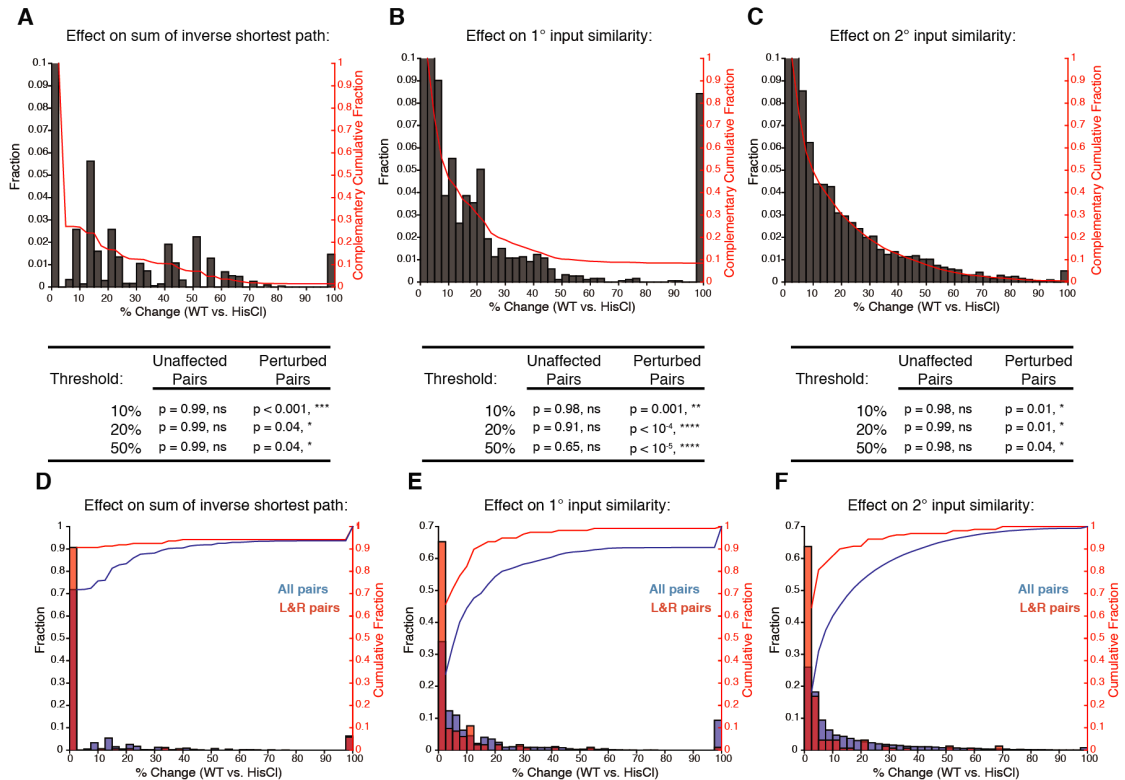


Figure 4.33 Different pairs are selectively perturbed in the network in inhibition lines.

(A-C) Top: frequency histograms of the percent change (WT vs. inhibition line) for indicated connectivity measure. Red lines indicate complementary cumulative distribution. Bottom: Permutation p values estimate the probability that KS distance between two distributions in Fig.4.35 was obtained in degree preserved randomized networks for indicated cutoff defining perturbed vs control pairs. (A) Sum of inverse shortest paths. (B) 1° input similarity (C) 2° input similarity.

(D-F) Frequency histograms of the percent change (WT vs inhibition line) for connectivity exhibited by left-right and all pairs. Red lines indicate cumulative distribution. (D) Sum of inverse shortest paths. (E) 1° input similarity (F) 2° input similarity.

to the arbitrary cutoff I had to make in order to classify perturbed versus unperturbed pairs, I repeated the analysis with different cutoffs and all of them yielded similar results (Fig.4.36 A-C). Since genetic drivers cover typically both the left and the right member of each cell-class, my experimental perturbations were symmetric: both members of each class were inhibited. Thus, these perturbations did not change the direct connections and input similarities between L-R pairs (Fig.4.36 D-F). This feature of my experimental perturbation strategy therefore served as another internal control. Consistently, I observed that L-R pairs retained high pairwise correlation values in multi-hub targeted animals (Fig.4.38).

In summary, loss of connectivity motifs as well as disrupting short path lengths and input similarities upon inhibiting multiple hub neurons likely account for the global breakdown in global correlations.

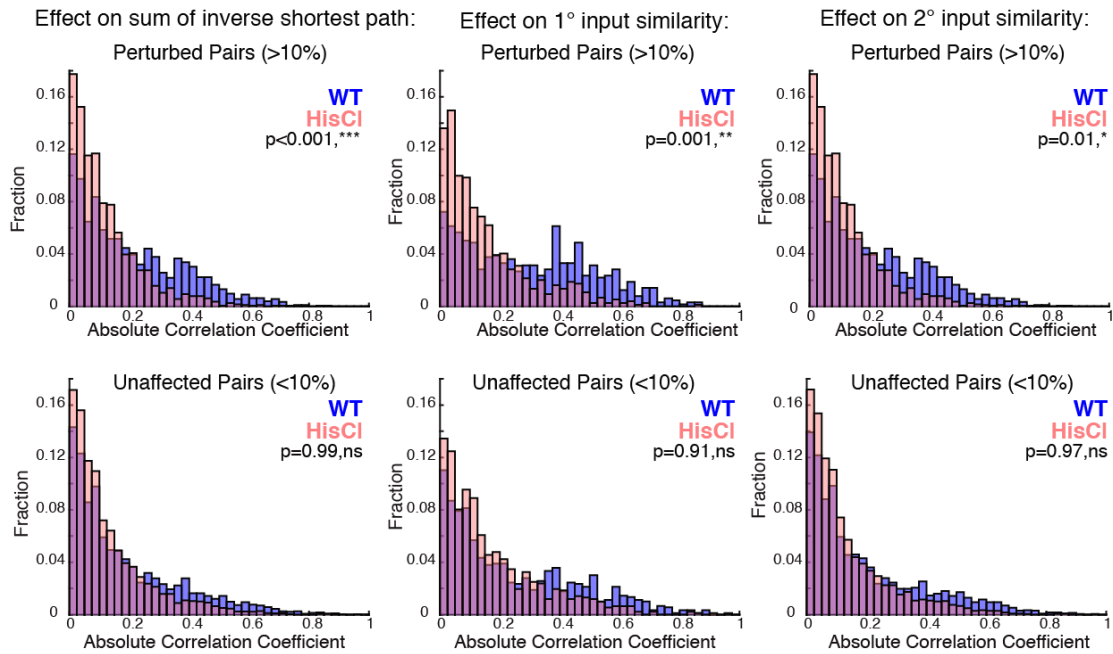


Figure 4.37 Disruptions of connectivity features correlate with impact on pairwise correlations.

Frequency distributions of absolute pairwise correlations from WT (blue) vs. pooled multiple hub inhibition lines (orange). Data were divided into neuronal pairs with the indicated connectivity feature perturbed by more than 10% (top panels, perturbed pairs) versus remainder (bottom panels, unaffected pairs). Permutation p values estimate the probability that KS distance between two distributions was obtained in degree preserved randomized networks. The effect was robust to the cutoff defining perturbed vs. unaffected pairs, shown in Fig.4.36. For all tests in this Figure: ****, $p < 0.0001$; ***, $p < 0.001$; **, $p < 0.01$; *, $p < 0.05$; ns, not significant. Data from $n = 5$ independent recordings from each inhibition line.

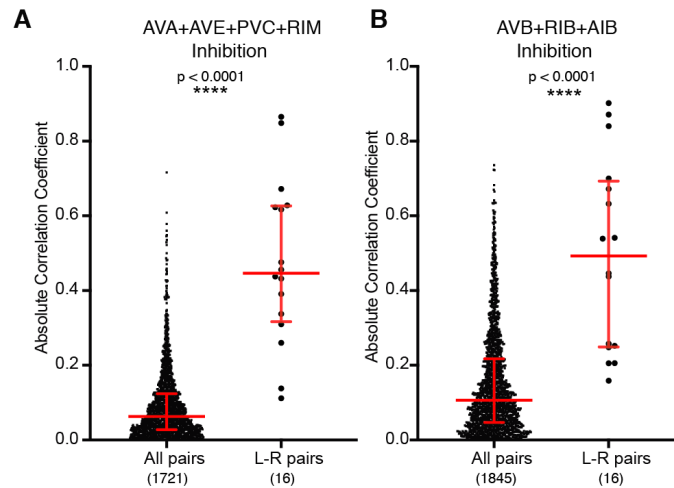


Figure 4.38 L-R pairs retained correlation values in multiple hub inhibition lines.

(A-B) Pairwise correlations grouped by left-right pairs vs all remaining pairs in the network for indicated inhibition lines. Dots show correlations of individual neuronal pairs, red bars indicate median with interquartile range. Asterisks indicate significance level after a custom shuffle test. ****, $p < 0.0001$. Numbers in parentheses indicate number of individual neuron pairs in scatter plots.

5. Discussion

5.1. Probing the network will increase the number of observed brain states

This thesis provides a framework for network-wide analysis of structure-activity relationships and the activity side of this relationship is based on the observed global brain dynamics in the *C. elegans* nervous system which were previously characterized (Kaplan et al., 2020; Kato et al., 2015; Schrödel et al., 2013). It is important to stress that these dynamics occur in sensory deprived and paralyzing experimental conditions which do not require movement or acute sensory stimulation. This means that they are likely driven intrinsically and importantly, they occur spontaneously. Thus, only a subset of all possible neuronal interactions in the worm brain were measured and therefore examined. In future studies, systematically probing the network under different functional contexts using many different sensory stimuli will extend observable neuronal interactions to cover sensory circuits. Importantly, these experiments would also enable testing the importance of other sensory-to-motor network motifs identified previously, but not covered in my activity recordings. These motifs include the “colored motifs” that incorporate the information of neuronal cell types and the connectivity at the same time (Qian et al., 2011), anatomically homogenous motifs that consist of common neighbours (Azulay et al., 2016) and network control principles characterized in locomotor behaviour of the worm (Yan et al., 2017). Furthermore, these experiments would allow the examination of extensive sensory feed-forward network in the *C. elegans* male tail (Jarrell et al., 2012) where community membership makes a better prediction on sensory evoked activity (Susoy et al., 2021).

A previous study from our lab showed that interneuron activity patterns are more stereotypic in paralyzing conditions compared to the ones observed in freely moving worms (Kato et al., 2015). Furthermore, oscillation frequencies of motor-neuron activities were also shown to exhibit a nearly ten-fold increase in freely moving worms (Kaplan et al., 2020). Therefore, it is likely that in unrestrained worms a more diverse set of pairwise interactions could be measured, as a recent study also suggests (Hallinen et al., 2021). Extending my analyses to these experimental setups will be important to expand the structure-function relationships to the whole network and brain states in a similar fashion described above.

A recent concept in neuroscience which is termed as “dynamics on network” explores how a fixed structural network can give rise to various activity patterns (Bassett and Sporns, 2017). This is in parallel with the view of functional motifs (Sporns and Kötter, 2004), where a single anatomical motif class that is dense in terms of connections (e.g. a fully connected triplet motif) can be used by the network with many different versions of its’ subsets in different contexts. This phenomenon is depicted in **Fig.3.3**. Although I employed a structural motif approach throughout this study to eliminate inflated motif statistics (see Chapter 3.4.6) and focused on the exact pattern of the network between neuron groups, the idea of probing the network with delivery of different sensory stimuli would also give an opportunity to test the “functional motif” concept (Sporns and Kötter, 2004).

On the other hand, changes in function can drive changes in structure, termed as “dynamics of network” (Bassett and Sporns, 2017). This term stems from the concept that many physical and biological systems exhibit different patterns of connections that transforms through time, in different situations or response to external stimuli (Bassett and Sporns, 2017). Here I treated the connectome as invariant between individuals; however, it is recently shown that a significant fraction of connections in adult worms are variable between individuals (Witvliet et al., 2020). The delivery of sensory stimuli to drive the network into different brain states would not make changes in the structure of the network in short time scales. However, employing different experimental paradigms to the worms such as entrainment to a certain stimulus for long time scales prior to the whole-brain recordings may provide a means to measure to which extent “dynamics of network” is present in the worms.

Finally, there are recent efforts to bring together both concepts of “dynamics on network” and “dynamics of network” through examining the subsets of networks and their expression pattern. Similar to the structural vs. functional motif concepts of (Sporns and Kötter, 2004), here subsets of the network (subgraphs) are treated as entities that can be present overlapping in space and time but their expression pattern has temporal dynamics (Chai et al., 2017). This is in parallel with the recently proposed framework called “the dynome”, which incorporates brain connectivity, brain dynamics and biological details about connectivity related to its’ function (Kopell et al., 2014). Importantly, this is more

likely to be applicable to longer time scale changes such as the ones existing throughout development and cannot be captured with the current time-limit of the whole-brain imaging paradigm in the worms which can only span minutes to hours.

5.2. Signed and multi-layered connectome might reveal new structure-function relationships

The currently available *C. elegans* connectome does not include any information about the sign of the connections because it is not possible to determine the polarity of a synapse (inhibitory or excitatory) from electron micrographs of *C. elegans* (Varshney et al., 2011) and it is difficult to perform electrophysiology experiments for every possible synaptic couple. However, an improvement could be made by making some approximations. It is known in the *C. elegans* nervous system GABAergic neurons make inhibitory synapses while cholinergic and glutamatergic neurons make excitatory synapses (Brownlee and Fairweather, 1999) (see Chapter 3.1). Critically, there are exceptions to these approximations such as inhibition of AIZ neurons via cholinergic AIY neurons (Li et al., 2014) and inhibition of AIB neurons through glutamatergic AWC neurons (Chalasanani et al., 2007). With the current knowledge which depends on rough assumptions and specific exceptions of neuronal pairs where studies are far from exhaustive in terms of exploring all synaptic pairs, I decided to use nonnegative values for the chemical synapse network throughout this thesis. However, with the new methodologies like optogenetic techniques and calcium imaging, the determination of the polarity of a synapse does not solely depend on electrophysiological methods which will increase the speed of acquiring knowledge about signs of all connections in the network. Once the complete repertoire of *C. elegans* neurotransmitter- and neuromodulator- receptors (Hobert, 2013) is characterized and mapped, it might be possible to extend my analyses to a signed connectome. Recently, a study took the advantage of available gene expression data and predicted the polarity for more than two-thirds of the available connections with the incorporation of information about neurotransmitters expressed in the presynaptic neurons and receptors expressed in the postsynaptic neurons as well as their connectivities (Fenyves et al., 2020). Such efforts (and possibly similar future studies) will greatly help and accelerate the generation of a signed connectome.

On the other hand, considering the gap junction network, I treated all the connections as symmetric within the network. However, there are examples of rectifying gap junctions -connections that pass current preferentially in one direction (Marder, 2009)- such as the gap junctions between AVA and the A-motor neurons which only allow antidromic current and shown to amplify excitatory chemical transmission (Liu et al., 2017). The expansion of the repertoire of such studies in the future, will also transform the gap junction network to a more complete and not totally symmetric (undirected) network. With the current knowledge where only a handful examples are thoroughly examined, I decided to make no assumptions and treated all connections same and symmetric.

Furthermore, *C. elegans* neurons use around 250 neuropeptides (Li and Kim, 2008) and these molecules can be co-released with neurotransmitters (Burnstock, 2004; Chalasani et al., 2010) or can initiate modifications in other cells extrasynaptically. Thus, neurons in the nervous system have another layer of communication on top of the already available synapses. Importantly, I did not take into consideration these possible interactions in this study; however, my analyses could be extended to the extra-synaptic communication networks of neuromodulators (Bentley et al., 2016).

As mentioned above, both chemical synapse and gap junction networks could be modified, and extra-synaptic connections could also be added to the repertoire of networks. The analyses in this study could be applied to the ensemble of all these networks. However, it will also bring challenges. Here I used the combined network of the *C. elegans* connectome which incorporates the information from the gap junction and chemical synapse networks. This step alone expanded the number of dyad motifs from 2 to 6 and triplet motifs from 13 to 259. Thus, the motif analyses throughout this thesis are restricted to include motif classes $n = 2$ and $n = 3$ (dyads and triplets). The addition of signs will also increase the number of motif configurations, thus providing new challenges. Having said that, it will also reveal whether inhibitory or excitatory motifs are in abundance within the connectome. Furthermore, it will reveal the possible enrichment locations of these signed motifs such as transitions from sensory-to-interneurons or from inter-to-motorneurons. Recently, the *C. elegans* connectome was predicted to have excitatory-inhibitory ratio close to 4:1 (Fenyves et al., 2020) which is similar to other parts of brain networks such as rat hippocampus (Gulyás et al., 1999) or

cerebral cortex (Marom and Shahaf, 2002). It would be interesting to see how the distribution of signed motifs correspond to these ratios and find out the contribution of signed connections to signed motifs.

5.3. Improvement of structure-function predictions via input similarities and symmetries

Throughout my analyses about structure-function predictions, direct connectivity did not show a strong relationship with functional interaction (**Fig.4.8**), which is contrary to structure-function studies using human and rodent mesoscale projectomes (Hagmann et al., 2008; Huang et al., 2020). Hagmann *et al.* revealed a structural core within posterior medial and parietal cerebral cortex and found that functional interactions between the regions of cortex were significantly correlated to the structural connectivity patterns (Hagmann et al., 2008). Using mouse as a model organism Huang *et al.* developed a recent method that can combine brain-wide activity recording, connectivity mapping and gene expression acquisition in single animals in a high-throughput fashion (Huang et al., 2020). This study also revealed that there is a significant correlation between connection strength and activity correlation values (Huang et al., 2020). Furthermore, Cossell *et al.* showed functionally the existence of rare strong synapses, embedded within many weak synapses, and their importance for pairwise correlations in primary visual cortex (Cossell et al., 2015).

In general, weighted vs. unweighted connectivity measures performed equally well in predicting functional interactions. Including all known information of synaptic strength did not significantly improve the r_s values when compared to a binarized connectivity measure. This indicates that the here reported structure-function predictions can be made based on the network's topology alone. Here, network topology refers to the scaffold of connections which is embodied by the adjacency matrix and similarities in input patterns which ignores connection strengths (number of synapses) and the count of common inputs to each pair of neurons.

Surprisingly, in my analyses higher order connectivity measures such as input similarity showed a better performance at structure-function predictions. There might be few explanations for this outcome. First of all, it is possible that the number of synapses is a poor proxy for total synaptic strength in *C. elegans* (see Chapter 3.3.2). Alternatively,

the neurons participating in brain-wide population dynamics might be driven by higher order network couplings. This is consistent with my finding that similarities in network neighborhoods and higher-order features to be the best structure-function predictors (**Fig.4.12**).

In densely connected networks, or in subregions of brain networks of many scales that contain densely interconnected regions (van den Heuvel and Sporns, 2011) every neuron receives multiple important inputs. Therefore, direct connections could only represent a subset of each neuron's causal inputs. However, considering the higher-order connections, such as 1° and 2° inputs, increase the fraction of all potential inputs and drivers within the network. This has implications for connectome reconstructions from small sub-volumes in the brain, potentially omitting higher order connectivity features such as 2° inputs that originate in distant brain region not reconstructed. In other words, this result suggests that complete connectomes will be way more informative than local volumes because complete connectomes will provide supra-linearly more information than connectomes of its sub-regions. This conclusion supports the current efforts for fully reconstructing entire brains and nervous systems.

On the other hand, the finding that 1° and 2° input similarities make the best structure-function predictions support the idea that symmetric structure found in the connectome is of high functional relevance in enabling synchronous network states (Morone and Makse, 2019). The substantial improvement of 2° connections is supported by the two main populations of the connectome responsible for the forward- and backward-movements which also show high symmetry levels (Morone and Makse, 2019). Interestingly, I observed an improvement of structure-function predictions when I extended the input similarity analysis from first 1° inputs to 2° inputs. The consideration of secondary layer inputs measures how similar the two network neighbourhoods are upstream of each neuronal pair; thus, it is consistent with the importance of symmetries within the network. This extension step was only done to secondary layer which already generated dense representation of connectivity within the network (**Fig.4.15**) which renders searching for higher orders such as third layers non-feasible for the *C. elegans* network. Having said that, it could be applied to other brain networks with larger nervous systems which will provide an opportunity to test the results of this study.

Importantly, network hubs have an important contribution to 1° and 2° input similarities. This raises a possibility that the improvement in the prediction of structure-function relationships with input similarities stems from the activity patterns of network hubs and their correlated partner neurons. However, the r_s values in **Fig.4.12** and **Fig.4.17** are comparable across all the neuronal pairs and did not correlate with the weight of a neuron in the first two PCs. In other words, pairs that include high PC1/2 weight neurons were scattered throughout the plots in **Fig.4.12 C,F** and did not cluster in the upper right corners. This is quantified in (**Fig.4.13**) to rule out a possible scenario where input similarity metrics enrich neurons only with the same type of linear activity (which should be captured by the first two PC modes). Furthermore, in chapter 4.7, I experimentally tested and validated these results with the perturbation of multiple network hub inhibitions targeting a complete different set of neurons. The predictive power of 1st and 2nd degree neurons is retained in multiple network hub inhibition datasets, where global correlations collapsed (**Fig.4.37**), hence this structure-function relationship is partially evident in a nervous system with global population activity lacking dominant PC modes.

In the perturbation experiments, it is important to note that the effect on correlations of 2° input similarity pairs is less than the effect on correlations of 1° input similarity pairs (**Fig.4.37**, top-middle and top-right histograms). Although perturbing a similar fraction cumulatively (red curves in **Fig.4.36 A-C**) the distributions of perturbations were different between input similarities, this in turn might account for their differential effects on correlations.

5.4. Relationship between genetic identity and connectivity

In this study I found strikingly high correlation values between L-R pairs of the same neuron class (**Fig.4.11**) indicating that genetic programs have a strong influence in establishing gap junction connections and symmetric structures in network neighborhoods. This result is consistent with the previous work in worms and mice that establishes strong links between genetic identity and connectivity (Barabási and Barabási, 2020; Huang et al., 2020). In chapter 4.7, I validated the structure-function relationships found in WT datasets using multiple hub inhibition lines (**Fig.4.35** and **Fig.4.37**). Here, I had the opportunity to use the aforementioned highly correlated L-R neurons as an internal control in these multiple hub inhibition experiments because the genetic drivers used to transgenically express the inhibition tools (HisCl channels) cover

both the left and the right member of each cell-class. In other words, the delivered perturbations to the network were symmetric. This was quantified in **Fig.4.36 D-F** where I showed that these perturbations did not change the direct connections and input similarities between L-R pairs. Consistently, I observed that L-R pairs retained high pairwise correlation values in multiple hub inhibition lines (**Fig.4.38 A-B**). However, one can test the structure-function relationships that involve the L-R pairs via asymmetric perturbations. Since genetic drivers cannot be used for this reason (only exceptions involve sensory neurons AWC and ASE (Cochella and Hobert, 2012; Wes and Bargmann, 2001)), the delivery of asymmetric perturbation is only possible with non-genetic tools such as laser ablation. Laser ablation experiments will provide a means to target only a single neuron within the neuron class which could be only one pair of the L-R pairs or only a single neuron within the motor neuron classes which have many members (e.g. VA neuron class consists of neurons VA1 to VA12). Symmetries and pseudo-symmetries were shown to be important for the formation of the circuit in the *C. elegans* connectome and especially enriched in forward and backward movement circuit among the motor neurons (Morone and Makse, 2019). With the laser ablation technique these symmetries within the network could be broken down and my studies can be extended to test the contribution of symmetries to the generation of synchronous activity patterns between the neurons.

5.5. Temporal dynamics of neuronal inhibition methods

Another important aspect of the genetic inhibition tools used in this study is its temporal control. HisCl channels allow the temporal control of the genetic inhibition to be triggered by the incubation of animals with histamine (Pokala et al., 2014). As a result, I was able to circumvent any possible defects during the development of the nervous system. All the animals were developed similar to the WT strains up until the point of histamine incubation which is only ~30 minutes prior to the whole-brain imaging recordings (see Methods). This was an advantage of the HisCl method. However, this inhibition is not acute and rely on the incubation of animals for a rather long-time window (~30 minutes); thus, I can only image a nervous system where the targeted neuron is already inhibited and a network exhibiting an already perturbed brain dynamics within my recordings. Therefore, the possibility of observing the very moment of disruption does not exist. On the other hand, other methods such as optogenetics which

depends on activation/inhibition through light can act in much more faster timescales (milliseconds to seconds instead of minutes) that would allow the inspection of the brain dynamics while it is being perturbed. Previously the experimental setup of whole-brain imaging is successfully coupled to the delivery of a chemosensory stimulus (Kato et al., 2015), the same time window is sufficient to test the outcomes of acute perturbations using optogenetic tools. The global brain dynamics that were under study throughout this thesis were previously characterized (Kato et al., 2015) and I extended this method to also cover the tail ganglia of the worms (**Fig.4.1 A-B**). I then proceeded with the confirmation of recapitulating these results (**Fig.4.1 D**). Although I delivered many perturbations using single or multiple network hub inhibition lines, further characterization of the brain dynamics of WT datasets were outside of the scope of this study. Therefore, I examined the anatomical substrates that support the brain dynamics and delineated structure-function relationships and next, compared the perturbed networks to WT datasets in the light of these structure-function relationships. However, with the delivery of acute perturbation via optogenetics, my studies can be extended to cover further characterization of the dynamics such as revealing more information about the robustness or attractor properties of network activity. Within my WT datasets the neuronal recruitment rules are extremely reliable, i.e. individual neurons are reproducibly and exclusively activated and inactivated during specific network states (this study, (Kato et al., 2015)). Acute perturbation through optogenetic interrogation of individual neurons or subgroups of neurons will force the network to form artificial states; thus, the stability of the network dynamics will be tested. For instance, if the brain dynamics exhibit attractor properties, the forced unnatural network state is expected to dissolve rapidly and brain state is expected to return back to previously identified stable network patterns which was previously shown to be the case in other nervous systems (Bruno et al., 2017).

5.6. Role of neurotransmitter pathways in neuronal population dynamics

The molecular mechanisms that neurons use to form and maintain global brain dynamics form another important aspect. In order to identify these molecular mechanisms and understand their contribution to the coordinated patterns within the network, the involved neurotransmitter pathways could be examined. Most major neurotransmitter pathways (glutamate, GABA, acetylcholine, serotonin, dopamine and neuropeptides) are

conserved in *C. elegans* (Hobert, 2013); importantly mutant strains lacking functional genes in the biosynthesis of these neurotransmitters are viable. Testing these strains might give new insights about the role of an individual pathway in patterned network activity. Furthermore, transgenic rescue experiments might reveal the crucial neurons releasing the neurotransmitter. A similar approach could be applied to neurotransmitter receptor genes, revealing the crucial target neurons. These experiments could be performed via transgenic expression of WT genes under the control of cell specific promoters. These experiments will also provide support for one of the two hypotheses: i) if pacemaker neurons dictate a signal to the whole network, locally expressed neurotransmitters or gap junctions must be crucial for the generation of the network states; ii) if every single neuron has its own intrinsic activity and then their synchronization generates the patterns in the network, multiple neurotransmitter pathways will be involved and have partial roles in the generation of the network state. By targeting neurotransmitter pathways and assessing their impact to the brain dynamics, their role in the formation of brain dynamics as well as their important cellular sources could be identified. Although not complete (see Chapter 3.3.2), we know the neurotransmitter identity of most of the connections within the network; thus, the *in silico* perturbation equivalent of such neurotransmitter mutants could be generated and added to perturbation screen in chapter 4.5 (**Fig.4.18** and **Fig.4.21**). This will provide an opportunity to test and validate the results of this study.

5.7. Contribution of the dominant PC modes to structure-function relationships

As previously characterized and further confirmed in this study whole-brain imaging datasets exhibit dominant modes. These PC modes (specifically PC1 and PC2) receive contributions from interneurons, pre-motor interneurons, head-motor neurons (Kato et al., 2015) and also from motor neurons throughout the ventral nerve cord (Kaplan et al., 2020). On the other hand, these datasets are not simply one-dimensional and contain multiple correlation clusters with sub-structures (**Fig4.3 A**). To put this aspect of the datasets on a quantitative ground, I calculated the ‘shared dimensionality’ (Owen and Perry, 2009; Stringer et al., 2019) and ‘effective dimensionality’ (Abbott et al., 2011) to reveal that my datasets exhibit a lower bound of 3-5 dimensions (effective dimensionality: 3.34 ± 0.43 , shared dimensionality: 8.17 ± 1.33 , **Fig.4.2**). Having said that, these dominant PC modes must have a contribution to the triplet motifs found in

Fig.4.9. A major conclusion of this study is that hub interneurons are crucial in recruiting neurons to global population dynamics via rich club topology, motifs and symmetries. These hubs and their connections constitute 52% of all connections in the connectome and they are heavily embedded to their neighboring neurons via triplet motifs (**Fig.4.22**). As a result, many correlations in the triplet motifs arise indeed from these hub neurons and their partners. Thus, it must be stated that triplet motifs consist of many correlations that are not local and independent of the global system, but these motifs provide the structural elements that support pairwise correlations by recruiting neurons to global population dynamics.

In order to support this statement, I performed few controls. First, I employed a rule where we removed the duplicates of a given pair from the functional map when analyzing motifs (see Methods). This prevents the artifact of having very skewed distributions stemming from a single neuronal pair (for instance a high pairwise correlation between two hub neurons), embedded in the same motif many times. This rule prevents the triplet motif analysis to be heavily influenced by only a specific circuit or a set of neurons. Thus, the members of these motifs are scattered throughout the neurons that we study and do not exclusively localize to high PC1 weighted neurons.

Second, statistics were performed rigorously by comparing to matched controls, i.e. pairs with the same direct connectivity motif, which are not members of the particular triplet motif. These control pairs are drawn from the same set of neurons and can also contain high correlations (see tail of distribution in **Fig4.9 A**), and they also contain hub neurons. Therefore, I conclude that triplet motifs likely recruit neurons to the global population activity by strengthening pairwise correlations, more so than direct connectivity motifs. However, the correlations within motifs are not entirely local correlations fully independent of the global population dynamics. **Fig.4.35 C and E** also suggest that motifs are not the sole source of correlations but rather one of the important contributors.

Third, as discussed in chapters 4.7 and 5.9, my results suggest that neuronal population dynamics are not driven by a single or a few pacemaker neurons but arise as an emergent property. This conclusion is strongly supported by the experimental result of AVA-AVE-RIM-PVC inhibition (**Fig.4.27**). Global population dynamics collapse in these worms, but most neurons retain vigorous activity. In the absence of this global patterned activity,

the remaining correlations between the neurons were partially retained when they are supported by the motifs left intact (**Fig.4.35 B**). This result suggests that significant triplet motifs are -although partial- responsible for the correlation of neurons throughout the nervous system.

5.8. The role of rich club organization within the network

Many connectomics studies revealed different circuit architectures that are suited for specific functions in various brain networks such as visual motion detection (Helmstaedter et al., 2013; Takemura et al., 2013), odorant representation (Dasgupta et al., 2017; Wanner and Friedrich, 2020), ring-attractor dynamics (Takemura et al., 2013; Turner-Evans et al., 2020) and learning (Eichler et al., 2017; Eschbach et al., 2020). Rich club architectures in larger brains, including humans, were described both on a global scale (van den Heuvel and Sporns, 2011) as well as on the level of *in silico* reconstructed rodent neocortical microcircuits (Gal et al., 2017). It was discussed that rich club architecture serve efficient global communication (de Reus and van den Heuvel, 2014); thus, it is crucial for network integration and plays a role as the connective core of the network (Shanahan, 2012).

In *C. elegans*, information about the ongoing behavioral state is widely shared among motor and sensory circuits (Kato et al., 2015). This feature is not specific to worms but also were shown other animals such as flies (Aimon et al., 2019) and mice (Musall et al., 2019; Salkoff et al., 2020; Stringer et al., 2019). My study suggests that rich club architecture plays a key role in synchronizing these different circuit elements to generate a global representation of behavior. Consistent with this view, hubs within the network have been shown to play important roles in shaping neural dynamics in other studies too. A subset of high-degree neurons is shown to be responsible for network synchronization in hippocampus (Bonifazi et al., 2009) and entorhinal cortex (Mòdol et al., 2017) and for the transfer of information in local cortical networks (Nigam et al., 2016). These studies support the idea that rich club neurons play a key role in networks which compensates their high wiring cost through long-distance synaptic connections at network integration. My results are in parallel with these studies where network hubs are the ones that shows strongest activity patterns (**Fig.4.6**) with strong participation to the global brain dynamics and providing the network features (**Fig.4.22 and Fig.4.23**) to support and recruit other

neurons to these dynamics. Upon their disruption with multiple hub inhibition lines the WT brain dynamics were perturbed and unable to generate similar coordination levels and correlated structures (**Fig.4.27**).

Importantly, the neuronal activity correlations analyzed in this study can be robustly observed across various conditions like in well-fed adults off food (this study, (Kaplan et al., 2020; Kato et al., 2015; Schrödel et al., 2013)), during larval development and in the presence of food (Nichols et al., 2017) as well as after short-term and long-term starvation (Skora et al., 2018). This is consistent with the robustness of the action sequence, which is represented by these brain dynamics; but also suggests that the network's topology persists across these conditions. My analyses, however, suggest that a substantial amount of variation in synaptic weights can be tolerated (**Fig.4.17**) and is not expected to affect global activity correlations. Consistently, during the course of *C. elegans* development network hubs are the earliest born neurons (Towlson et al., 2013), and connections between high-degree network-hubs are the least variable ones, both across development and across individuals (Witvliet et al., 2020). This results further corroborate the importance of the network hubs for the generation and maintenance of the global population dynamics within the *C. elegans* neuronal network.

5.9. Neuronal population dynamics as an emergent property

In this study, I focused on the neuronal population dynamics observed in my WT datasets to delineate the structure-function relationships and validated these relationships through genetic inhibition of network hubs. This experimental paradigm also gave me the opportunity to provide insights on the origin of the observed global brain dynamics. Many previous studies commonly reported that groups of neurons are involved in a network activity which is coordinated and patterned (Ahrens et al., 2012; Briggman et al., 2005; Bruno et al., 2017; Churchland et al., 2012; Shine et al., 2019; Stopfer et al., 2003) (see Chapter 3.2). However, how such network activity is generated in the first place and how population structure is achieved is not known yet for any organism. Network activity patterns could be emergent; arising from synaptic coupling of many neurons that have unique intrinsic activities. Or alternatively, they could be instructed by crucial pacemaker neurons.

If there are pacemaker neurons within the network, it is more likely that they are high degree network hubs which belongs to the rich club architecture of the network (see Chapter 3.5). Because the generation of a global signal that dictates a certain activity pattern to many neurons will require a high degree that allows reaching to many synaptic partners and possibly with high connection strength. Throughout this study I have targeted seven single neuron classes which are all network hubs (**Fig.4.23**). This list contains neurons with very high degrees as well as neurons with known essential functions in the core command sequence that corresponds to the behaviour of the animals (**Fig.4.1 D**). These essential functions include being the command interneurons (AVA, AVB, AVE and PVC) or being involved in the transition of forward-to-turn (RIB) or backward-to-turn movements (AIB, RIM) (see also Chapter 3.7). Importantly in neither of these single cell inhibition lines I did not observe a drastic global correlation change. All of these inhibition lines retained the global cycles where I observed the transitions between important clusters of forward and backward neurons (**Fig 4.31 and Fig.4.32**) albeit with different frequencies (**Fig.4.29 and Fig.4.30**). The retainment of these transitions suggests that there are no important key neurons responsible for these switches, rather these observed states are network states which involves the recruitment of many neurons. Thus, these states are generated in a distributed manner throughout the brain and robust to the perturbation of single neuron classes.

Importantly, I did not observe any change in remaining neuronal activity levels after single neuron inhibitions rendering the possibility of having pacemaker for certain brain states less likely. For instance, AVA and AVB are bottlenecks in the connectome linking the other hub neurons to the A- and B-class motor neuron pools in the ventral nerve cord, which are required for execution of reverse and forward crawling respectively (Chalfie et al., 1985; Kawano et al., 2011; Wen et al., 2012). While AVA and AVB targeted animals cannot execute these behaviours (**Fig.4.28**), and fail to activate A- and B-class motor neuron pools (**Fig.4.29 A, Fig.4.30 A**), brain wide forward and backward motor commands persisted; corroborating a previous conclusion and prediction that AVA and AVB should not be seen as the sole command interneurons, but rather as outputs of a robust command network (Kaplan et al., 2018; Kato et al., 2015).

Furthermore, within the single cell inhibition experiments, although both are non-significant globally, the effects of second-layer interneurons (RIM and RIB) were comparable (or even stronger in some cases) than the effects of command interneurons (AVA, AVE, PVC, AVB) which have more synaptic partners and connections in the connectome, indicating that the removal of key connections has a more substantial effect on synchronizations than the removal of many connections. Having said that, these effects were only confined to a single cluster within the correlated structures of the network (**Fig.4.33**). Usually, this cluster is the where the targeted neuron is implemented within the circuit: correlation within the forward cluster decreased significantly with the inhibition of AVB and RIB (**Fig.4.33 D,F**). The only exception for this was the inhibition of RIM neurons where I also observe a significant loss in the forward cluster (**Fig.4.33 I**), although RIM interneurons are implicated in backward movement and found active in backward movement brain states (this study, (Kato et al., 2015)). This effect is partially due to the reduction in number of brain cycles within the recordings (**Fig4.34 A**). This decrease translates as long forward movement brain state stretches (traces can be seen in **Fig.4.34 B**) where the neurons belonging to this cluster exhibits more dynamic activity patterns and thus the correlation calculation that takes into account the whole recording fail to produce WT level coefficients. However, even this perturbation failed to generate a difference in global correlation levels.

Critically, the disruption of global correlation levels can only be achieved with the multiple inhibition of network hubs. The observation that nearly all neurons remained vigorously active, though uncoordinated, in AVA-AVE-RIM-PVC animals, countervails the notion that neuronal population dynamics are driven by a single or few pacemaker neurons, but rather arise as an emergent property, further corroborating the importance of network architecture in generating coherent brain states and subsequent behaviors.

6. Materials and Methods

6.1. Worm culture and strains

All *C. elegans* strains were maintained on nematode growth medium (NGM) at 20°C, and hermaphrodites were used for all experiments. Strain genotypes are listed in **Table 6.1**.

6.1.

Table 6.1: Detailed list of strains used in this study

Strain name	Experiment	Genotype	Construct (plasmid no.) and injection concentrations	Promoter expression references
ZIM1428	Whole-brain imaging	MzmIs52; <i>lite-1</i> (<i>ce314</i>)	<i>Punc-31</i> ::NLSGCaMP6f (pTS100) 2.5ng/ul;	(Schrödel et al., 2013)
ZIM805	Whole-brain imaging, AIB- Inhibition	<i>mzmEx199</i> ; <i>mzmEx459</i> ; <i>lite-1</i> (<i>xu7</i>)	<i>Punc-31</i> ::NLSGCaMP5K (pTS36) 30ng/μL; <i>Pinx-1</i> ::HisCl::SL2::mCherry 50 ng/μL;	<i>Pinx-1</i> (Altun et al., 2009);
ZIM756	Whole-brain imaging, AVA- Inhibition	<i>mzmEx199</i> ; <i>kyEx4863</i> ; <i>lite-1</i> (<i>xu7</i>)	<i>Punc-31</i> ::NLSGCaMP5K (pTS36) 30ng/μL; <i>Punc-122</i> ::gfp 15ng/μL; <i>Prig-3</i> ::HisCl1::SL2::mCherry (pNP471) 50 ng/μL	<i>Prig-3</i> (Pokala et al., 2014)
ZIM1860	Whole-brain imaging, AVB- Inhibition	MzmIs52; <i>lite-1</i> (<i>ce314</i>); <i>mzmEx578</i>	<i>Punc-31</i> ::NLSGCaMP6f (pTS100) 2.5ng/ul; <i>Psra-11</i> ::HisCl::SL2::mCherry (pRL123) 50 ng/μL; <i>Pflp-17</i> ::mCherry 1.5ng/uL	<i>Psra-11</i> (Troemel et al., 1995)
ZIM2020	Whole-brain imaging, AVE- Inhibition	MzmIs52; <i>lite-1</i> (<i>ce314</i>); <i>mzmEx1223</i> ;	<i>Punc-31</i> ::NLSGCaMP6f (pTS100) 2.5ng/ul; <i>Popt-3</i> ::HisCl::SL2::mCherry (pKU33) 30ng/uL;	<i>Popt-3</i> (Fei et al., 2000)
ZIM755	Whole-brain imaging, RIB- Inhibition	<i>mzmEx199</i> ; <i>mzmEx457</i> ; <i>lite-1</i> (<i>xu7</i>)	<i>Punc-31</i> ::NLSGCaMP5K (pTS36) 30ng/μL; <i>Psto-3</i> ::HisCl::SL2::mCherry (pHK170) 20 ng/μL;	<i>Psto-3</i> (Kato et al., 2015)
ZIM1720	Whole-brain imaging, RIM- Inhibition	MzmIs52; <i>lite-1</i> (<i>ce314</i>); <i>mzmEx973</i> ; <i>mzmEx976</i>	<i>Punc-31</i> ::NLSGCaMP6f (pTS100) 2.5ng/ul; <i>Punc-122</i> ::dsRed 19ng/μL; <i>Pcex-1</i> ::CreVDH (pKU26) 15ng/μL; <i>Ptdc-1</i> ::DIO-(HisCl::SL2::mCherry) (pKU28) 12.5ng/uL; <i>Pelt-2</i> ::NLSGFP 5ng/uL	<i>Ptdc-1</i> (Alkema et al., 2005) CreVDH (Ruijtenberg and van den Heuvel, 2015); DIO (Sohal et al., 2009)

Strain name	Experiment	Genotype	Construct (plasmid no.) and injection concentrations	Promoter expression references
ZIM1810	Whole-brain imaging, PVC-Inhibition	MzmIs52; <i>lite-1</i> (<i>ce314</i>); mzmEx973; mzmEx974	<i>Punc-31::NLSGCaMP6f</i> (pTS100) 2.5ng/ul; <i>Punc-122::dsRed</i> 19ng/μL; <i>Pcex-1::CreVDH</i> (pKU26) 15ng/μL; <i>Pdes-2::DIO-(HisCl::SL2::mCherry)</i> (pKU23) 25ng/uL; <i>Pelt-2::NLSdsRed</i> 5ng/uL	<i>Pdes-2</i> (Treinin et al., 1998); <i>CreVDH</i> (Ruijtenberg and van den Heuvel, 2015); <i>DIO</i> (Sohal et al., 2009)
ZIM2312	Whole-brain imaging, RIM+PVC Inhibition	MzmIs52; <i>lite-1</i> (<i>ce314</i>); mzmEx973; mzmEx974; mzmEx976	<i>Punc-31::NLSGCaMP6f</i> (pTS100) 2.5ng/ul; <i>Punc-122::dsRed</i> 19ng/μL; <i>Pcex-1::CreVDH</i> (pKU26) 15ng/μL; <i>Pdes-2::DIO-(HisCl::SL2::mCherry)</i> (pKU23) 25ng/uL; <i>Pelt-2::NLSdsRed</i> 5ng/uL <i>Ptdc-1::DIO-(HisCl::SL2::mCherry)</i> (pKU28) 12.5ng/uL; <i>Pelt-2::NLSGFP</i> 5ng/uL	
ZIM1807	Whole-brain imaging, AVA+AVE+ RIM+PVC Inhibition	MzmIs52; <i>lite-1</i> (<i>ce314</i>); mzmEx462	<i>Punc-31::NLSGCaMP6f</i> (pTS100) 2.5ng/ul; <i>Pcex-1::HisCl::SL2::mCherry</i> (pRL122) 50 ng/μL; <i>Pflp-17::mCherry</i> 1.5ng/uL <i>Pcex-1</i> was previously reported to drive expression only in RIM. I confirmed that it drives strong expression in RIM and PVC also weak expression in AVA and AVE that are sufficient to successfully inhibit all 4 neuron classes (Fig.4.25 A) in ZIM1807 (injected 50 ng/μL).	
ZIM1935	Whole-brain imaging, AVB+RIB+ AIB Inhibition	MzmIs52; <i>lite-1</i> (<i>ce314</i>); mzmEx463; mzmEx578; mzmEx1114	<i>Punc-31::NLSGCaMP6f</i> (pTS100) 2.5ng/ul; <i>Psto-3::HisCl::SL2::mCherry</i> (pHK170) 5 ng/μL; <i>Punc-122::dsRed</i> 19ng/μL; <i>Psra-11::HisCl::SL2::mCherry</i> (pRL123) 50 ng/μL; <i>Pflp-17::mCherry</i> 1.5ng/uL; <i>Pinx-1::HisCl::SL2::mCherry</i> (pKU31) 50 ng/μL; <i>Pelt-2::NLSdsRed</i> 5ng/uL	<i>Pinx-1</i> (Altun et al., 2009); <i>Psra-11</i> (Troemel et al., 1995); <i>Psto-3</i> (Kato et al., 2015)

6.2. Whole-Brain calcium imaging of *C. elegans* head and tail ganglia neurons

Whole-brain calcium imaging experiments were performed as described previously (Kato et al., 2015) using transgenic adult *C. elegans* (1 day after larval L4 stage, 5-10 eggs) expressing pan-neuronal genetically-encoded calcium indicator NLS-GCaMP6f (Chen et al., 2013) and bearing a mutation in the *lite-1* gene (*ce314* allele) which decreases responsiveness to UV and blue-light (Edwards et al., 2008; Gong et al., 2016;

Liu et al., 2010). Animals were imaged in two-layer PDMS microfluidic devices to control O₂ environment (Zimmer et al., 2009) and with curved worm channels to immobilize and laterally align animals (Cáceres et al., 2012; Kato et al., 2015; Schrödel et al., 2013). This curve was designed to reduce the necessary imaging area by aligning the animal's head and tail. With this design, all neurons in the head and tail ganglia of the worm, the retro vesicular ganglion as well as multiple motor neurons along the ventral cord can be imaged simultaneously (**Fig.4.1 A**). The worm channel of the microfluidic device was connected to a syringe which contains NGM buffer with 1 mM tetramisole. All components were connected using Tygon tubing (0.02 in ID, 0.06 in OD; Norton) using 23G Luer-stub adapters (Intramedic). Constant gas flow of 21% O₂ and 79% N₂ (50ml/min) was delivered using a gas mixer connected to mass flow controllers (Vögtling Instruments) using LabView software. Adult worms (5-10 eggs) were picked on food-free NGM agar plates in a drop of NGM with 1mM tetramisole and aspirated into the worm channel. The fluorescence values were recorded 10 min after loading; the illumination and piezo stage were switched on 2 min before acquisition start. Animals were imaged at 21% O₂ for 18 min. High-resolution data of neuronal activity in the head and tail ganglia was acquired with an inverted spinning disk confocal microscope (Zeiss Axio Observer.Z1 with attached Yokogawa CSU-X1) using an EMCCD camera (Photometrics Evolve 512) and a 40x 1.2 LD LCI Plan- Apochromat water-immersion objective (Zeiss) with VisiView software (Visitron Systems GmbH Exposure time was 10ms, with 2µm steps between Z-planes operated by a Piezo stage (P-736 PI nano, Physik Instrumente GmbH). These settings allowed an imaging rate of 3.06–5.04 volumes per second with 14-15 planes. In inhibition experiments, worms from HisCl expressing lines were incubated for 30-45 min on OP50 seeded NGM agar plates including 20 mM histamine (histamine dihydrochloride, Sigma-Aldrich) before loading them into the worm channel filled with NGM containing 20 mM histamine.

6.3. Neural time series extraction

As described before (Kato et al., 2015), neuronal activity traces were obtained by tracking the intensity maxima in each volume over time and calculating the single-cell fluorescence intensities (F). F_0 was calculated as the mean fluorescence intensity across the trial. After background subtraction, DF/F_0 was calculated for each neuron, following bleach correction by linear detrending and exponential fitting.

6.4. Identification of head and tail ganglia neurons

In each recording, we detected 133–154 neurons, covering 58%-67% of expected neurons in the imaging area. We only identified neurons that were active in the datasets (66 neurons on average in WT datasets, **Fig.4.3 A**). The remaining neurons were either recorded but not active or not captured in our recordings due to very low fluorescent levels. Also, we cannot exclude that the fluorescent label is not expressed in a small fraction of neurons. Neurons were identified as previously described (Kato et al., 2015) by taking into account their anatomical positions, relation to surrounding neurons (<http://www.wormatlas.org>), their characteristic activity patterns and our experience with red fluorophore expression in specific marker lines reported in previous studies (Kaplan et al., 2020; Kato et al., 2015; Nichols et al., 2017; Skora et al., 2018). In the present study, we additionally confirmed all of these previous identities using the new NeuroPAL method (Yemini et al., 2021). Neurons in the tail, which have not been identified previously (PHA, ALN, VD13, VA12, DA09, AS10, DA07, DB07, VB11), have been identified here using the NeuroPAL method (Yemini et al., 2021). Only a single researcher identified all datasets in the study.

Average correlation matrices were generated by calculating the mean (n=2-6) pairwise correlations between the activity time-series of identified active neurons. The identified active neuron numbers for WT (**Fig.4.3 A**) and inhibition lines (**Fig.4.27 A-B; Fig.4.31 A-D; Fig.4.32 A-C**) are as follows: WT, 66 neurons; AVA-AVE-RIM-PVC inhibition, 64 neurons; AVB-RIB-AIB inhibition, 63 neurons; RIM-PVC inhibition, 57 neurons; RIM inhibition, 60 neurons; PVC inhibition, 64 neurons; AVE inhibition, 60 neurons; AVA inhibition, 45 neurons; AVB inhibition, 63 neurons; RIB inhibition 44 neurons; AIB inhibition 48 neurons. AIB, RIB and AVA inhibition datasets include only head ganglia recordings with 120-140 neurons. AVA inhibition datasets are from ref (Kato et al., 2015) and several neuron IDs from these datasets were corrected (SMBs to SMDs; SIBs to SIAs; OLQs to URYs).

6.5. Leave-one-out procedure to test the robustness of correlation values

To check for possible deviations from the average correlation value of a single neuronal pair within individual recordings, we performed a leave-one-out procedure. Here a new average correlation for every neuronal pair is re-calculated with the absence of a single recording, then the deviations of these values from the original average correlation

coefficient (absolute difference) were calculated. Deviations from the mean across the individual datasets are available in **Fig.4.4 B**.

6.6. Derivatives on neural time series data

Total-variation regularization (Chartrand, 2011) was used to compute de-noised time derivatives.

6.7. Effective dimensionality

We calculated effective dimensionality (D_{eff}) which represents the eigenvalue distribution along different modes (Abbott et al., 2011; Gurnani and Silver, 2021). Where M is the number of modes, if the variance is equally distributed along the modes, then $D_{eff} = M$. On the other hand, if one mode dominantly captures most of the variance D_{eff} will be close to

$$D_{eff} = \left(\sum_{i=1}^K \hat{\lambda}_i^2 \right)^{-1} \quad \text{where} \quad \hat{\lambda}_i^2 = \frac{\lambda_i^2}{\left(\sum_{i=1}^K \lambda_i \right)^2} \quad 1.$$

λ_i is an eigenvalue of the covariance matrix.

6.8. Shared dimensionality

As an alternative dimensionality measure, we used shared dimensionality with the code provided by (Gurnani and Silver, 2021). It is based on the calculation of cross-validated explained variance (CVEV) to identify shared population modes (Owen and Perry, 2009; Stringer et al., 2019). The data is divided into training (70%) and test (30%) sets, and the training data decomposed to find the loadings (U). we then trained the top K modes, and the corresponding loadings (U^K , first columns of U) to quantify the explained variance by this K -dimensional reconstruction of the population activity. Data was further split into second partition of training neurons ($X1$, 80% of the population) and test neurons ($X2$, 20% of the population).

Then, to estimate the reliable population modes the mean CVEV curves of 200 iterations for each dataset were calculated. In the original method (Gurnani and Silver, 2021) the peak of the relationship between explained variance and number of modes (K) was chosen as the number of reliable population modes (shared dimensionality). Instead of the peak of the CVEV curve, we picked the changepoint in the slope as the shared dimensionality which results in a lower bound for dimensionality.

6.9. Calculating the residual activity of neurons

Residual activity of neurons was calculated by projecting out the top modes (**Fig.4.14**). The population activity is decomposed using SVD and then reconstructed using all the modes except the indicated number of modes (**Fig.4.14**).

6.10. Brain state transition quantification

For **Fig.4.34 A**, reverse and forward command states were inferred from the activity of interneuron AVA, as previously described (Kato et al., 2015). In summary, time points of falling Ca^{2+} transients and low intensity Ca^{2+} signals were defined as forward command states. Time points of rising Ca^{2+} transients and high intensity Ca^{2+} signals were defined as reversal command states.

6.11. Identification of backward and forward clusters

The participation of neurons to backward and forward clusters in **Fig.4.33** were calculated by sorting them according to their mean weight on PC1 in WT datasets. A threshold of +0.4 and -0.4 was used to identify backward and forward cluster neurons, respectively. Backward neurons were AVAL, AVAR, RIML, RIMR, AIBL, AIBR, AVEL, AVER, AS10, VA11, DA07, SABD, DA01, VA01 and forward neurons were AVBL, AVBR, RIBL, RIBR, DVA, DB07, VB11, SIADL, SIADR, SIAVL, SIAVR, DB02 RMEV, RMED, VB01.

6.12. Population behavioural assays

Behaviour assays in **Fig.4.26** and **Fig.4.28 A-G** were performed as described previously (Kato et al., 2015). 20-25 worms (young adults, 1 row of eggs) grown on OP50 seeded food plates were picked on NGM agar plate without food. The 25 mm x 25 mm assay arena was confined by Whatman paper soaked with 20 mM CuCl_2 to repel and prevent worms from leaving the arena. Constant gas flow of 21% O_2 and 79% N_2 (25 ml/min) for 6 min was delivered through a transparent plexiglas device with a flow arena of 39 mm x 39 mm x 0.7 mm placed on top of the assay arena. Gas flow was controlled using a static gas mixer connected to mass flow controllers (Vögtling Instruments) using LabView software. Gas mixtures were balanced using N_2 to maintain constant gas flow. Arenas were illuminated with red LEDs and movies were recorded at 10 fps using a 4 megapixel CCD (Jai) camera and Streampix software. Movie analysis and reversal

detection was performed using Matlab-based tracking software as described before (Chalasanani et al., 2007; Ramot et al., 2008; Zimmer et al., 2009). Worms were pre-incubated at constant 21% O₂ on the assay arena for 5 min before recordings were started to accustom them to the gas flow. Prior to picking onto the assay plates, worms were incubated for 30-45min on plates with NGM agar including either 20mM histamine (+His; histamine dihydrochloride, Sigma-Aldrich) or an equal volume of water (Ctrl) and seeded with OP50 across the entire agar surface to enhance histamine uptake. Recordings were performed on +His and Ctrl assay plates.

6.13. Posterior harsh touch assays

For touch assays (**Fig.4.28 H**) I followed the protocol in ref (Li et al., 2011), posterior harsh touch was applied with a platinum wire pick in a top-down manner. Worms were incubated for 30-45min on +His or Ctrl plates seeded with OP50 across the entire agar surface to enhance histamine uptake. Harsh touch assays were performed on the same plates after incubation. Each worm was tested for 5 trials with 2 min intervals between trials and their responses were scored. Posterior touch was delivered to non-moving animals.

6.14. Activity measures

6.14.1. Correlation coefficient

Pearson's correlation coefficient was calculated in a pairwise manner between all identified neurons' traces in whole-brain imaging datasets.

6.14.2. Cross correlation coefficient

Maximum cross correlation values (Pearson's correlation coefficient) were calculated between neuronal pairs. Maximal lag of 10 seconds was imposed, and the absolute maximum of the values was selected.

6.14.3. Mutual information

Mutual information (MI) was computed between neuronal pairs using the toolbox provided in ref (Ince et al., 2017). The method first transforms each univariate marginal to be a standard normal via a Gaussian parametric MI estimate (thereby called Gaussian-

copula Mutual Information); thus, obtains a lower bound estimate of the MI (Ince et al., 2017).

6.14.4. Covariogram analysis

Covariograms were calculated as described previously (Kaplan et al., 2020). Shortly, Ca^{2+} -events were detected by selecting peaks in the time-derivatives using a method that reduces the number of arbitrary parameter choices (Kaplan et al., 2020). Covariograms report the frequency of a target neuron's peak at different time delays relative to a reference neuron's peak. This calculation contains several steps. First, for each neuron pair raw cross-correlograms were computed in 5s bins. Raw cross-correlograms were then converted into frequencies by dividing by the number of available data in each bin. Next, 100 resampled raw cross-correlograms were computed by random selection of same number of spikes which act as the shuffle predictor (Brody, 1999). Covariograms were finally computed by subtracting the shuffle predictor from the raw cross-correlograms. For each neuronal pair two different covariogram values were calculated because the order of target and reference neurons were swapped. Thus, covariogram-analysis represents a directed (asymmetric) measure of functional interactions used in the systematic structure-function relationship survey.

6.15. Randomized networks

6.15.1. Totally randomized networks

For the calculation of input similarities in **Fig.4.16** and the p value calculation in **Fig.4.17**, we calculated the sum of chemical synapse and gap junction networks of the intact connectome and shuffled the connections to generate totally random networks. These matrices preserve the total connection number within the network.

6.15.2. Degree-preserved randomized networks

For the p value calculation in **Fig.4.7**, **Fig.4.12 C,F**, **Fig.4.17 A-B** degree-preserved random matrices were used. We generated these matrices with the *randmio_dir* function from the Brain Connectivity Toolbox (BCT) (Rubinov and Sporns, 2010) using the sum of chemical synapse and gap junction network. In summary, this function generates a matrix where every neuron preserves the in- and out- degrees but change their connection partners.

6.15.3. Degree-, reciprocal connections and gap junction-chemical synapse likelihood preserved randomized networks

For the over-representation analysis of the motifs (**Fig.4.9 A**, **Fig.4.10 A**) and p value calculation in **Fig.4.17 B**, we generated random matrices that preserve i) degree distribution, ii) reciprocal chemical synapse number and iii) gap junction-chemical synapse likelihood. As previously shown reciprocal chemical synapses are enriched in the *C. elegans* connectome compared to the random networks (Reigl et al., 2004; Varshney et al., 2011). Many triplet motifs contain reciprocal chemical synapses and in order to make a fair comparison while searching for the over-represented triplet motifs in the connectome, we decided to preserve the number of reciprocal chemical synapses in the randomized networks. Additionally, the analysis of connectivity motifs in this study incorporates the information from gap junction and chemical synapse networks independently (see Methods). Thus, we also preserved the likelihood of gap junctions and chemical synapses (Varshney et al., 2011) to a similar ratio as the intact connectome in the randomized matrices.

The algorithm starts with an empty matrix and randomly selects a neuron. Then 4 steps are taken for each neuron. First, it distributes the neuron's outgoing unidirectional connections according to its out-degree to randomly selected neurons as long as their in-degree is not exceeded compared to the intact connectome. Second, it reconnects the neuron's all incoming unidirectional connections now from randomly selected neurons as long as their out-degree is not exceeded compared to the intact connectome. Third, it reconnects all reciprocal connections of that neuron with random neurons that have available unconnected reciprocal connections. Finally, it distributes gap junctions to these newly connected neuron pairs' uni-directionally and reciprocally connected partners according to the corresponding gap junction – chemical synapse likelihood of the intact connectome. If available, the remaining gap junctions for that specific neuron are distributed to random neurons with available degrees.

6.15.4. Rich-club curve preserved randomized networks

For the p value calculation of **Fig.4.17 B**, random matrices that preserve the rich-club curve was used. These random networks preserve all 4 features: degree, reciprocal connection number and gap junction – chemical synapse likelihoods. Further, they also

contain a “synthetic” rich-club organization. This is achieved by using the randomization algorithm described above for two networks separately: rich-club neurons and the rest of the network. Then, these two separately randomized networks are combined together which results in the preservation of inter-connections between the rich-club neurons; thus, the rich-club curve of these randomized networks are similar to the intact connectome.

6.15.5. Partial randomization analysis

For calculating the robustness of the results against variability in the connectome (**Fig.4.17 A**) we generated networks that are partially randomized. For this, we started with the intact connectome and labeled all synapses with different IDs. Next, according to the range of partial randomization, a subpopulation of synapses (e.g. 95%) were preserved. Then, the remaining synapses were randomly distributed across the network. We performed partial randomizations in 1% increments from 1% to 10% and in 5% increments from 10% to 50%.

Next, for every structure-function relationship, r_s values were calculated for all possible partially random networks for 10^5 trials. Then, we calculated the probability where the partially random networks can produce an r_s value greater or equal to the original structure-function relationship (the r_s values shown in **Fig.4.17 A**). The partial randomization range where these p values are below the significance threshold (corrected p values for Bonferroni’s multiple hypothesis test) was annotated as the maximum variability level where the corresponding structure-function relationship holds.

6.16. Connectivity measures

6.16.1. Input similarities

Input similarities were calculated based on the combined network: the sum of chemical synapse and gap junction networks (on unweighted matrices if not stated otherwise). For every pairwise comparison (e.g. neuron A & B) input similarity was calculated as the cosine similarity between the input vectors of A and B (dot product of input vectors divided by their norms) in primary or secondary layer. Input similarity values range between 0 (all available inputs to the neurons are private) and 1 (all available inputs to

the neurons are common). For instance, secondary input similarity for the example pair A-B in **Fig.4.12 D** is 0.7071 whereas the total count of common inputs is 1.

6.16.2. Sum of inverse shortest path calculation

Sum of inverse shortest path was calculated as a directed measure. The shortest path was calculated from both directions and then summed. For instance, for neuronal pairs A&B:

$$1 / \text{shortest path (A} \rightarrow \text{B)} + 1 / \text{shortest path (B} \rightarrow \text{A)}.$$

6.17. *In silico* perturbation screen

6.17.1. Generating perturbed networks

In perturbed networks, the removal of a neuron was done by removing the connections (converting to zero) of the targeted neuron from the matrix. In this way, the total number of neurons within the matrix stays the same. To make it more comparable for the subsequent analyses and neuronal inhibition experiments, the neuron classes were removed as a L-R pair when possible in the perturbation (e.g. AVAL & AVAR are both removed in AVA-perturbation). *In silico* perturbations were performed starting from single neuron class removals and systematically increased up to quadruple neuron class removals. Single and double neuron removals contain all possible combinations of neurons: $n=187$ (187 instead of 279 because L-R pairs are grouped) and $n=1.74 \times 10^4$, respectively. In order to reduce the number of combinations and computation time, motor neurons that belong to DA, DB, AS, DD, VA, VB, VD or VC class are not included in triple and quadruple neuron removals. Triple and quadruple neuron class removals contain all possible combinations of the remaining neurons (113 neurons instead of 187; $n=2.34 \times 10^5$ for triple neuron removal combinations; $n=6.43 \times 10^6$ for quadruple neuron removal combinations).

6.17.2. Graph theoretical measures on perturbed networks

Several graph theoretical measures targeting different network features were calculated on the perturbed networks. These include 3 different measures in **Fig.4.18** with 9 additional ones in **Fig.4.20**. All measures were calculated using the combined connection matrix: sum of the chemical synapse and gap junction networks. Betweenness centrality, eigenvector centrality, characteristic path length, maximum modularity score, clustering coefficient, assortativity coefficient, transitivity and path transitivity were calculated

with the scripts from BCT (Rubinov and Sporns, 2010). Total degree stands for the sum of in- and out-degree of the neurons. Triplet motif count is the sum of all possible 98 motifs occurrences detected by a custom MATLAB script (see Motifs).

In perturbed networks (**Fig.4.18** and **Fig.4.20**) input similarities were calculated in a pairwise manner for all possible pairs in the network (n=38781 pairs for 279 non-pharyngeal neurons) and the mean of the network represents the overall distribution for each perturbation; hence, the neuron classes that have the greatest effect on the measure (e.g. 2° input similarity) will have the lowest mean value after its removal (**Fig.4.18**).

6.17.3. Principal component analysis (PCA) on measures of perturbed networks

The impact of the neuron's removal was calculated by comparing the intact and the perturbed networks. In total we used 12 different graph theoretical measures. For the measures where a single value represents the whole network, we calculated the difference between intact connectome's and perturbed network's value (max modularity score, characteristic path length, triplet motif count, assortativity coefficient, transitivity). For the measures which are neuron specific (degree, betweenness centrality, eigenvector centrality, clustering coefficient) or neuron pair specific (primary and secondary input similarities, path transitivity) the Kolmogorov-Smirnov (KS) distance between the intact connectome and perturbed network's distributions were calculated (the distribution of 279 values or 38781 values represent the network for node-specific and pair-specific measures, respectively). Next, these differences for all perturbed networks (n=6.69x10⁶) were z-scored individually for each measure to be able to compare differences between different measures. Finally, PCA was performed on the z-scored differences.

6.18. Rich club analysis

Rich club coefficient (RCC) curve was calculated as previously described (Towlson et al., 2013) with following modifications. The degree of the neurons was calculated as the sum of chemical synapse degree and gap junction degree. In the normalized RCC curve, the change point (depicted by vertical dashed line in **Fig.4.19**) was chosen as the threshold where a sudden increase is observed. According to this threshold following neurons were classified as the network hubs in this study (sorted by their total degree): AVAR, AVAL, AVBL, AVBR, PVCR, PVCL, AVDR, DVA, AVEL, AVER, AVDL,

AIBR, RIAR, RIBL, AIBL, HSNR, RIAL, RIH, RIMR, AVJL and AVKL. The remaining L or R counterparts of 5 neuron classes: RIBR, RIML, AVJR, HSNL and AVKR were also classified as network hubs in the *in silico* perturbation screen due to neuron classes being removed from the network as L-R pairs in this analysis (see Methods).

6.19. Connectivity motifs

In both dyad and triplet motif detections, we targeted “structural motifs” (Sporns and Kötter, 2004) and searched for the exact connectivity pattern within triplets where every unique neuron triplet can have a single motif ID. For instance, if neuron A,B,C is connected with motif ID#3, and neuron D,E,F is connected with motif ID#4, and motif ID#3 is a subset of motif ID#4 (**Fig.4.10**), we counted the occurrence of motif ID#3 and #4 both as 1 (as opposed to counting motif ID#3 for twice and motif ID#4 for once). This approach was implemented to avoid counting the same circuit over and over again which might result in highly inflated motif statistics.

6.19.1. Dyad connectivity motifs

Dyad connectivity motifs were detected within the connectome by incorporating the information in both chemical synapse and gap junction networks.

6.19.2. Triplet connectivity motifs

6.19.2.1. Detection of motifs

Triplet connectivity motifs were detected within the connectome using a custom MATLAB code. The algorithm treats chemical synapse and gap junction networks separately but unlike previous studies (Cook et al., 2019; Reigl et al., 2004; Varshney et al., 2011), it incorporates the two information between triplets of neurons. With this approach the total permutation of triplet motifs increased to 98 (it was 2 permutations for gap junctions and 13 permutations for chemical synapses if the networks are considered alone). The full list of 98 motifs is visible in **Fig.4.10**. Furthermore, within the triplet motifs there can be several neuronal pair configurations (1, 2 or 3 per motif according to the symmetry level) and in 98 triplet motifs the total number of neuronal pair configuration is 259; thus, we refer to these 259 as different motifs when considering

pairwise correlations (e.g. in **Fig.4.9 A**, A-C is a neuronal pair configuration within the motif, A-B and B-C configurations also exist within the same motif).

6.19.2.2. Classifying significant motifs

We tested the ability of triplet motifs to influence functional interactions of neurons by comparing it to a control group. For each configuration of neuronal pairs within the triplet motifs (259 in total, see Detection of motifs) a control group was assigned. This matched control group contains pairs of neurons with the same dyad connectivity pattern except the members of the analyzed triplet motif. Most neuronal pairs in the functional map are members of multiple motifs and they are also connected via the same motif multiple times. While comparing the motifs versus its control, if the same neuronal pair is present multiple times, these duplicates were removed so that the values taken from the functional map were included only for once for each individual pair. This prevents the artifact of having very skewed distributions stemming from a single neuronal pair, embedded in the same motif many times. The members of the motif and the control group were then compared with a custom shuffle test. The motifs that show significantly high pairwise correlations (p value threshold: 0.05) were classified as “significant motifs”.

An example of a significant motif and its comparison against control group is available in **Fig.4.9 A**. In this example the motif ID#3 from **Fig.4.10** is available together with its matched control group which is non-connected neuron pairs. 12 motifs are not implemented in the *C. elegans* connectome. For the remaining of 247 motifs, 25/247 motifs (10%) were classified as significant (**Fig.4.9 A**) and 136/247 motifs (55%) were classified as non-significant. For 86/247 (35%) motifs our method cannot deduce the motifs ability to influence correlations due to low number of n (≤ 2) either in members of the motif or its control group.

6.19.2.3. Enrichment versus common input

In total, 22 out of 25 triplet motifs that were classified as significant contain a common input to the pair. In order to generalize this feature, we pooled all the motifs that contain a common input. Next, individual motifs were tested against this pooled group of all common input containing motifs (except the motif under analysis) with a custom shuffle

test. 10 different motifs that show significantly high correlation values (p value threshold 0.05) are grouped within the black box in **Fig.4.9 A**.

6.19.2.4. Over-representation of motifs

Here we tested the occurrence of 98 triplet motifs in the *C. elegans* connectome compared to randomized networks. Randomized networks used in this analysis preserve three features: i) degree distribution, ii) reciprocal chemical synapse number and iii) gap junction-chemical synapse likelihood (see Methods). In 10^5 different randomized networks, the occurrences of the motifs were counted. Similar to previous studies (Reigl et al., 2004; Varshney et al., 2011), *single-step min-P based* multiple-hypothesis correction was performed and 0.05 threshold for corrected p values was used for the final classification. Motifs that are over-represented (38/98) and under-represented (10/98) in the connectome are available in **Fig.4.10** as black and green asterisks, respectively.

6.19.2.5. Determining intact, targeted and control groups

In order to exclude the impact of correlation decrease simply due to the inhibition of a neuron, we excluded all pairwise correlation values that belong to the inhibited neuron (or neurons) in the inhibition line datasets.

In the inhibition datasets, we divided the members of significant motifs into two groups according to the condition of the third neuron in that specific configuration of the motif. If this neuron is inhibited via neuronal inhibition tools in that experiment, the members of this motif was added to the “targeted motifs” group. For instance, AIBL-AVBL is a member of a significant motif and AVAL is the third neuron; in this case this pair was added into “targeted motifs” group in AVA-AVE-RIM-PVC inhibition. On the other hand, if the third neuron is not targeted, these neuronal pairs was added to “intact motifs” group. Since neuronal pairs can be members of many motifs, a single pair can be present in both targeted and intact motif groups at the same time. In those special cases, we counted the fraction of instances where it is targeted, if the majority of these cases ($\geq 50\%$) were targeted, then the pair was added to the “targeted motifs” group. If the fraction was $< 50\%$, the pair was excluded from the analysis. Finally, we used a “control group” which only consists neuronal pairs that do not belong to any triplet motif within the connectome.

6.20. Classification of perturbed and control neuronal pairs

In order to assess whether the perturbation of connectivity measures have an impact on the correlation values, we classified neuronal pairs within our inhibition experiments as “perturbed” and “unaffected” (control). Here, the same neuronal pairs’ connectivity measure (e.g. 2° input similarity) was calculated in both intact connectome and perturbed network. Then, the percent change in the perturbed network compared to the intact connectome was calculated. This percent change was calculated for all neuronal pairs within the network (n=38781 pairs) and the distributions were provided for 3 different measures in **Fig.4.36 A-C**. According to these distributions we decided to choose the threshold of 10% for a neuronal pair to be classified as “perturbed” and the rest of the neurons were treated as control pairs or “unaffected”. With the selection of this threshold, 25-45% of neuronal pairs were classified as perturbed for different measures (**Fig.4.36 A-C**, red curves).

According to these classifications, we then grouped the correlation values from the WT and multiple hub inhibition experiments (AVA-AVE-RIM-PVC and AVB-RIB-AIB inhibitions). For the statistical test, the KS distance between WT and inhibition values were measured. Next, we calculated the probability of the same KS distance value to be reached or exceeded in 10^5 trials of degree preserved randomized networks. The p values in **Fig.4.37** were calculated with the 10% threshold. Additionally, we provide the p values calculated with same method but with two different percent change thresholds (20% and 50%) in **Fig.4.36 A-C**, showing that the results are not dependent on this parameter choice.

6.21. Permutation test for global correlation and activity change in WT vs. HisCl datasets

A permutation test was performed to assess the statistical significance of the change in global correlation values and global activity levels between WT and inhibition experiments. First step in this test was to remove the values that belong to the inhibited neuron (or neurons) in both WT and inhibition experiments. For instance, RMS values or all pairwise correlation values of AVAL and AVAR were removed from the WT and HisCl cumulative distributions for the statistical tests of AVA-inhibition experiments. This was done to exclude the impact of activity or correlation decrease simply due to the

inhibition of a neuron. Next, the whole brain imaging datasets (n=6 for WT and n=5 for HisCl datasets) were shuffled and re-grouped into two groups containing 6 vs. 5 datasets and the means of these new groups were calculated. Then, the KS distance of Group#1 and #2 was computed for all permutations of shuffling. Finally, the probability of these KS distances reaching the original WT vs. HisCl KS distance was computed and provided next to the plots in **Fig.4.27 C-D, Fig.4.31 E-H and Fig.4.32 D-F**.

6.22. Custom shuffle test for comparing correlation values

Since the correlation values in our data cannot be assumed to be independent datapoints, which is assumed by standard statistical tests, we applied a custom resampling procedure which is model-free with respect to the underlying data distributions. In this custom shuffle test, the correlation values from both groups were pooled, randomly sampled without repetition with the same number of observations as in the original groups and the difference between the means of these new shuffled groups were calculated in $n=10^4$ trials. Finally, the probability of the distances between means of the shuffled groups reaching the original difference between means was computed and provided next to the plots.

7. References

- Abbott, L.F., Bock, D.D., Callaway, E.M., Denk, W., Dulac, C., Fairhall, A.L., Fiete, I., Harris, K.M., Helmstaedter, M., Jain, V., *et al.* (2020). The Mind of a Mouse. *Cell* *182*, 1372-1376.
- Abbott, L.F., Rajan, K., and Sompolinsky, H. (2011). Interactions between intrinsic and stimulus-evoked activity in recurrent neural networks. *The dynamic brain: an exploration of neuronal variability and its functional significance*, 1-16.
- Ahrens, M.B., Li, J.M., Orger, M.B., Robson, D.N., Schier, A.F., Engert, F., and Portugues, R. (2012). Brain-wide neuronal dynamics during motor adaptation in zebrafish. *Nature* *485*, 471-477.
- Aimon, S., Katsuki, T., Jia, T., Grosenick, L., Broxton, M., Deisseroth, K., Sejnowski, T.J., and Greenspan, R.J. (2019). Fast near-whole-brain imaging in adult *Drosophila* during responses to stimuli and behavior. *PLoS biology* *17*, e2006732 EP -.
- Akerboom, J., Chen, T.-W., Wardill, T.J., Tian, L., Marvin, J.S., Mutlu, S., Calderón, N.C., Esposti, F., Borghuis, B.G., Sun, X.R., *et al.* (2012). Optimization of a GCaMP calcium indicator for neural activity imaging. *The Journal of neuroscience : the official journal of the Society for Neuroscience* *32*, 13819-13840.
- Alkema, M.J., Hunter-Ensor, M., Ringstad, N., and Horvitz, H.R. (2005). Tyramine Functions independently of octopamine in the *Caenorhabditis elegans* nervous system. *Neuron* *46*, 247-260.
- Altun, Z.F., Chen, B., Wang, Z.-W., and Hall, D.H. (2009). High resolution map of *Caenorhabditis elegans* gap junction proteins. *Developmental dynamics : an official publication of the American Association of Anatomists* *238*, 1936-1950.
- Azulay, A., Itskovits, E., and Zaslaver, A. (2016). The *C. elegans* Connectome Consists of Homogenous Circuits with Defined Functional Roles. *PLoS Computational Biology* *12*, e1005021.
- Barabasi, A., and Albert, R. (1999). Wiring cost and topological participation of the mousebrain connectome. *Science* *286*, 509-512.
- Barabási, D.L., and Barabási, A.-L. (2020). A Genetic Model of the Connectome. *Neuron* *105*, 435-445.e435.
- Bargmann, C.I. (1998). Neurobiology of the *Caenorhabditis elegans* genome. *Science* *282*, 2028-2033.
- Bartho, P., Curto, C., Luczak, A., Marguet, S.L., and Harris, K.D. (2009). Population coding of tone stimuli in auditory cortex: dynamic rate vector analysis. *The European journal of neuroscience* *30*, 1767-1778.
- Bassett, D.S., and Bullmore, E. (2006). Small-world brain networks. *Neuroscientist* *12*, 512-523.
- Bassett, D.S., and Sporns, O. (2017). Network neuroscience. *Nature neuroscience* *20*, 353-364.
- Bentley, B., Branicky, R., Barnes, C.L., Bullmore, E.T., Vértes, P.E., and Schafer, W.R. (2016). The multilayer connectome of *Caenorhabditis elegans*. *arXivorg q-bio.NC*, e1005283.
- Bhattacharya, A., Aghayeva, U., Berghoff, E.G., and Hobert, O. (2019). Plasticity of the Electrical Connectome of *C. elegans*. *Cell* *176*, 1174-1189.e1116.
- Bock, N.A., Hashim, E., Kocharyan, A., and Silva, A.C. (2011). Visualizing myeloarchitecture with magnetic resonance imaging in primates. *Annals of the New York Academy of Sciences* *1225 Suppl 1*, E171-181.

- Bonifazi, P., Goldin, M., Picardo, M.A., Jorquera, I., Cattani, A., Bianconi, G., Represa, A., Ben-Ari, Y., and Cossart, R. (2009). GABAergic hub neurons orchestrate synchrony in developing hippocampal networks. *Science* 326, 1419-1424.
- Briggman, K.L., Abarbanel, H.D.I., and Kristan, W.B. (2005). Optical imaging of neuronal populations during decision-making. *Science* 307, 896-901.
- Briggman, K.L., and Bock, D.D. (2012). Volume electron microscopy for neuronal circuit reconstruction. *Current opinion in neurobiology* 22, 154-161.
- Brody, C. (1999). Correlations without synchrony. *Neural computation* 11, 1537-1551.
- Brownlee, D.J., and Fairweather, I. (1999). Exploring the neurotransmitter labyrinth in nematodes. *Trends in neurosciences* 22, 16-24.
- Bruno, A.M., Frost, W.N., and Humphries, M.D. (2017). A spiral attractor network drives rhythmic locomotion. *eLife* 6, 471.
- Burnstock, G. (2004). Cotransmission. *Current opinion in pharmacology* 4, 47-52.
- Cáceres, I.d.C., Valmas, N., Hilliard, M.A., and Lu, H. (2012). Laterally orienting *C. elegans* using geometry at microscale for high-throughput visual screens in neurodegeneration and neuronal development studies. *PloS one* 7, e35037.
- Chai, L.R., Khambhati, A.N., Ciric, R., Moore, T.M., Gur, R.C., Gur, R.E., Satterthwaite, T.D., and Bassett, D.S. (2017). Evolution of brain network dynamics in neurodevelopment. *Network neuroscience (Cambridge, Mass)* 1, 14-30.
- Chalasan, S.H., Chronis, N., Tsunozaki, M., Gray, J.M., Ramot, D., Goodman, M.B., and Bargmann, C.I. (2007). Dissecting a circuit for olfactory behaviour in *Caenorhabditis elegans*. *Nature* 450, 63-70.
- Chalasan, S.H., Kato, S., Albrecht, D.R., Nakagawa, T., Abbott, L.F., and Bargmann, C.I. (2010). Neuropeptide feedback modifies odor-evoked dynamics in *Caenorhabditis elegans* olfactory neurons. *Nature neuroscience* 13, 615-621.
- Chalfie, M., Sulston, J.E., White, J.G., Southgate, E., Thomson, J.N., and Brenner, S. (1985). The neural circuit for touch sensitivity in *Caenorhabditis elegans*. *The Journal of neuroscience : the official journal of the Society for Neuroscience* 5, 956-964.
- Chartrand, R. (2011). Numerical Differentiation of Noisy, Nonsmooth Data. *ISRN Applied Mathematics* 2011, 1-11.
- Chase, D.L., and Koelle, M.R. (2007). Biogenic amine neurotransmitters in *C. elegans*. *WormBook : the online review of C elegans biology*, 1-15.
- Chen, T.-W., Wardill, T.J., Sun, Y., Pulver, S.R., Renninger, S.L., Baohan, A., Schreiter, E.R., Kerr, R.A., Orger, M.B., Jayaraman, V., *et al.* (2013). Ultrasensitive fluorescent proteins for imaging neuronal activity. *Nature* 499, 295-300.
- Chklovskii, D.B., Schikorski, T., and Stevens, C.F. (2002). Wiring optimization in cortical circuits. *Neuron* 34, 341-347.
- Churchland, M.M., Cunningham, J.P., Kaufman, M.T., Foster, J.D., Nuyujukian, P., Ryu, S.I., and Shenoy, K.V. (2012). Neural population dynamics during reaching. *Nature* 487, 51-56.
- Cochella, L., and Hobert, O. (2012). Embryonic priming of a miRNA locus predetermines postmitotic neuronal left/right asymmetry in *C. elegans*. *Cell* 151, 1229-1242.
- Colizza, V., Flammini, A., Serrano, M.A., and Vespignani, A. (2006). Detecting rich-club ordering in complex networks. *Nature Physics* 2, 110-115.
- Cook, S.J., Jarrell, T.A., Brittin, C.A., Wang, Y., Bloniarz, A.E., Yakovlev, M.A., Nguyen, K.C.Q., Tang, L.T.H., Bayer, E.A., Duerr, J.S., *et al.* (2019). Whole-animal connectomes of both *Caenorhabditis elegans* sexes. *Nature* 571, 63-71.

- Cossell, L., Iacaruso, M.F., Muir, D.R., Houlton, R., Sader, E.N., Ko, H., Hofer, S.B., and Mrsic-Flogel, T.D. (2015). Functional organization of excitatory synaptic strength in primary visual cortex. *Nature* 518, 399-403.
- Cover, T.M., and Thomas, J.A. (2006). *Elements of Information Theory*, 2nd Edition edn (New York: Wiley-Interscience).
- Curto, C., and Morrison, K. (2019). Relating network connectivity to dynamics: opportunities and challenges for theoretical neuroscience. *Current opinion in neurobiology* 58, 11-20.
- Dasgupta, S., Stevens, C.F., and Navlakha, S. (2017). A neural algorithm for a fundamental computing problem. *Science* 358, 793-796.
- De Bono, M., and Bargmann, C.I. (1998). Natural variation in a neuropeptide Y receptor homolog modifies social behavior and food response in *C. elegans*. *Cell* 94, 679-689.
- de Reus, M.A., and van den Heuvel, M.P. (2013). Rich club organization and intermodule communication in the cat connectome. *The Journal of neuroscience : the official journal of the Society for Neuroscience* 33, 12929-12939.
- de Reus, M.A., and van den Heuvel, M.P. (2014). Simulated rich club lesioning in brain networks: a scaffold for communication and integration? *Frontiers in human neuroscience* 8, 647.
- De Robertis, E. (1959). Submicroscopic morphology of the synapse. *Int Rev Cytol* 8, 61-96.
- Edwards, S.L., Charlie, N.K., Milfort, M.C., Brown, B.S., Gravlin, C.N., Knecht, J.E., and Miller, K.G. (2008). A novel molecular solution for ultraviolet light detection in *Caenorhabditis elegans*. *PLoS biology* 6, e198.
- Eichler, K., Li, F., Litwin-Kumar, A., Park, Y., Andrade, I., Schneider-Mizell, C.M., Saumweber, T., Huser, A., Eschbach, C., Gerber, B., *et al.* (2017). The complete connectome of a learning and memory centre in an insect brain. *Nature* 548, 175-182.
- Eschbach, C., Fushiki, A., Winding, M., Schneider-Mizell, C.M., Shao, M., Arruda, R., Eichler, K., Valdes-Aleman, J., Ohyama, T., Thum, A.S., *et al.* (2020). Recurrent architecture for adaptive regulation of learning in the insect brain. *Nature neuroscience* 23, 544-555.
- Fei, Y.-J., Romero, M.F., Krause, M., Liu, J.-C., Huang, W., Ganapathy, V., and Leibach, F.H. (2000). A novel H⁺-coupled oligopeptide transporter (OPT3) from *Caenorhabditis elegans* with a predominant function as a H⁺ channel and an exclusive expression in neurons. *Journal of Biological Chemistry* 275, 9563-9571.
- Fenyves, B.G., Szilágyi, G.S., Vassy, Z., Söti, C., and Csermely, P. (2020). Synaptic polarity and sign-balance prediction using gene expression data in the *Caenorhabditis elegans* chemical synapse neuronal connectome network. *PLoS Computational Biology* 16, e1007974 EP -.
- Ferrarini, L., Veer, I.M., Baerends, E., van Tol, M.-J., Renken, R.J., van der Wee, N.J.A., Veltman, D.J., Aleman, A., Zitman, F.G., Penninx, B.W.J.H., *et al.* (2009). Hierarchical Functional Modularity in the Resting-State Human Brain. *Human brain mapping* 30, 2220-2231.
- Freeman, L.C. (1978). Centrality in social networks conceptual clarification. *Social Networks* 1, 215-239.
- Gal, E., London, M., Globerson, A., Ramaswamy, S., Reimann, M.W., Muller, E., Markram, H., and Segev, I. (2017). Rich cell-type-specific network topology in neocortical microcircuitry. *Nature neuroscience* 20, 1004-1013.

- Gendrel, M., Atlas, E.G., and Hobert, O. (2016). A cellular and regulatory map of the GABAergic nervous system of *C. elegans*. *eLife* 5.
- Girvan, M., and Newman, M.E.J. (2002). Community structure in social and biological networks. *Proc Natl Acad Sci USA* 99, 7821.
- Gisselmann, G., Pusch, H., Hovemann, B.T., and Hatt, H. (2002). Two cDNAs coding for histamine-gated ion channels in *D. melanogaster*. *Nature neuroscience* 5, 11-12.
- Gong, J., Yuan, Y., Ward, A., Kang, L., Zhang, B., Wu, Z., Peng, J., Feng, Z., Liu, J., and Xu, X.Z.S. (2016). The *C. elegans* Taste Receptor Homolog LITE-1 Is a Photoreceptor. *Cell* 167, 1252-1263.e1210.
- Goodman, M.B., Hall, D.H., Avery, L., and Lockery, S.R. (1998). Active currents regulate sensitivity and dynamic range in *C. elegans* neurons. *Neuron* 20, 763-772.
- Gordus, A., Pokala, N., Levy, S., Flavell, S.W., and Bargmann, C.I. (2015). Feedback from network states generates variability in a probabilistic olfactory circuit. *Cell* 161, 215-227.
- Goulas, A., Bastiani, M., Bezgin, G., Uylings, H.B.M., Roebroek, A., and Stiers, P. (2014). Comparative analysis of the macroscale structural connectivity in the macaque and human brain. *PLoS Computational Biology* 10, e1003529.
- Gray, J.M., Hill, J.J., and Bargmann, C.I. (2005). A circuit for navigation in *Caenorhabditis elegans*. *Proceedings of the National Academy of Sciences of the United States of America* 102, 3184-3191.
- Gulyás, A.I., Megías, M., Emri, Z., and Freund, T.F. (1999). Total Number and Ratio of Excitatory and Inhibitory Synapses Converging onto Single Interneurons of Different Types in the CA1 Area of the Rat Hippocampus. *The Journal of neuroscience : the official journal of the Society for Neuroscience* 19, 10082.
- Gurnani, H., and Silver, R.A. (2021). Multidimensional population activity in an electrically coupled inhibitory circuit in the cerebellar cortex. *Neuron* 109, 1739-1753.e1738.
- Haeusler, S., Schuch, K., and Maass, W. (2009). Motif distribution, dynamical properties, and computational performance of two data-based cortical microcircuit templates. *Journal of Physiology - Paris* 103, 73-87.
- Hagmann, P., Cammoun, L., Gigandet, X., Meuli, R., Honey, C.J., Wedeen, V.J., and Sporns, O. (2008). Mapping the structural core of human cerebral cortex. *PLoS biology* 6, e159.
- Hall, D.H. (2017). Gap junctions in *C. elegans*: Their roles in behavior and development. *Developmental neurobiology* 77, 587-596.
- Hallinen, K.M., Dempsey, R., Scholz, M., Yu, X., Linder, A., Randi, F., Sharma, A.K., Shaevitz, J.W., and Leifer, A.M. (2021). Decoding locomotion from population neural activity in moving *C. elegans*. *Elife* 10.
- Harriger, L., van den Heuvel, M.P., and Sporns, O. (2012). Rich club organization of macaque cerebral cortex and its role in network communication. *PloS one* 7, e46497.
- Helmstaedter, M., Briggman, K.L., Turaga, S.C., Jain, V., Seung, H.S., and Denk, W. (2013). Connectomic reconstruction of the inner plexiform layer in the mouse retina. *Nature* 500, 168-174.
- Hildebrand, D.G.C., Cicconet, M., Torres, R.M., Choi, W., Quan, T.M., Moon, J., Wetzel, A.W., Scott Champion, A., Graham, B.J., Randlett, O., *et al.* (2017). Whole-brain serial-section electron microscopy in larval zebrafish. *Nature* 545, 345-349.
- Hobert, O. (2013). The neuronal genome of *Caenorhabditis elegans*. *WormBook : the online review of C elegans biology*, 1-106.

- Hobert, O., Johnston, R.J., and Chang, S. (2002). Left-right asymmetry in the nervous system: the *Caenorhabditis elegans* model. *Nature reviews Neuroscience* 3, 629-640.
- Honey, C.J., Kötter, R., Breakspear, M., and Sporns, O. (2007). Network structure of cerebral cortex shapes functional connectivity on multiple time scales. *Proceedings of the National Academy of Sciences of the United States of America* 104, 10240-10245.
- Hong, R.L., Riebesell, M., Bumbarger, D.J., Cook, S.J., Carstensen, H.R., Sarpolaki, T., Cochella, L., Castrejon, J., Moreno, E., Sieriebriennikov, B., *et al.* (2019). Evolution of neuronal anatomy and circuitry in two highly divergent nematode species. *eLife* 8.
- Huang, L., Kebschull, J.M., Fürth, D., Musall, S., Kaufman, M.T., Churchland, A.K., and Zador, A.M. (2020). BRICseq Bridges Brain-wide Interregional Connectivity to Neural Activity and Gene Expression in Single Animals. *Cell* 182, 177-188.e127.
- Humphries, M.D., and Gurney, K. (2008). Network ‘Small-World-Ness’: A Quantitative Method for Determining Canonical Network Equivalence. *PLOS ONE* 3, e0002051.
- Husson, S.J., Costa, W.S., Wabnig, S., Stirman, J.N., Watson, J.D., Spencer, W.C., Akerboom, J., Looger, L.L., Treinin, M., Miller, D.M., *et al.* (2012). Optogenetic analysis of a nociceptor neuron and network reveals ion channels acting downstream of primary sensors. *Current biology* : CB 22, 743-752.
- Ince, R.A.A., Giordano, B.L., Kayser, C., Rousselet, G.A., Gross, J., and Schyns, P.G. (2017). A statistical framework for neuroimaging data analysis based on mutual information estimated via a gaussian copula. *Human brain mapping* 38, 1541-1573.
- Jarrell, T.A., Wang, Y., Bloniarz, A.E., Brittin, C.A., Xu, M., Thomson, J.N., Albertson, D.G., Hall, D.H., and Emmons, S.W. (2012). The connectome of a decision-making neural network. *Science* 337, 437-444.
- Jiang, J., Su, Y., Zhang, R., Li, H., Tao, L., and Liu, Q. (2021). *C. elegans* enteric motor neurons fire synchronized action potentials underlying the defecation motor program. *bioRxiv*, 2021.2008.2025.457687.
- Kaplan, H.S., Nichols, A.L.A., and Zimmer, M. (2018). Sensorimotor integration in *Caenorhabditis elegans*: a reappraisal towards dynamic and distributed computations. *Philosophical transactions of the Royal Society of London Series B, Biological sciences* 373.
- Kaplan, H.S., Salazar Thula, O., Khoss, N., and Zimmer, M. (2020). Nested Neuronal Dynamics Orchestrate a Behavioral Hierarchy across Timescales. *Neuron* 105, 562-576.e569.
- Kato, S., Kaplan, H.S., Schrödel, T., Skora, S., Lindsay, T.H., Yemini, E., Lockery, S., and Zimmer, M. (2015). Global brain dynamics embed the motor command sequence of *Caenorhabditis elegans*. *Cell* 163, 656-669.
- Katz, M., Corson, F., Iwanir, S., Biron, D., and Shaham, S. (2018). Glia Modulate a Neuronal Circuit for Locomotion Suppression during Sleep in *C. elegans*. *Cell reports* 22, 2575-2583.
- Kawano, T., Po, M.D., Gao, S., Leung, G., Ryu, W.S., and Zhen, M. (2011). An imbalancing act: gap junctions reduce the backward motor circuit activity to bias *C. elegans* for forward locomotion. *Neuron* 72, 572-586.
- Kocabas, A., Shen, C.-H., Guo, Z.V., and Ramanathan, S. (2012). Controlling interneuron activity in *Caenorhabditis elegans* to evoke chemotactic behaviour. *Nature* 490, 273-277.

- Kopell, N.J., Gritton, H.J., Whittington, M.A., and Kramer, M.A. (2014). Beyond the connectome: the dynamo. *Neuron* 83, 1319-1328.
- Laurent, P., Soltesz, Z., Nelson, G.M., Chen, C., Arellano-Carbajal, F., Levy, E., and de Bono, M. (2015). Decoding a neural circuit controlling global animal state in *C. elegans*. *eLife* 4.
- Leicht, E.A., and Newman, M.E.J. (2008). Community structure in directed networks. *Physical review letters* 100, 118703.
- Li, C., and Kim, K. (2008). Neuropeptides. *WormBook : the online review of C elegans biology*, 1-36.
- Li, W., Kang, L., Piggott, B.J., Feng, Z., and Xu, X.Z.S. (2011). The neural circuits and sensory channels mediating harsh touch sensation in *Caenorhabditis elegans*. *Nature communications* 2, 315-319.
- Li, Z., Liu, J., Zheng, M., and Xu, X.Z.S. (2014). Encoding of both analog- and digital-like behavioral outputs by one *C. elegans* interneuron. *Cell* 159, 751-765.
- Li, Z., Zhou, J., Wani, K.A., Yu, T., Ronan, E.A., Liu, J., and Xu, X.Z. (2020). A *C. elegans* neuron both promotes and suppresses motor behavior to fine tune motor output [preprint].
- Lichtman, J.W., and Denk, W. (2011). The big and the small: challenges of imaging the brain's circuits. *Science* 334, 618-623.
- Lindsay, T.H., Thiele, T.R., and Lockery, S.R. (2011). Optogenetic analysis of synaptic transmission in the central nervous system of the nematode *Caenorhabditis elegans*. *Nature communications* 2, 306-309.
- Liu, J., Ward, A., Gao, J., Dong, Y., Nishio, N., Inada, H., Kang, L., Yu, Y., Ma, D., Xu, T., *et al.* (2010). *C. elegans* phototransduction requires a G protein-dependent cGMP pathway and a taste receptor homolog. *Nature neuroscience* 13, 715-722.
- Liu, P., Chen, B., Altun, Z.F., Gross, M.J., Shan, A., Schuman, B., Hall, D.H., and Wang, Z.-W. (2013). Six innexins contribute to electrical coupling of *C. elegans* body-wall muscle. *PLoS one* 8, e76877.
- Liu, P., Chen, B., Mailler, R., and Wang, Z.-W. (2017). Antidromic-rectifying gap junctions amplify chemical transmission at functionally mixed electrical-chemical synapses. *Nature Communications* 8, 14818.
- Liu, Q., Kidd, P.B., Dobosiewicz, M., and Bargmann, C.I. (2018). *C. elegans* AWA Olfactory Neurons Fire Calcium-Mediated All-or-None Action Potentials. *Cell* 175, 57-70.e17.
- Macosko, E.Z., Pokala, N., Feinberg, E.H., Chalasani, S.H., Butcher, R.A., Clardy, J., and Bargmann, C.I. (2009). A hub-and-spoke circuit drives pheromone attraction and social behaviour in *C. elegans*. *Nature* 458, 1171-1175.
- Mante, V., Sussillo, D., Shenoy, K.V., and Newsome, W.T. (2013). Context-dependent computation by recurrent dynamics in prefrontal cortex. *Nature* 503, 78-84.
- Marder, E. (2009). Electrical synapses: rectification demystified. *Current biology : CB* 19, R34-35.
- Marom, S., and Shahaf, G. (2002). Development, learning and memory in large random networks of cortical neurons: lessons beyond anatomy. *Quarterly Reviews of Biophysics* 35, 63-87.
- McGrath, P.T., Rockman, M.V., Zimmer, M., Jang, H., Macosko, E.Z., Kruglyak, L., and Bargmann, C.I. (2009). Quantitative mapping of a digenic behavioral trait implicates globin variation in *C. elegans* sensory behaviors. *Neuron* 61, 692-699.
- Mellem, J.E., Brockie, P.J., Madsen, D.M., and Maricq, A.V. (2008). Action potentials contribute to neuronal signaling in *C. elegans*. *Nature neuroscience* 11, 865-867.

- Milo, R., Shen-Orr, S., Itzkovitz, S., Kashtan, N., Chklovskii, D., and Alon, U. (2002). Network motifs: simple building blocks of complex networks. *Science* 298, 824-827.
- Mòdol, L., Sousa, V.H., Malvache, A., Tressard, T., Baude, A., and Cossart, R. (2017). Spatial Embryonic Origin Delineates GABAergic Hub Neurons Driving Network Dynamics in the Developing Entorhinal Cortex. *Cerebral cortex* (New York, NY : 1991) 27, 4649-4661.
- Morone, F., and Makse, H.A. (2019). Symmetry group factorization reveals the structure-function relation in the neural connectome of *Caenorhabditis elegans*. *Nature communications* 10, 4961-4913.
- Motta, A., Berning, M., Boergens, K.M., Staffler, B., Beining, M., Loomba, S., Hennig, P., Wissler, H., and Helmstaedter, M. (2019). Dense connectomic reconstruction in layer 4 of the somatosensory cortex. *Science* 366.
- Musall, S., Kaufman, M.T., Juavinett, A.L., Gluf, S., and Churchland, A.K. (2019). Single-trial neural dynamics are dominated by richly varied movements. *Nature neuroscience* 22, 1677-1686.
- Nakai, J., Ohkura, M., and Imoto, K. (2001). A high signal-to-noise Ca(2+) probe composed of a single green fluorescent protein. *Nature biotechnology* 19, 137-141.
- Narayan, A., Laurent, G., and Sternberg, P.W. (2011). Transfer characteristics of a thermosensory synapse in *Caenorhabditis elegans*. *Proceedings of the National Academy of Sciences of the United States of America* 108, 9667-9672.
- Newman, M.E.J. (2002). Assortative mixing in networks. *Physical review letters* 89, 208701.
- Newman, M.E.J. (2003). The Structure and Function of Complex Networks. *SIAM Rev* 45, 167-256.
- Newman, M.E.J. (2004). Detecting community structure in networks. *The European Physical Journal B* 38, 321-330.
- Nguyen, J.P., Shipley, F.B., Linder, A.N., Plummer, G.S., Liu, M., Setru, S.U., Shaevitz, J.W., and Leifer, A.M. (2016). Whole-brain calcium imaging with cellular resolution in freely behaving *Caenorhabditis elegans*. *Proceedings of the National Academy of Sciences of the United States of America* 113, E1074-1081.
- Nichols, A.L.A., Eichler, T., Latham, R., and Zimmer, M. (2017). A global brain state underlies *C. elegans* sleep behavior. *Science* 356.
- Nigam, S., Shimono, M., Ito, S., Yeh, F.-C., Timme, N., Myroshnychenko, M., Lapiush, C.C., Tosi, Z., Hottowy, P., Smith, W.C., *et al.* (2016). Rich-Club Organization in Effective Connectivity among Cortical Neurons. *The Journal of neuroscience : the official journal of the Society for Neuroscience* 36, 670-684.
- Owen, A.B., and Perry, P.O. (2009). Bi-cross-validation of the SVD and the nonnegative matrix factorization. *The Annals of Applied Statistics* 3, 564-594, 531.
- Pan, R.K., Chatterjee, N., and Sinha, S. (2010). Mesoscopic organization reveals the constraints governing *Caenorhabditis elegans* nervous system. *PloS one* 5, e9240.
- Pecora, L.M., Sorrentino, F., Hagerstrom, A.M., Murphy, T.E., and Roy, R. (2014). Cluster synchronization and isolated desynchronization in complex networks with symmetries. *Nature communications* 5, 1-8.
- Pereira, L., Kratsios, P., Serrano-Saiz, E., and Elife, H.S. (2015). A cellular and regulatory map of the cholinergic nervous system of *C. elegans*. *elifesciences.org*.
- Perin, R., Berger, T.K., and Markram, H. (2011). A synaptic organizing principle for cortical neuronal groups. *Proceedings of the National Academy of Sciences of the United States of America* 108, 5419-5424.

- Pirri, J.K., McPherson, A.D., Donnelly, J.L., Francis, M.M., and Alkema, M.J. (2009). A tyramine-gated chloride channel coordinates distinct motor programs of a *Caenorhabditis elegans* escape response. *Neuron* 62, 526-538.
- Pokala, N., Liu, Q., Gordus, A., and Bargmann, C.I. (2014). Inducible and titratable silencing of *Caenorhabditis elegans* neurons in vivo with histamine-gated chloride channels. *Proceedings of the National Academy of Sciences of the United States of America* 111, 2770-2775.
- Qian, J., Hintze, A., and One, C.A.P. (2011). Colored motifs reveal computational building blocks in the *C. elegans* brain. *journal.plosorg*.
- Rakowski, F., Srinivasan, J., Sternberg, P.W., and Karbowski, J. (2013). Synaptic polarity of the interneuron circuit controlling *C. elegans* locomotion. *Frontiers in computational neuroscience* 7, 128.
- Ramot, D., Johnson, B.E., Berry, T.L., Carnell, L., and Goodman, M.B. (2008). The Parallel Worm Tracker: a platform for measuring average speed and drug-induced paralysis in nematodes. *PloS one* 3, e2208.
- Randel, N., Shahidi, R., Verasztó, C., Bezares-Calderón, L.A., Schmidt, S., and Jékely, G. (2015). Inter-individual stereotypy of the *Platynereis* larval visual connectome. *eLife* 4, e08069.
- Reigl, M., Alon, U., and Chklovskii, D.B. (2004). Search for computational modules in the *C. elegans* brain. *BMC biology* 2, 25.
- Rice, J.A. (2006). *Mathematical Statistics and Data Analysis*, 3rd edition edn (Belmont, CA: Duxbury Press).
- Rieubland, S., Roth, A., and Häusser, M. (2014). Structured Connectivity in Cerebellar Inhibitory Networks. *Neuron* 81, 913-929.
- Rubinov, M., and Sporns, O. (2010). Complex network measures of brain connectivity: uses and interpretations. *NeuroImage* 52, 1059-1069.
- Rubinov, M., Ypma, R.J.F., Watson, C., and Bullmore, E.T. (2015). Wiring cost and topological participation of the mousebrain connectome. *Proceedings of the National Academy of Sciences of the United States of America* 112, 10032-10037.
- Ruijtenberg, S., and van den Heuvel, S. (2015). G1/S Inhibitors and the SWI/SNF Complex Control Cell-Cycle Exit during Muscle Differentiation. *Cell* 162, 300-313.
- Ryan, K., Lu, Z., and Meinertzhagen, I.A. (2016). The CNS connectome of a tadpole larva of *Ciona intestinalis* (L.) highlights sidedness in the brain of a chordate sibling. *eLife* 5.
- Salkoff, D.B., Zagha, E., McCarthy, E., and McCormick, D.A. (2020). Movement and Performance Explain Widespread Cortical Activity in a Visual Detection Task. *Cerebral cortex* (New York, NY : 1991) 30, 421-437.
- Schmitt, C., Schultheis, C., Pokala, N., Husson, S.J., Liewald, J.F., Bargmann, C.I., and Gottschalk, A. (2012). Specific expression of channelrhodopsin-2 in single neurons of *Caenorhabditis elegans*. *PloS one* 7, e43164.
- Schneider-Mizell, C.M., Gerhard, S., Longair, M., Kazimiers, T., Li, F., Zwart, M.F., Champion, A., Midgley, F.M., Fetter, R.D., Saalfeld, S., *et al.* (2016). Quantitative neuroanatomy for connectomics in *Drosophila*. *eLife* 5.
- Schrödel, T., Prevedel, R., Aumayr, K., Zimmer, M., and Vaziri, A. (2013). Brain-wide 3D imaging of neuronal activity in *Caenorhabditis elegans* with sculpted light. *Nature methods* 10, 1013-1020.
- Serrano-Saiz, E., Poole, R.J., Felton, T., Zhang, F., De La Cruz, E.D., and Hobert, O. (2013). Modular control of glutamatergic neuronal identity in *C. elegans* by distinct homeodomain proteins. *Cell* 155, 659-673.

- Shanahan, M. (2012). The brain's connective core and its role in animal cognition. *Philosophical transactions of the Royal Society of London Series B, Biological sciences* 367, 2704-2714.
- Shannon, C.E. (1948). A Mathematical Theory of Communication. *Bell System Technical Journal* 27, 379-423.
- Shih, C.-T., Sporns, O., Yuan, S.-L., Su, T.-S., Lin, Y.-J., Chuang, C.-C., Wang, T.-Y., Lo, C.-C., Greenspan, R.J., and Chiang, A.-S. (2015). Connectomics-Based Analysis of Information Flow in the Drosophila Brain. *Current Biology* 25, 1249-1258.
- Shine, J.M., Breakspear, M., Bell, P.T., Ehgoetz Martens, K.A., Shine, R., Koyejo, O., Sporns, O., and Poldrack, R.A. (2019). Human cognition involves the dynamic integration of neural activity and neuromodulatory systems. *Nature neuroscience* 22, 289-296.
- Skora, S., Mende, F., and Zimmer, M. (2018). Energy Scarcity Promotes a Brain-wide Sleep State Modulated by Insulin Signaling in *C. elegans*. *Cell reports* 22, 953-966.
- Sohal, V.S., Zhang, F., Yizhar, O., and Deisseroth, K. (2009). Parvalbumin neurons and gamma rhythms enhance cortical circuit performance. *Nature* 459, 698-702.
- Sohn, Y., Choi, M.-K., Ahn, Y.-Y., Lee, J., and Jeong, J. (2011). Topological cluster analysis reveals the systemic organization of the Caenorhabditis elegans connectome. *PLoS Computational Biology* 7, e1001139.
- Song, S., Sjöström, P.J., Reigl, M., Nelson, S., and Chklovskii, D.B. (2005). Highly nonrandom features of synaptic connectivity in local cortical circuits. *PLoS biology* 3, e68.
- Sporns, O., and Kötter, R. (2004). Motifs in brain networks. *PLoS biology* 2, e369.
- Sporns, O., Tononi, G., and Kötter, R. (2005). The human connectome: A structural description of the human brain. *PLoS Computational Biology* 1, e42.
- Starich, T.A., Hall, D.H., and Greenstein, D. (2014). Two classes of gap junction channels mediate soma-germline interactions essential for germline proliferation and gametogenesis in *Caenorhabditis elegans*. *Genetics* 198, 1127-1153.
- Starich, T.A., Lee, R.Y., Panzarella, C., Avery, L., and Shaw, J.E. (1996). eat-5 and unc-7 represent a multigene family in *Caenorhabditis elegans* involved in cell-cell coupling. *The Journal of cell biology* 134, 537-548.
- Stopfer, M., Jayaraman, V., and Laurent, G. (2003). Intensity versus identity coding in an olfactory system. *Neuron* 39, 991-1004.
- Stringer, C., Pachitariu, M., Steinmetz, N., Reddy, C.B., Carandini, M., and Harris, K.D. (2019). Spontaneous behaviors drive multidimensional, brainwide activity. *Science* 364, 255.
- Susoy, V., Hung, W., Witvliet, D., Whitener, J.E., Wu, M., Park, C.F., Graham, B.J., Zhen, M., Venkatachalam, V., and Samuel, A.D.T. (2021). Natural sensory context drives diverse brain-wide activity during *C. elegans* mating. *Cell* 184, 5122-5137.e5117.
- Takemura, S.-y., Aso, Y., Hige, T., Wong, A., Lu, Z., Xu, C.S., Rivlin, P.K., Hess, H., Zhao, T., Parag, T., *et al.* (2017). A connectome of a learning and memory center in the adult *Drosophila* brain. *eLife* 6, 5643.
- Takemura, S.-y., Bharioke, A., Lu, Z., Nern, A., Vitaladevuni, S., Rivlin, P.K., Katz, W.T., Olbris, D.J., Plaza, S.M., Winston, P., *et al.* (2013). A visual motion detection circuit suggested by *Drosophila* connectomics. *Nature* 500, 175-181.
- Tian, L., Hires, S.A., Mao, T., Huber, D., Chiappe, M.E., Chalasani, S.H., Petreanu, L., Akerboom, J., McKinney, S.A., Schreiter, E.R., *et al.* (2009). Imaging neural

- activity in worms, flies and mice with improved GCaMP calcium indicators. *Nature methods* 6, 875-881.
- Timme, N.M., and Lapish, C. (2018). A Tutorial for Information Theory in Neuroscience. *eNeuro* 5.
- Tononi, G., Sporns, O., and Edelman, G.M. (1994). A measure for brain complexity: relating functional segregation and integration in the nervous system. *Proceedings of the National Academy of Sciences of the United States of America* 91, 5033-5037.
- Towlson, E.K., Vértés, P.E., Ahnert, S.E., Schafer, W.R., and Bullmore, E.T. (2013). The rich club of the *C. elegans* neuronal connectome. *The Journal of neuroscience : the official journal of the Society for Neuroscience* 33, 6380-6387.
- Treinin, M., Gillo, B., Liebman, L., and Chalfie, M. (1998). Two functionally dependent acetylcholine subunits are encoded in a single *Caenorhabditis elegans* operon. *Proceedings of the National Academy of Sciences of the United States of America* 95, 15492-15495.
- Troemel, E.R., Chou, J.H., Dwyer, N.D., Colbert, H.A., and Bargmann, C.I. (1995). Divergent seven transmembrane receptors are candidate chemosensory receptors in *C. elegans*. *Cell* 83, 207-218.
- Turner-Evans, D.B., Jensen, K.T., Ali, S., Paterson, T., Sheridan, A., Ray, R.P., Wolff, T., Lauritzen, J.S., Rubin, G.M., Bock, D.D., *et al.* (2020). The Neuroanatomical Ultrastructure and Function of a Biological Ring Attractor. *Neuron* 108, 145-163.e110.
- van den Heuvel, M.P., Bullmore, E.T., and Sporns, O. (2016). Comparative Connectomics. *Trends in cognitive sciences* 20, 345-361.
- van den Heuvel, M.P., and Sporns, O. (2011). Rich-club organization of the human connectome. *The Journal of neuroscience : the official journal of the Society for Neuroscience* 31, 15775-15786.
- Varshney, L.R., Chen, B.L., Paniagua, E., Hall, D.H., and Chklovskii, D.B. (2011). Structural properties of the *Caenorhabditis elegans* neuronal network. *PLoS Computational Biology* 7, e1001066.
- Venkatachalam, V., Ji, N., Wang, X., Clark, C., Mitchell, J.K., Klein, M., Tabone, C.J., Florman, J., Ji, H., Greenwood, J., *et al.* (2016). Pan-neuronal imaging in roaming *Caenorhabditis elegans*. *Proceedings of the National Academy of Sciences of the United States of America* 113, E1082-1088.
- Wang, Y., Zhang, X., Xin, Q., Hung, W., Florman, J., Huo, J., Xu, T., Xie, Y., Alkema, M.J., Zhen, M., *et al.* (2020). Flexible motor sequence generation during stereotyped escape responses. *eLife* 9.
- Wanner, A.A., and Friedrich, R.W. (2020). Whitening of odor representations by the wiring diagram of the olfactory bulb. *Nature neuroscience* 23, 433-442.
- Watts, D.J., and Strogatz, S.H. (1998). Collective dynamics of 'small-world' networks. *Nature* 393, 440-442.
- Wen, Q., Po, M.D., Hulme, E., Chen, S., Liu, X., Kwok, S.W., Gershow, M., Leifer, A.M., Butler, V., Fang-Yen, C., *et al.* (2012). Proprioceptive coupling within motor neurons drives *C. elegans* forward locomotion. *Neuron* 76, 750-761.
- Wes, P.D., and Bargmann, C.I. (2001). *C. elegans* odour discrimination requires asymmetric diversity in olfactory neurons. *Nature* 410, 698-701.
- White, J.G., Southgate, E., Thomson, J.N., and Brenner, S. (1976). The structure of the ventral nerve cord of *Caenorhabditis elegans*. *Philosophical transactions of the Royal Society of London Series B, Biological sciences* 275, 327-348.

- White, J.G., Southgate, E., Thomson, J.N., and Brenner, S. (1986). The structure of the nervous system of the nematode *Caenorhabditis elegans*. *Philosophical transactions of the Royal Society of London Series B, Biological sciences* 314, 1-340.
- Witvliet, D., Mulcahy, B., Mitchell, J.K., Meirovitch, Y., Berger, D.R., Wu, Y., Liu, Y., Koh, W.X., Parvathala, R., Holmyard, D., *et al.* (2020). Connectomes across development reveal principles of brain maturation in *C. elegans*. *bioRxiv*, 2020.2004.2030.066209.
- Yan, G., Vértés, P.E., Towlson, E.K., Chew, Y.L., Walker, D.S., Schafer, W.R., and Barabási, A.-L. (2017). Network control principles predict neuron function in the *Caenorhabditis elegans* connectome. *Nature* 550, 519-523.
- Yemini, E., Lin, A., Nejatbakhsh, A., Varol, E., Sun, R., Mena, G.E., Samuel, A.D.T., Paninski, L., Venkatachalam, V., and Hobert, O. (2021). NeuroPAL: A Multicolor Atlas for Whole-Brain Neuronal Identification in *C. elegans*. *Cell* 184, 272-288.e211.
- Zheng, Z., Lauritzen, J.S., Perlman, E., Robinson, C.G., Nichols, M., Milkie, D., Torrens, O., Price, J., Fisher, C.B., Sharifi, N., *et al.* (2018). A Complete Electron Microscopy Volume of the Brain of Adult *Drosophila melanogaster*. *Cell* 174, 730-743.e722.
- Zhou, S., and Mondragon, R.J. (2004). The rich-club phenomenon in the Internet topology. *IEEE Communications Letters* 8, 180-182.
- Zimmer, M., Gray, J.M., Pokala, N., Chang, A.J., Karow, D.S., Marletta, M.A., Hudson, M.L., Morton, D.B., Chronis, N., and Bargmann, C.I. (2009). Neurons detect increases and decreases in oxygen levels using distinct guanylate cyclases. *Neuron* 61, 865-879.